UNIVERSITY OF GRANADA

PHYSICS AND SPACE SCIENCES

DOCTORAL THESIS

Colloidal assembly by convective deposition. The role of electric charge, substrate wettability and particle density

---

Author:
Diego NOGUERA MARÍN

Supervisors:
Dr. Miguel A.
RODRÍGUEZ-VALVERDE
Dr. Miguel A.
CABRERIZO-VÍLCHEZ

Granada - 27 de Febrero de 2015

Editorial: Universidad de Granada. Tesis Doctorales
Autor: Diego Noguera Marín
ISBN: 978-84-9125-075-3
URI: http://hdl.handle.net/10481/40011

El Doctorando Diego Noguera Marín y los directores de la tesis Dr. Miguel A. Rodríguez-Valverde y Dr. Miguel A. Cabrerizo-Vílchez, garantizamos, al firmar esta tesis doctoral, que el trabajo ha sido realizado por el doctorando bajo la dirección de los directores de la tesis y hasta donde nuestro conocimiento alcanza, en la realización del trabajo, se han respetado los derechos de otros autores a ser citados, cuando se han utilizado sus resultados o publicaciones en la realización del trabajo.

Granada, January 30, 2015

Director de la Tesis	Director de la Tesis	Doctorando
M.A. Rodríguez-Valverde	M.A. Cabrerizo-Vílchez	D. Noguera Marín

Contents

Acknowledgements

This work was supported by the“Ministerio Español de Educación, Cultura y Deporte” (Beca de Colaboración Orden EDU/1868/2011), “Ministerio Español de Ciencia e Innovación” (project MAT2011-23339) and the “Junta de Andalucía” (projects P07-FQM-2517, P09-FQM-4698 and P12-FQM-1443). D. Noguera and his supervisors are very grateful to the Biocolloid and Fluid Physics Group (ref. PAI-FQM115) of the University of Granada (Spain). Diego and his supervisors also thank Prof. Roque Hidalgo for fruitful discussion. Diego shows his appreciation to Dr. Yadira Sánchez for help with the AFM, Dr. Juan de Vicente for help with the viscosity measurements, Dr. Juan A. Holgado and Dr. Jesús Muros for help with the humidity measurements, David Porcel for help with the CLSM measurements and Alicia González for HRSEM assistance. Diego is also very grateful to Dr. Carmen Lucía Moraila for help with experimental issues and wise advice.

JUNTA DE ANDALUCIA

GOBIERNO
DE ESPAÑA

MINISTERIO
DE CIENCIA
E INNOVACIÓN

Aquí culmina mi carrera contra reloj para finalizar mi tesis doctoral. Diría que ha sido un camino largo, pero mentiría. Lo que sí diré es que ha sido un camino duro. He tenido la suerte de realizar mi tesis en esos años de oscuridad económica que, disfrazados de crisis, han marcado mi carrera investigadora hasta el momento. Pero nunca he estado por completo a oscuras, siempre ha habido alguna luz que me ha hecho seguir adelante, y a esas luces les dedico estas líneas:

En primer lugar quiero mencionar a Miguel Cabrerizo, que en medio del desierto de becas y financiación siempre se ha preocupado de llevarme a algún oasis. Por su incombustible vitalidad, por ser un referente en la ciencia creativa y recreativa y por mostrarse siempre dispuesto a darte una buena palmada en la espalda. Junto a él quiero agradecer a Miguel Ángel Rodríguez todo el tiempo invertido en mí. Por combatir con orden y tareas planificadas mi desorden y despiste con una paciencia infinita. Por demostrarme cómo se hace ciencia hoy en día y porque puedes contar con él cualquier día, a cualquier hora, y siempre con el mismo entusiasmo.

En segundo lugar quiero nombrar a Carmen, porque es mi directora emérita. Porque me ha enseñado mucho más de lo que yo podría escribir. Porque su manera de ser, su afán de superación y su entereza en los momentos más duros, han sido inspiración para mí. Sin ella no estaría escrita esta tesis.

Quiero agradecer también a todo el grupo de Física de Fluidos y Biocoloides, de la Universidad de Granada. Me siento muy afortunado de haber podido investigar en el seno de este grupo que te ayuda a no perder la esperanza; todavía hay gente que lucha por la ciencia. Sois muchos, y me conocéis bastante como para no ofenderos si se me olvida algún nombre. Quiero agradecer a Yadira su ayuda con el bendito AFM, a Teresa porque llegaste justo a tiempo para hacerme compañía en el laboratorio blanco, a Kasia porque siempre tienes tiempo para una pequeña charla, a Fernando que hace que no nos falte de nada, a Juan de Vicente por dedicarme su tiempo en el reómetro, a Julia por su verde esperanza, a Arturo y Alberto porque siempre me arrancáis una risa al cruzarme con vosotros, a María por cuidar de la Sala, a Roque porque su pasión y su actitud de *eterno aprendiz* son inspiración, a Delfi, Pepe, Curro, Mª José, Ana Belén, Peula, Juan Luis, Antonio . . . y todos los que dais alma a este grupo.

También quiero agradecer a Conrado, Miguel Heredia y Belén su ayuda superando los escollos administrativos, a Jose Antonio “el Técnico” por su asistencia y a Ángel Delgado por su guía a modo de brújula en el océano llamado “Plan de Doctorado”.

Por supuesto entre los renglones de esta tesis está puesta la ayuda y el esfuerzo de todos los miembros de ese habitáculo multiusos que llamamos *Sala* (sin ponerle apellid+s). Quiero agradecer a Azahara porque hablar con ella es abrir una ventana y que entre aire fresco, es encontrar el punto de vista que no sabía ni que existía, a Leo, porque contesta siempre con una sonrisa a un número infinito no-numerable de mis preguntas, por tontas que sean, a Irene porque es la compañera infalible y porque creo que ha resucitado la sala cuando estaba a punto de venirse abajo, a Inma porque te anima a devolverle una sonrisa a la vida pase lo que pase, a Jose porque le da alegría y espíritu a todo lo que hace y eso se contagia, a Germán porque gracias a él sigo vivo pese a trabajar en un laboratorio "peligroso" y porque es ejemplo de principios y valores en la ciencia, Migue porque es un "inventor" de los de antes, su inquietud y habilidad están igual de desarrolladas, a Juan Pablo porque si él está, la risa y el buen rollo se respiran, me encanta su actitud hacia la vida y a Keshwad porque empezamos este camino juntos y su adaptación ha sido digna de admirar. No quiero dejarme a los que ya no están, Felipe y su incombustible buen humor, Álvaro y su asistencia para lo que haga falta, Paola y su vitalidad contagiosa, Amelia y su ejemplo como investigadora, Luisma que todavía nos regala sus visitas, Dani y los momentos compartidos en el laboratorio y de congreso, y los miembros adoptivos Paloma, Nico, Mª del Mar, Laura... muchas gracias a todos.

Por supuesto quiero agradecer a todos mis amigos, los que no necesitan que escriba su nombre, los selectos. Porque me han apoyado y se han preocupado por mi cuando el monstruo de la tesis me ha secuestrado mucho tiempo. Gracias porque, día a día hay mucha gente que me hace sentirme su 'hermanico', ya estén en Granada, Madrid, Mérida, Perú, Chile, Mozambique. . . *por saber compartir vuestras vidas y sacarme de mis pobrezas.*

También quiero agradecer a toda mi familia. Porque han sido el motor, porque da igual lo alto que esté, ellos saltan conmigo. Porque cada uno a su manera, con charlas infinitas llenas de huecos infinitos, compartiendo anécdotas de laboratorio, consejos y preguntas, con un " Hermano. . . dónde estás que no te veo?", con comentarios frikis, chistes malos o haciéndome ver que mi tesis es sólo "carne perro" se han ganado el título de doctores consortes. Porque ellos no entienden las palabras raras, pero saben leer el mensaje oculto en esta tesis: *ni un paso atrás*.

Por último quiero agradecer a la luz más grande de todas en este camino: Sara. Esta tesis se la debo a ella. Ella me ha cuidado, aguantado, apoyado, animado, escuchado. . . porque sólo con ella habría sido posible y solo por ella lo ha sido. Porque sólo con ella me atreví a emprender esta aventura y sólo con ella me atrevo a emprender muchas más.

Summary

Currently, the study of colloidal assembly by convective deposition is an emerging topic: nanolithography, particle templating and design of "smart surfaces" could be some examples. This is supported by the increasing number of works recently published.

The variety of morphologies observed in the particle deposits produced by solvent evaporation may be ruled to a large extent by contact line dynamics according to the so-called "Coffee Stain" effect, but the wettability properties of the substrate can alter it drastically. The magnitude of the convective capillary flow varies as the contact angle held at the pinned or moving contact line. On the other hand, motion of charge-stabilized particles in confined regions and subjected to an evaporation-driven capillary flow might be ruled by collective diffusion. There are many ways to affect the diffusion coefficient of colloidal particles and an elegant method is charge. The interparticle repulsion leads to an enhancement of collective diffusion at large concentrations. However, the "Coffee Stain" effect typically ignores the interparticle and substrate-particle electrostatic interactions.

In this thesis we have studied the assembly of colloidal particles by convective deposition. We have examined the effect of three factors: particle electric charge, wettability properties of the substrate, and charge-mass ratio of the particles using two experimental approaches: driven evaporating menisci and free evaporating drops.

Using these methodologies, the wettability properties of the substrate were found to be important for colloidal assembly. Driven evaporating menisci experiments showed a transition from

stripe-like deposit to heterogeneous film as the substrate used. We confirmed that the receding contact angle imposes a geometrical constraint for the particles at the triple line and due to this, size segregation of binary suspensions was observed with Confocal Laser Scanning Microscopy (CLSM) of free evaporating drops. The effects of wettability properties of the substrate on the colloidal assembly are coupled because self-pinning affects contact line dynamics, and the particle accumulation depends at different extents on the space available near the contact line, the time of natural pinning and mostly, the convective flow. We also found that collective diffusion mitigated the arrival of electrically charged particles to the contact line, regardless of the type of particle, the substrate or the methodology used. From the experiments of driven receding contact lines, we conclude that the particle deposition may be controlled by the interplay between evaporative convection and collective diffusion. Experiments carried out with binary colloidal mixtures illustrated the influence of collective diffusion on the particle deposition. Diffusive flow in drops takes relevance at low particle concentration, when the gradient between the contact line and bulk is important. Instead, in driven evaporating menisci the bulk concentration remains constant and the effects due to concentration gradient are enhanced. In both scenarios, substrate-particle interactions seems to play no significant role because the deposition of particles was favored for the nearly uncharged particles rather than the charged ones, even for the opposite charged substrate-particle system.

Finally, we found that binary mixtures of particles with different charge-mass ratio reveal segregation as the “colloidal Brazil nut” effect. This segregation produced an increase of the rate of accumulation of the particles suspended with higher charge-mass ratios. Otherwise, the particles with lower charge-mass ratio arrived at the contact line at lower rate.

Resumen

Hoy en día, el estudio del ensamblado coloidal por deposición convectiva es un tema en auge: nanolitografía, recubrimientos o el diseño de superficies con propiedades controladas son ejemplos de sus aplicaciones. Esto está respaldado por el creciente número de trabajos que han sido publicados recientemente.

La amplia gama de morfologías obtenidas por deposición de partículas a raíz de la evaporación de soluto puede estar condicionada en gran medida por la dinámica de la línea de contacto y por el fenómeno conocido como efecto "Mancha de Café", pero las propiedades de mojado del sustrato pueden alterarlo de manera drástica. La intensidad del flujo convectivo-capilar varía con el ángulo de contacto de retroceso que adopta la línea de tres fases, ya esté anclada o retrocediendo. Por otro lado, el movimiento en espacios confinados de partículas estabilizadas por medio de su carga y sometidas a un flujo convectivo originado por la evaporación, podría estar gobernado por la difusión colectiva. Hay muchas vías para variar el coeficiente de difusión de partículas coloidales, y una manera elegante de hacerlo es a través de la carga. La repulsión entre las partículas en grandes concentraciones produce un aumento de la difusión colectiva. Sin embargo, el efecto "Mancha de Café" normalmente ignora la interacción electrostática entre partículas, o de éstas con el sustrato.

En esta tesis se estudia el ensamblado de partículas coloidales por deposición convectiva. Hemos examinado el efecto de tres factores: carga eléctrica de la partícula, las propiedades de mojado de los sustratos y la relación carga-masa de las partículas usando dos técnicas experimentales: meniscos líquidos guiados y gotas evaporándose libremente.

Se ha observado en ambas metodologías que las propiedades de mojado del sustrato utilizado son importantes en el ensamblado coloidal. En los experimentos realizados con meniscos líquidos guiados se obtuvieron unos patrones a bandas que se iban atenuando hasta formar una capa uniforme según el sustrato utilizado. Hemos confirmado que el ángulo de contacto de retroceso impone una restricción geométrica para las partículas en la línea de contacto y debido a esto, las suspensiones binarias analizadas por Microscopía de Barrido Láser Confocal mostraron una segregación por tamaños en la configuración de gota evaporándose libremente. Hemos concluido que las propiedades de mojado y el auto-ensamblado coloidal están acoplados ya que, la acumulación de partículas provoca el anclaje de la línea y esto altera su dinámica, mientras que la deposición de partículas depende, entre otros factores, del espacio disponible, de los estados meta-estables que adopte la línea y sobre todo, del flujo convectivo.

También hemos observado cómo la difusión colectiva mitiga la llegada a la línea de contacto de partículas cargadas electrostáticamente, sin importar el tipo de partícula, el sustrato o la metodología empleada. De los experimentos con meniscos líquidos guiados, hemos concluido que la deposición de partículas es el resultado de un balance entre el flujo convectivo ocasionado por el gradiente de evaporación y el flujo difusivo ocasionado por el gradiente de concentración. Los experimentos con suspensiones binarias han ilustrado muy bien la influencia del flujo difusivo en la deposición de partículas. Éste, cobra importancia cuando la concentración de partículas es baja, siendo así mayor el gradiente de concentración entre el seno de la gota y la línea de contacto, aunque la concentración en el seno de la gota varía con el tiempo conforme ésta pierde volumen de disolvente. Por otro lado, en los experimentos de meniscos líquidos guiados la concentración en el seno del reservorio permanece constante y los efectos debidos a gradientes de concentración quedan resaltados. En ambas situaciones, la interacción entre la partícula y el sustrato parece no ser determinante ya que la deposición de partículas casi descargadas en la línea de contacto ha sido siempre mayor que la acumulación de partículas cargadas, incluso cuándo el sistema sustrato-partícula tenía cargas opuestas (y la deposición estaba electrostáticamente favorecida).

Por último, hemos observado cómo las mezclas binarias de partículas con diferente relación carga-masa segregaron según el fenómeno conocido como efecto “nueces de Brasil coloidal”. Esta segregación ha producido un aumento en la acumulación de partículas suspendidas con mayor relación carga-masa. Por el contrario, partículas con menor relación carga-masa llegaron a la línea de contacto a un ritmo menor. Estos resultados abren una vía para conseguir un mayor control del depósito de las partículas sobre un sustrato en auto-ensamblado convectivo.

Motivation

Colloidal assembly by convective deposition is a phenomenon closely related to our every day life. Formation of ring-like stains after drying of a coffee drop on a substrate is a paradigmatic example (*1*). The formation of these deposits at the periphery of the drop is known as "Coffee Stain/Ring" effect. However this effect is not exclusive to coffee. Any complex liquid containing colloidal particles in suspension, such as tears, dishwasher, wine or body fluids, exhibits this behavior when it is allowed to evaporate on a substrate (*2*) (see Figure 1).

Identification of the variables involved in the convective/capillary self-assembly is of great relevance to control the deposit morphology (*3*). Controlling the particle deposition is interesting for lithography (*4*), optoelectronics (*5*), paints (*6*), inkjet printing and medical diagnosis (*7*–*9*). Numerous studies have been devoted to analyze the different morphologies of the deposits (*10*–*12*). The identification of cracks and invaginations in the final deposit of body fluids is useful to reveal certain diseases (*13*) (see Figure 2). Drying of complex liquids can be also used to assemble different materials and to produce surfaces with different properties (*14*), such as templates. Printing and painting are fields where film drying becomes very critical (*15*, *16*).

The occurrence of "Coffee Ring" effect is not always desirable. In biotechnology a uniform deposition of biological moieties, such as bacteria or DNA molecules, is needed to examine them on a substrate. Otherwise, when a paint dries, uniform coatings are intended. This is the reason why numerous studies aim to avoid or mitigate the "Coffee Stain" effect (*17*–*19*). Marangoni flow due to surface tension gradients has been found to reverse this effect (*20*, *21*). Surfactants, very volatile solvents or thermal variations can produce Marangoni flow (*22*, *23*). Size and shape

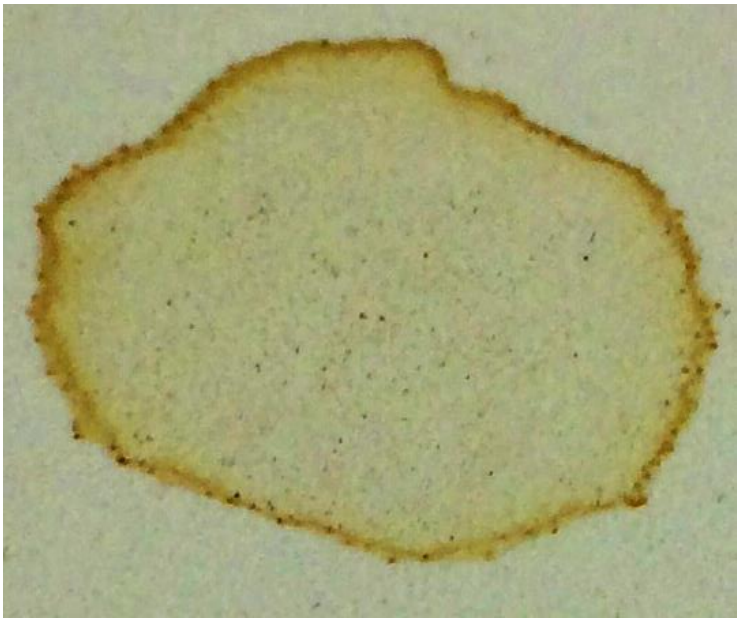

Figure 1: Image of an evaporated drop of pumpkin soup on a kitchen counter. The borders of the deposit are darker due to the "Cofee Stain" effect.

of the colloidal particle can also modulate the convective/capillary self-assembly.

"Coffee Stain" effect is a fascinating phenomenon, but at the same time, it has proven itself to be very complex (*24*). The evaporation of colloidal drops is governed by the coupling of multiple factors such as heat and mass transfer, hydrodynamics, viscous and inertial flows and wetting (*25*, *26*). This out-of-the-equilibrium scenario is hard to explore. The drying of a colloidal suspension is challenging to reproduce. Liquid loss along the liquid-air interface depends on the relative humidity and temperature (*27*). Wettability properties of the substrate can alter the deposition as the evaporation rate depends on substrate contact angle (*28*). We need to standardize the method to measure meaningful values.

A better control of colloidal assembly by convective deposition is particularly helpful in particle templating and nanolithography. However, knowledge about the different factors that can alter colloidal patterning mechanisms is still incomplete. It is known that the magnitude of the convective capillary flow varies as the contact angle held at the pinned or moving contact line (*29*). For low contact angles, the evaporation gradient on the drop surface is much more prominent at the triple line and thus, the convective flow is enhanced (*30*). On the other hand, the value of receding contact angle determines the geometrical constraints for the particle arrangement. The space available for the particle deposit is limited because of the so-called "wedge effect" (*31*, *32*). The space close to the contact line enables to segregate particles with different size as its aperture angle (*33*, *34*). Although the impact of substrate contact angle is apparently well-established in colloidal patterning, the wettability properties of a substrate are indeed described by their contact angle hysteresis (35) and receding contact angle (36). Moreover, contact angle hysteresis enhances contact line self-pinning (37–40) and the final deposit morphology is highly dependent on contact line dynamics (41). Recently, controlled wettability of substrates has been used to alter (42), or even to suppress the deposits (43). Otherwise, patterned substrates have been used in evaporating drop experiments (44) and for colloidal self-assembly by dip-coating (45). To the best of our knowledge, these parameters of the substrates have not been investigated in guided depositions where the receding lines are driven by an external force. A better understanding of how these parameters affect the deposition would allow to exploit them.

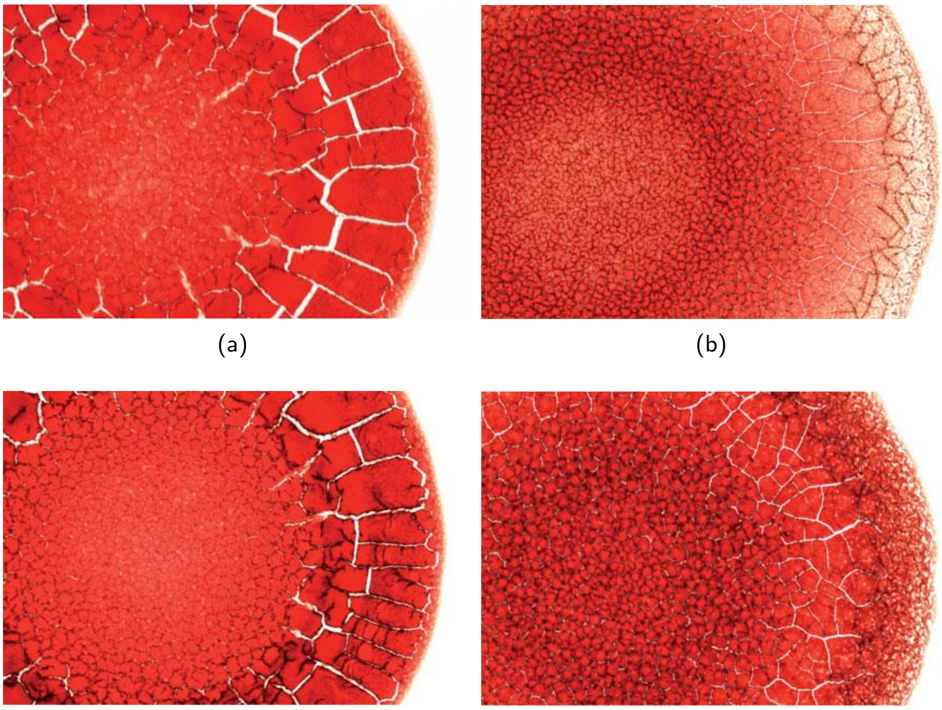

(a) (b) (c) (d)

Figure 2: Image of four evaporated blood drops. The difference in their cracks and shape can determinate if the blood comes from (a) a healthy woman, (b) a person with anaemia, (c) a healthy man or (d) a person with hyperlipidaemia (46).

Particle properties are further relevant for colloidal deposition. Collective diffusion of electrically charged particles in convective assembly deposition has been barely explored (47). Experimental results on the dynamics of charge-stabilized colloids at high colloid concentrations are very scarce. Besides, in the complex evaporating process, it is difficult to distinguish diffusive and convective displacements of particles by imaging techniques. Although other techniques might be used to measure collective diffusion such as dynamic light scattering and pulsed field gradient NMR, in-situ measurements of concentration profiles are hardly realizable. Otherwise, fluorescent particles have been successfully used to record dynamics inside colloidal drops in the vicinity of the contact line (*31*, *48*). Confocal Laser Scanning Microscopy (CLSM) is a well-established technique (*49*) that allows real time imaging of fluorescent targets.

Segregation of particles during capillary/convective self-assembly is interesting to be prevented or promoted, accordingly (*50*, *51*). Charged colloids sediment more slowly than uncharged ones since near-contact configurations are disfavored. However, in highly charged colloidal mixtures at low ionic strength, where the electrostatic energy of electrolyte ions is higher than the thermal energy, the so-called "colloidal Brazil nut" effect (*52*) retards and eventually inhibits further sedimentation. As their charge-mass ratio, the charged larger particles are enriched at the top of the mixture, rather than the bottom. This scenario might be also observed in the evaporation-driven colloidal assembly where the particle segregation is established between the contact line and drop bulk. Dynamics of certain charge-stabilized colloids, such as micron-sized polystyrene spheres in deionized water, appears to be governed by an effective charge smaller in magnitude than the structural charge, provided that the particle surface groups are fully dissociated. This effective charge unexpectedly increases with electrolyte concentration, as observed in electrophoretic mobility experiments (*53*). Ion condensation (*54*, *55*) is widely used to interpret this phenomenon, where counter-ions are strongly attracted to the particle surface and accumulate in a thin layer around it. At greater ionic strength, this layer of counter-ions strongly bound to the particle is "screened" by the in excess-coion cloud.

This thesis focused on three factors in the convective deposition: particle electric charge, wettability properties of the substrate, and charge-mass ratio of the particles. The dissertation is divided into two parts as the technique used. In the firs part, we formed driven evaporating menisci like in the dip-coating technique used in the coating industry. We used smooth substrates with very different wettability properties and nanoparticles of different size and surface charge. For fixed withdrawal velocity, evaporation conditions and particle concentration, we analyzed the morphology of the deposits formed with variety of substrate-particle systems where the particle-particle electrostatic interaction was changed (via pH) as well as the wettability properties by different glass substrates. We further altered the particle deposition through the relative humidity and particle concentration for a fixed substrate-particle system. In this experimental approach, the particle concentration in bulk remains constant during the entire experiment and the effects due to particle concentration gradients at the contact line can be noticeable. On the other hand high sample volume is needed to produce the capillary rise and the technique requires high concentration to obtain significant patterns.

In the second part, free evaporating drops were used to examine the impact of the above mentioned factors under realistic conditions in a well studied scenario. There are numerous works devoted to the study of colloidal drop drying (*56*) although they are mostly limited to the final deposits analysis and they depend on the ireproducibility of drop evaporation as the liquid-air interface is higher than the solid-liquid one. Instead, we monitored in-situ the accumulation of particles arriving at the contact line of evaporating sessile drops by CLSM (*57*). From particle counting, we evaluated the particle increment per unit of drop area over the time. We used four substrates with different wettability properties and six types of particle selected as their size, density and electric charge response. The area of deposit is lower than deposits on driven-evaporating menisci, but horizontal substrates is favored for in-situ measurements than the vertical substrates at the menisci configuration.

CHAPTER 1

Theoretical framework

1.1 Coffee ring effect

When a drop of coffee dries on a substrate, a ring-like deposit is typically observed (see Figure 1.1). This phenomena was first described by Deegan et al. (*1*) and next supported with numerical studies by Fischer (*58*). During the evaporation of a sessile drop, the liquid loss is faster at the triple line. This is due to the geometry of the drop in a similar manner as a baked potato gets roasted at the edges (*59*), or the electrical field inside a conductor at a fixed potential diverges at its corner or edges (*60*). This way, evaporation gradient along the drop surface diverges at the contact line. This greater rate of evaporation at the contact line produces an outward convective flow from the bulk to balance the liquid loss (see Figure 1.2). When colloidal particles are suspended in the drop, they are transported towards the periphery by this convective flow. This mechanism is the responsible for the ring-like deposits observed after the evaporation of colloidal drops, known as "Coffee Ring" or "Coffee Stain" effect.

This phenomenon and the morphology of final deposits depend on multiple factors in heat conduction and convection, evaporative mass transfer, viscous and inertial flows, thermal and hydrodynamic instabilities, Marangoni flows, wettability properties of the substrate and contact line pinning-depining (*61*–*67*). This fascinating and complex phenomenon has numerous applications

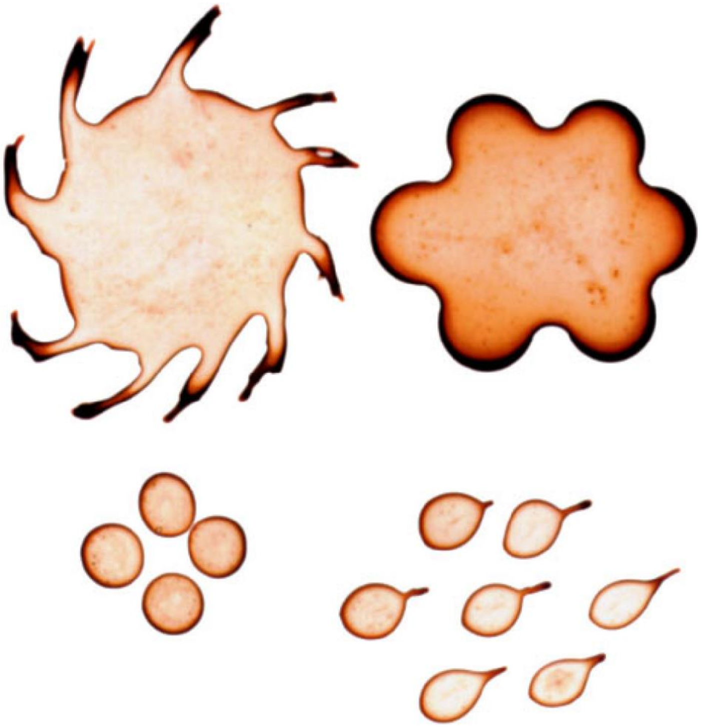

Figure 1.1: Coffee deposits left by dried drops. It is very clear how the deposits are darker at the most curved regions.

such as optoelectronics (*16*), inkjet printing (*68*), nanolithography (*69*), biotechnology (*70*) and medical diagnosis (*9*).

There is a vast variety of patterns left on the substrates when a colloidal drop completely evaporates (see Figure 1.3). This has been proven useful for disease diagnosis as pointed out by Yakhno et al. (*73*). They used drops of serum to identify different types of pathologies. In a similar matter, Brutin et al. used the patterns left by blood drops to identify certain diseases (*13*). Ring-like deposits (single or multiple ring) (*1*), central bumps (*71*) and branch-like (*74*) deposits produced with drops, stripe-like patterns and continuous layers with menisci (*39*) have been reported in the literature. The particle arrangement within the deposits depends on the volume fraction, particle size, contact line velocity and rate of deposition (*75*). The speed of the particles arriving at the contact line seems to be crucial (*76*). However, the suppression of the "Coffee Ring" effect is also intended.

"Coffee Stain" effect is undesired in inkjet printing and coatings such as paints where homogeneous layers are expected. The first condition that has to be fulfilled to obtain a ring-like pattern is that the liquid meets the surface at a non-zero contact angle. This has a direct relation with the evaporation gradient along the drop surface, which depends on the contact angle (see Section 1.2). If evaporation is mitigated (at least locally (*77*)), the "Coffee Ring" effect does not

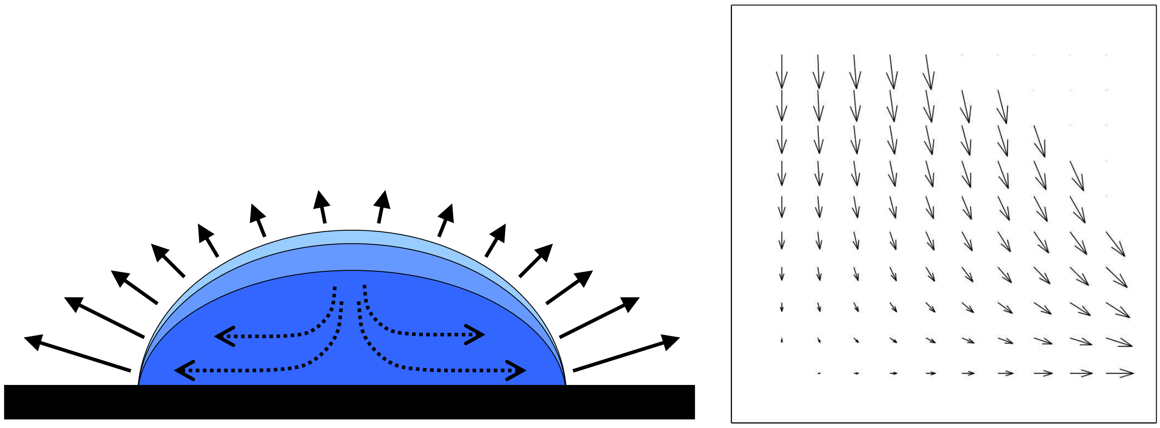

(a) (b)

Figure 1.2: (a) Sketch of the evaporation gradient produced along the surface of a sessile drop. (b) This gradient produces a convective flow to replenish the liquid loss at the triple line.

occur. The second condition for the accumulation of particles is that the contact line is pinned. The own accumulation of particles at the triple line produces the effect known as "self-pinning". However, if the contact line moved, the "Coffee Ring" effect would be also mitigated (78).

Electrostatic interactions must be also taken into account in convective self assembly. Bhardwaj et al. (71) analyzed in terms of DLVO interactions[a] the influence of pH on the final deposit left by dried colloidal drops. Yan et al. (81) also studied the influence of particle charge in the convective self-assembly reporting more ordered deposits for charged particles. Hsueh et al. (82) reported different morphology on deposits at different pH for the meniscus configuration. For sessile drop configuration, a study of the influence of electrostatic interactions was carried out by Moraila et al. (83). Recent work also intend to suppress the coffee ring effect by applying external electric field to alter the interactions (17).

Marangoni flows can modulate the "Coffee Ring" effect (20, 22, 48, 84, 85). Elipsoidal particles further modulate, even suppress, the ring-like deposit (86). Particles adopt different aggregation configurations nearby the triple line depending on their shape (87). Wettability properties also affect the convective self assembly (36) in different manners as discussed in Section 1.2. Recently, controlled wettability of substrates has been used to alter (42), or even to suppress the deposits (43). Moreover, patterned substrates have been used in evaporating drop experiments (44) and for colloidal self-assembly by dip-coating (45). The influence of the wettability properties of substrates on the particle deposition is apparently well-established (38), although it has not

---

[a] DLVO is a colloidal stability theory proposed by Derjaguin, Landau, Verwey and Overbeek. More information about this theory can be found in references (79, 80).

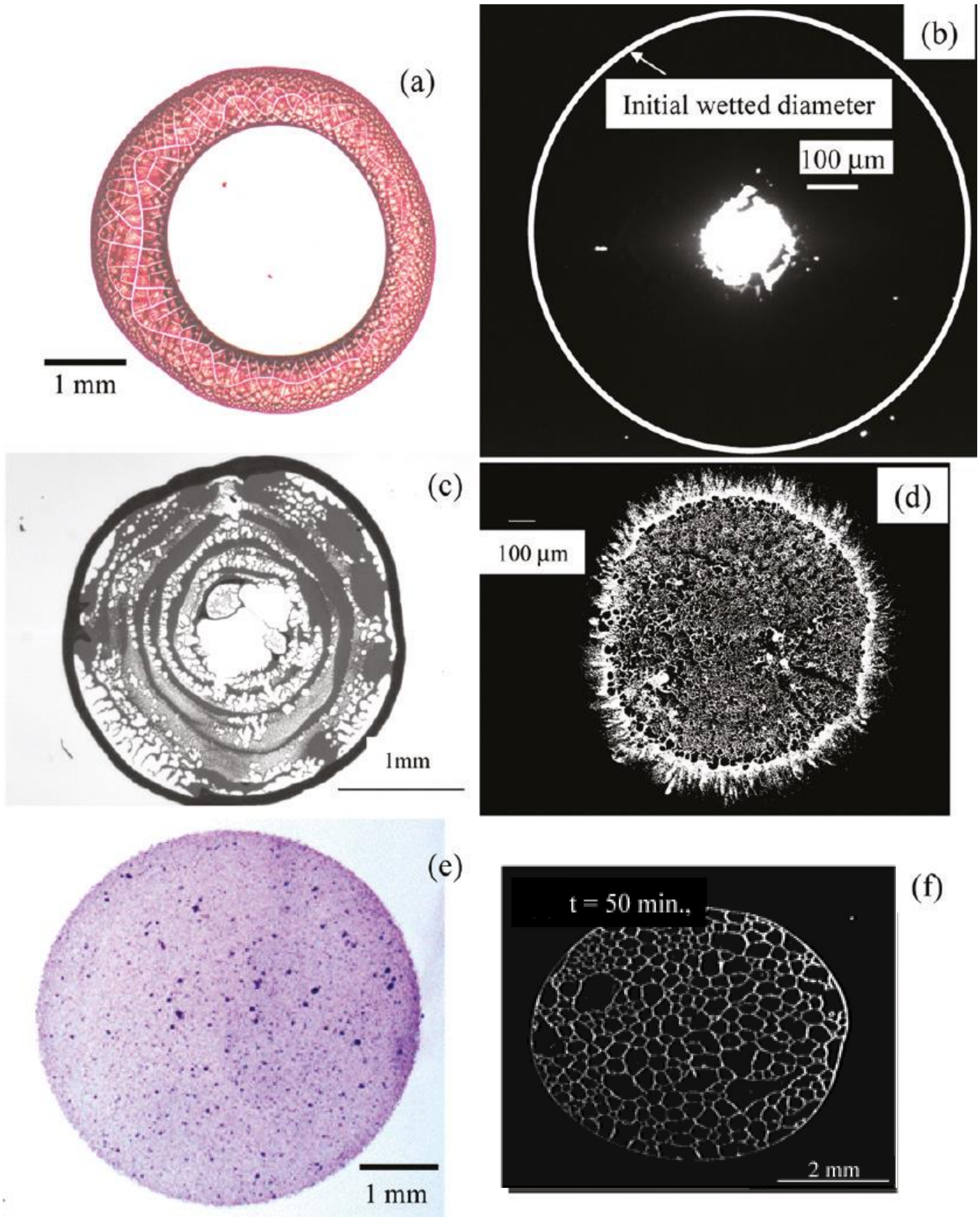

Figure 1.3: Different patterns that can be obtained when a drop evaporates: (a) ring (*34*), (b) central bump (*26*), (c) multiple rings (d), fingering (*71*), (e) uniform layer (*72*) and (f) network of polygons.

been exploited sufficiently

1.2 Wettability

When a liquid interacts with a solid surface, a force balance is held at the three-phase contact line. The ability of a solid surface to be wet by a liquid is known as "wettability". A portion of liquid spreads over a solid surface if the energy required to create a unit area of liquid-vapor interface does not exceed the energy gained in creating a unit area of solid-liquid interface (*88*). We can classify the solid surfaces as hydrophilic or hydrophobic as the adhesion force between the solid and liquid is greater than the cohesion force or vice versa respectively. When the equilibrium is reached and the tangential interfacial forces are balanced (see Figure 1.4), the following condition is fulfilled:

$$\cos\theta = \frac{\gamma_{SV} - \gamma_{SL}}{\gamma_{LV}} \tag{1.1}$$

where γ_{SV}, γ_{SL} and γ_{LV} are the interfacial tensions at each interface (Solid-Vapour, Solid-Liquid and Liquid-Vapour, respectively) and θ is the angle formed between the unit vector tangent to the liquid-vapour interface and the tangent to the solid-liquid interface at the edge of the drop (known as three-phase contact line or triple line). Eq. 1.1 is commonly known as the Young equation (*89*). From contact angle, we can identify hydrophilic surfaces as those ones with contact angle lower than 90°,

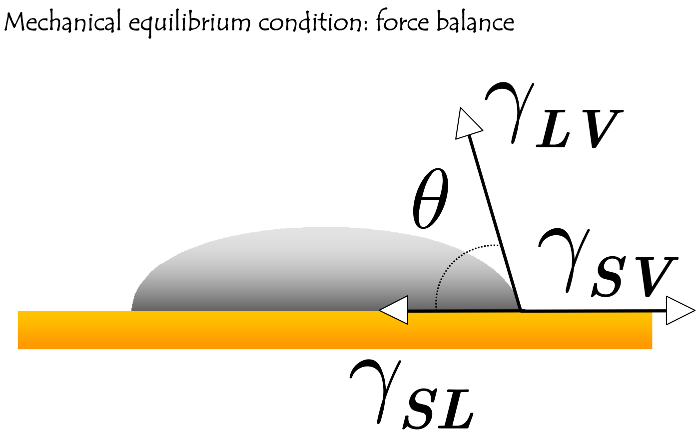

Figure 1.4: Interfacial forces and contact angle at the triple line of a sessile drop on a solid substrate.

When we dip two parallel substrates separated by a "small" distance d into a pool or reservoir perpendicularly, capillary rise/fall occurs. If we use hydrophilic substrates, the column inside the substrate rises but, for hydrophobic substrates, the column falls down instead (see Figure 1.5). This behavior is due to the balance between the gravity and adhesion forces at the contact line

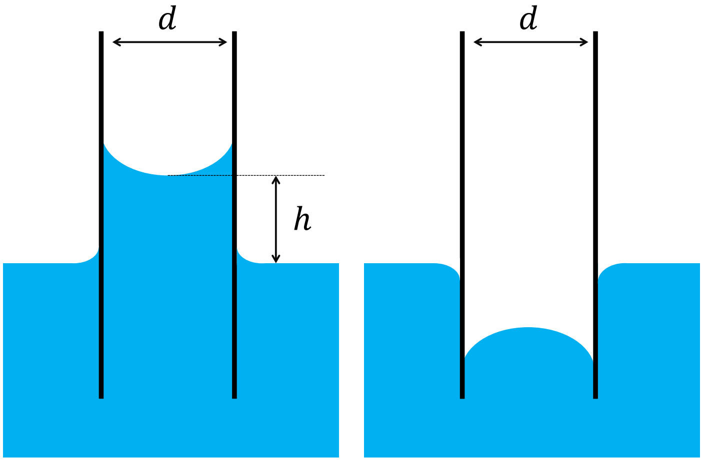

(a) (b)

Figure 1.5: (a) Capillary rise and (b) fall, between two vertical plates separated by a distance d. For hydrophilic substrates, capillary rise will occur while hydrophobic substrates will produce the capillary fall.

of the meniscus. Jurin's law states that the height of the liquid column is (*90*):

$$h = \frac{2\gamma cos\theta}{d\rho g} \tag{1.2}$$

where γ is the surface tension, ρ the density of the liquid, g is the gravity acceleration. Eq. 1.2 provides an expression that relates the height of the loquid (h) with the contact angle of the substrate (θ), provided that the distance d between plates satisfies the relation $d << \sqrt{\frac{\gamma}{\rho g}}$.

1.2.1 Contact angle hysteresis

In real surfaces, observable contact angle depends on the history of the system (*91*). If we place several drops on a substrate, the observed value of contact angle will not be the same. However, there are two values that depend on the substrate and liquid used, rather than the history of the drop (*92*): advancing contact angle θ_A (which is the maximum value, usually adopted when the contact line is advancing) and receding contact angle θ_R (which is the minimum value, usually adopted when the conctact line is receding). Contact Angle Hysteresis (CAH) is commonly defined as the difference between θ_A and θ_R. This way, when we place a drop on a substrate, the contact angle can reach any value between the receding and advancing contact angles. In terms of free energy, a solid-liquid-vapour system has multiple local minima corresponding to multiple metastable states (see Figure 1.6). Greater number of metastates will be observed with substrates of higher CAH.

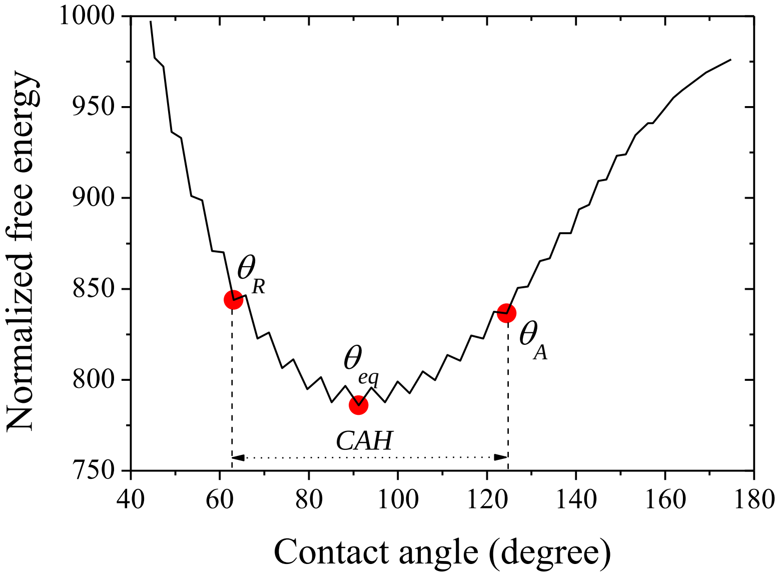

Figure 1.6: Dimensionless free energy versus the contact angle for a fixed drop volume (*93*).

CAH rules the dynamics of contact line (*94*). Final deposit morphology of self-assembled deposits is depends on contact line dynamics (*41*). In convective-evaporative self-assembly, pinning of contact line will take longer whereas the contact angle is decreasing up to the receding contact angle from higher angles (see Section 1.2.2). During this pinning time the triple line remains static (*40*), whereas the particles are transported towards the contact line. Greater pinning time leads to a higher number of particles deposited at the contact line and this enhances the so-called 'self-pinning' (*95*). This repeated mechanism allows the formation of multiple concentric rings with evaporating drops (*96*).

1.2.2 Drop evaporation

Understanding the process of drop evaporation is of great importance for industrial and scientific areas. Description of this phenomena has been the aim of numerous studies since several years (*27*, *97*, *98*). Drop evaporation typically occur in two stages (*25*):

- The drop volume decreases while the wet area remains constant. This only occurs if the contact line is pinned. The contact angle (initially θ_0) decreases until it reaches the receding contact angle value θ_R (see Figure 1.7a).
- Once θ_R is reached, the radius of the drop decreases at constant contact angle value (see Figure 1.7b).

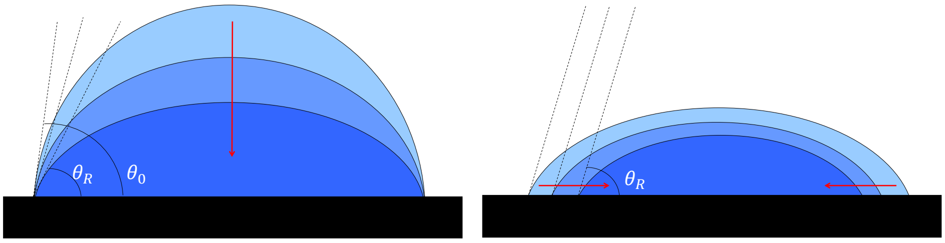

(a) (b)

Figure 1.7: Stages of drop evaporation: (a) the triple line remains pinned and the height of the drop decreases with time and (b) the contact radius decreases and the contact angle remains constant.

Liquid molecules at the surface of a drop will diffuse to the surrounding atmosphere (*56*). Contact angle plays a central role in this process. A liquid molecule randomly moving at the surface of a low-contact angle drop, is more likely to escape if it is close to the contact line due to the interfacial curvature (*99*). On the contrary, a liquid molecule at the surface nearby the triple line of a non-wetting drop, is more likely to remain within the drop. Figure 1.8 shows the local evaporation rate distribution along the surface of two drops with different contact angles.

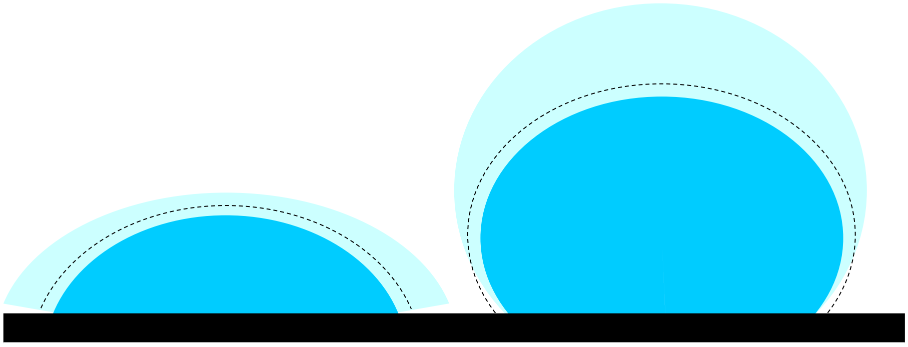

Figure 1.8: Evaporation rate for wetting (left) and non-wetting (right) drops. Dashed lines represent an uniform evaporation rate. Shadowed region around the drops illustrate the intensity of local evaporation rate.

In evaporating colloidal drops, the different local evaporation rate acquires great relevance because it will establish the intensity of the convective flow to replenish the liquid loss at the contact line. Deegan et al. (*100*) proposed that the evaporation-driven flow at the distance z from the triple line, j_{evap}, responsible for the migration of particles towards the contact line, depends on contact angle as follows:

$$j_{evap}(z,\theta) \propto z^{\frac{\pi}{2(\pi-\theta)}-1} \tag{1.3}$$

Lower contact angles produce higher flow and thus, a faster accumulation of particles nearby the contact line (*29*). In other respects, contact angle imposes a geometric constraint confining the particles into a wedge-shaped region (see Figure 1.9). This is the so-called "wedge effect" and is useful for size segregation (*31*). It is important to take into account that in such a confined region, short-range interactions might alter the behavior of the particles (*101*).

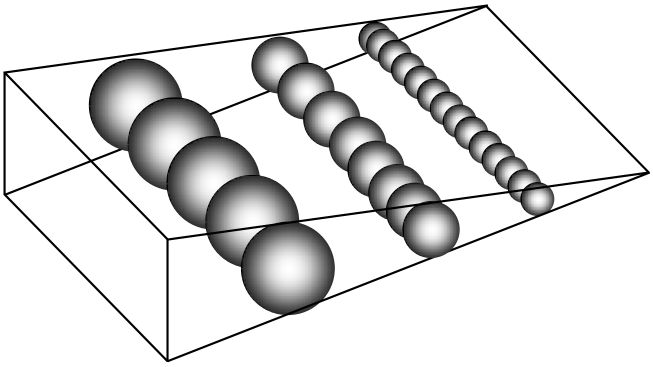

Figure 1.9: Particles of different size confined in wedge-shaped region nearby the contact line. Smaller particles can further penetrate in the wedge.

1.3 Electric charge of particles

Particles-particle and substrate-particle electrostatic interactions should be taken into account in the convective-driven self-assembly. Charged particles will produce different deposits on an oppositely-charged substrate than on a like-charged substrate (*71*, *83*) (see Figure 1.10). Some studies (*74*) have reported with mathematical models the that long-range interaction should be taken into account as they might control the occurrence of the "Coffee Stain" effect.

1.3.1 Collective diffusion

Particle charge might also affect the evaporation-driven self-assembly by means of collective diffusion. Electrostatic interactions occur at long distances (in terms of particle radius), but as the particles are transported to the triple line, confinement takes place. In such dense systems,

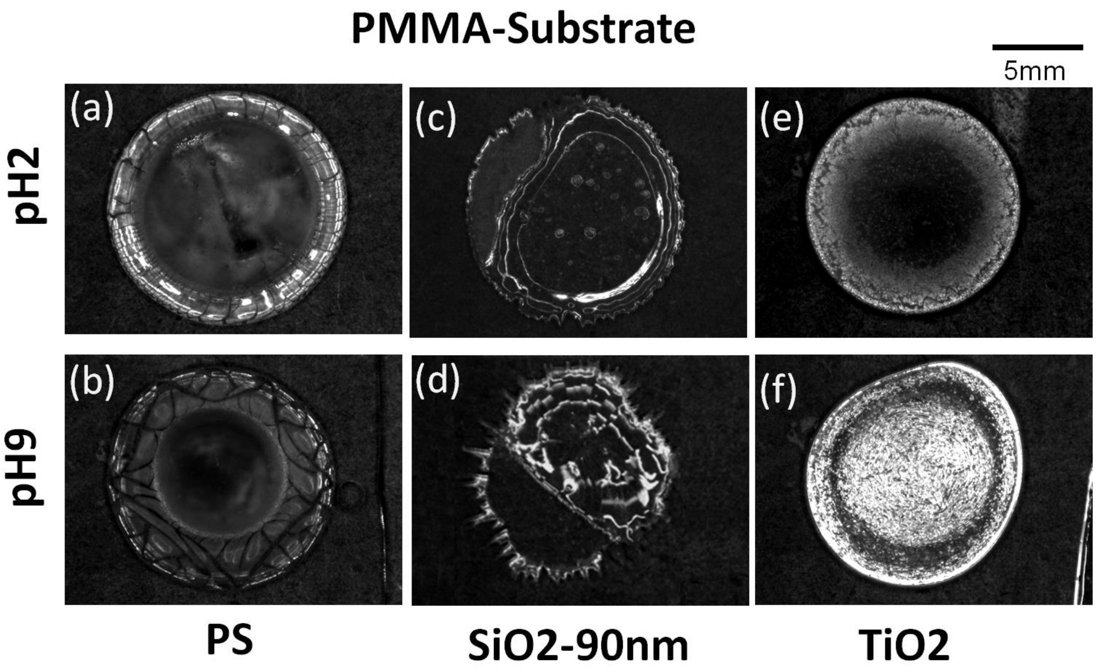

Figure 1.10: Deposits obtained for free evaporating drops at different pH values on a PMMA substrate using three different particles (83).

mutual or collective diffusion[b] takes relevance rather than self-diffusion[c].

Firstly, we will describe collective diffusion of colloidal particles. When the local gradient of particle concentration increases during the evaporation of a drop/meniscus, the Fick's law establishes that an inward flow is created towards the bulk by particle cooperative diffusion. This diffusive flow $\vec{j_D}(\phi)$ follows the first Fick Law:

$$\vec{j_D}(\phi) = -D \cdot \nabla\phi \tag{1.4}$$

where $\nabla\phi$ is the concentration gradient and D is the collective diffusion coefficient. Near the contact line there is a higher particle concentration and, many-body direct and hydrodynamic interactions have to be considered to correctly describe the collective diffusion behavior (105). This way, D also reveals a dependence with concentration $D(\phi)$. Merlin et al. (47) reported how $D(\phi)$ for a suspension of charged nanoparticles is higher than the particle self-diffusion coefficient. In hard-sphere suspensions, the hydrodynamic interaction between the particles slows down their diffusional motion and almost cancels the increase of osmotic compressibility (see Figure 1.11).

---

[b] Rate at which macroscopic spatial inhomogeneities in particle distribution relax (102). The movement of particles is regarded as a whole rather than individually.

[c] Individual motion of one particle in a suspension produced by impacts of the solvent molecules (103).

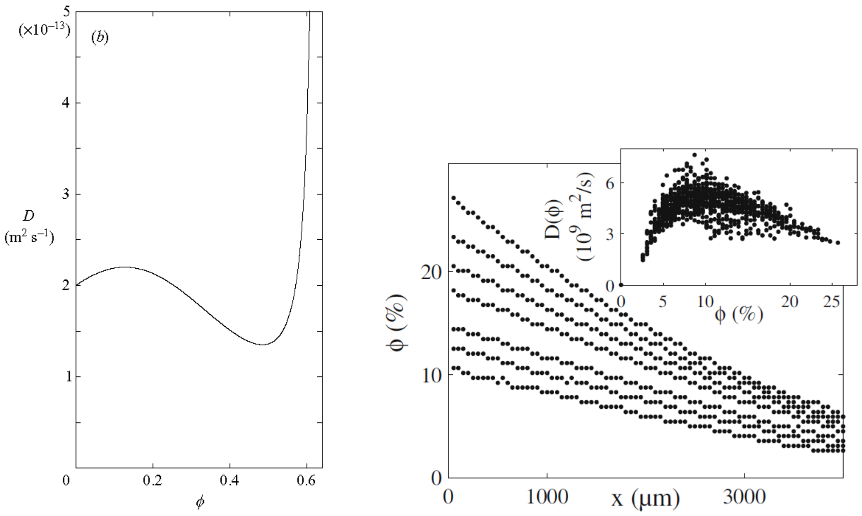

(a) (b)

Figure 1.11: Dependence of the collective diffusion coefficient $D(\phi)$ with particle concentration in suspensions of: (a) hard-spheres (*104*) and (b) charged particles (inset) (*47*).

However, in highly charged suspensions at low concentrations, the hydrodynamic interaction may even enhance diffusion. At intermediate concentrations, there is a complex interplay between electrostatic repulsion and hydrodynamic interactions. Close to the random-close packing fraction, although the assembly of interacting particles still presents a finite permeability, the osmotic compressibility due to interparticle direct interactions diverges. Due to this, the collective diffusion coefficient rapidly diverges around the maximum packing fraction (*106*, *107*).

Collective diffusion tends to equilibrate the loss of solute concentration in bulk produced by the evaporation-driven flow that accumulates particles close to the triple line. This way, at least two opposing flows may occur in a pinned evaporating drop of colloidal particles (*108*). In absence of other significant flows of different origin, the competition between both convective and diffusive flows might dictate the final deposit shape (*109*) or even the suppression of deposit (*109*, *110*), if the particles diffused away from the contact line. However, the own concentration gradient also affects the diffusive flow as Eq. 1.4.

1.3.2 Colloidal Brazil nut effect

Particle charge can also alter the behavior of particles in suspension at a very-low ionic strength. A monodisperse colloidal suspension is usually considered as a one-component system. If their buoyant mass m is not negligible, the particles sediment. Under this conditions the particle number density $\rho(z)$ at a height z follows the Boltzmann distribution:

$$\rho(z) = \rho_0 e^{-z/L} \tag{1.5}$$

where ρ_0 is the concentration at $z = 0$, and $L = \kappa_B T/mg$ is the gravitational length in terms of the temperature T, the Boltzmann constant κ_B, the gravity acceleration g and the buoyant mass m. However, some studies have reported how this profile can be altered for a salt-free dispersion (*111*). This discrepancy comes from the competition between potential energy and entropy, and further, the role of the ions in such conditions. Rather than a one-component system, ions must be taken into account in the colloidal suspensions. Co- and counter-ions diffuse through a medium seeking to maximize their entropy and homogeneity. This way, to maintain the electroneutrality free counter-ions might "lift" the particles by repelling the counter-ions adsorbed onto its surface. This interaction is known as "entropic lift" and it produces further stability in colloidal suspensions.

Figure 1.12: Size separation in vibrated systems where large particles rise to the top while smaller ones sink (*112*).

Size segregation of polydisperse macroscopic spheres (such as nuts or stones) has been widely studied (*113*–*115*). In 1930s, a size segregation was observed in the Brazil nuts under shaking. This effect is due to the lowering of the mass center of the mixture by filling the gaps with the smaller nuts (*116*). This results in a size segregation where bigger nuts "rise" while smaller ones are "pushed" downwards (see Figure 1.12). This effect has its equivalent in charged colloidal particles. When a binary mixture of colloidal particles with different charge and mass is studied, a charge-driven segregation can be observed (*117*) resembling the size segregation observed in granular matter. This way, charge-mass ratio may rule the behavior of particles in a colloidal suspension and thus alter the convective-capillary self-assembly.

Part I

Driven Evaporating Menisci

CHAPTER 2

Materials and methods

2.1 Substrates

We employed glass microscope cover slips (0.1mm-thick, 60x24 mm^2, Menzel-Glaser) and polymethylmethacrylate (PMMA, 1.1mm-thick, CQ grade, Goodfellow) as substrates for the deposit formation. We selected these materials by their different and stable wettability response, transparency and purity degree. To obtain substrates of similar dimensions, the PMMA sheets was adequately cut into pieces of 60x24mm^2. Before each experiment, the PMMA surfaces were cleaned ultrasonically in a detergent solution (Micro90) for 10min, followed by a prolonged ultrasonic rinsing in Milli-Q water (20min). To obtain different stable wettability properties on glass substrates, the cover slips were subjected to three different protocols:

- (Untreated) Glass. Sonication during 15 min in the following solutions: Micro90 solution, 70% (v/v) acetone, 70% (v/v) ethanol, distilled water and finally generous rinses of Milli-Q water.
- Plasma-Treated Glass (PTGlass). The Glass substrate (clean cover slip) was introduced into an argon plasma asher (Emitech K1050X) during 15 min at 25W. With this process, all organic components were volatilized leading to a very clean surface (*118*).

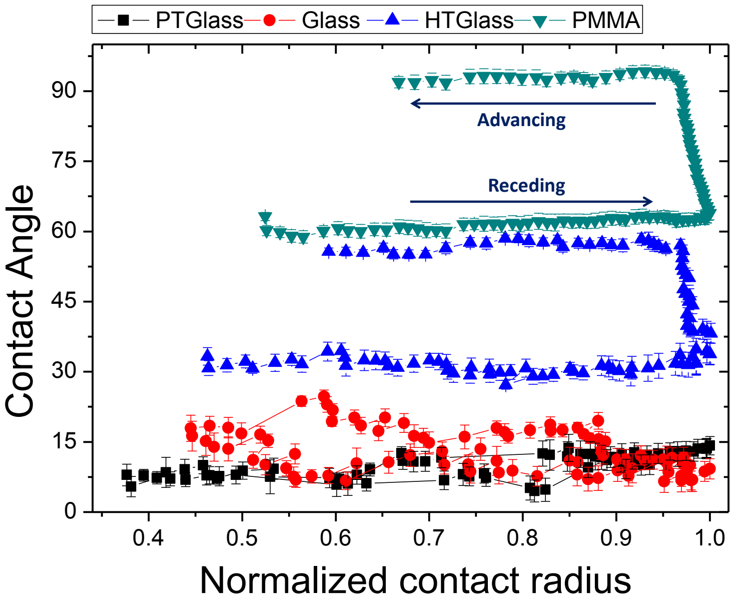

Figure 2.1: Contact angle in terms of dimensionless contact radius of the glass and PMMA substrates measured with the captive bubble method. The arrows indicate the direction of the air injection/suction process.

- Heat-Treated Glass (HTGlass). The Glass substrate was introduced into an oven at 200°C during 15 min. With this treatment we expect to dehydrate the surface, affecting the substrate wettability properties.

Roughness of the substrates was measured using the white light confocal microscope (see Section 2.3). The values obtained for the root mean square roughness on a window of 209x285 μm^2 were 6.5nm and 120nm for glass and PMMA, respectively.

To characterize the substrate contact angle hysteresis, we measured the water advancing (θ_a) and receding contact angles (θ_r) using the captive bubble technique (*119*). We employed this method due to the low receding contact angle of the glass substrates (lower than 20°). Moreover, captive bubble experiments are closer to the experimental conditions of the driven menisci experiments: moving contact lines on a previously wet surface. In this technique, a growing and shrinking bubble was formed against the substrate. A 0.5mm hole was produced at the center of the substrates before each treatment with a pulsed laser (Laser E-20 SHG II, Rofin), allowing the injection/suction of air. The bubble volume was varied with a 250μl syringe connected to a micro-injector (PSD3, Hamilton). We used Milli-Q water at room temperature for all experiments. A "seed" bubble of 20μl was placed below the hole before each experiment to form a centered large bubble. Next, at a quadratic flow rate (*120*), an air volume of 100μl was added or removed from the bubble. Details of the experimental set-up used for contact angle measurements is described elsewhere (*119*). Bubble profiles were analyzed with the Axisymmetric

Substrate	θ_A (°)	θ_R (°)
PMMA	93 ± 1	62 ± 1
HTGlass	57 ± 1	31 ± 1
Glass	16 ± 4	10 ± 3
PTGlass	8 ± 2	7 ± 2

Tabla 2.1: Advancing and receding contact angles of the substrates in this work. The acronyms correspond to Heat-Treated Glass and Plasma-Treated Glass.

Drop Shape Analysis-Profile (ADSA-P) technique. With this approach, all the bubble parameters such as contact angle, contact radius, area, volume and surface tension were extracted. The advancing and receding contact angles were averaged over the values of contact angle observed when the contact line was uniformly moving (see Figure 2.1).

Different values of contact angle hysteresis were obtained with the substrates studied in this work (see Table 2.1). The HTGlass substrate presented the greatest values of hysteresis and contact angle (advancing and receding) because of the controlled dehydration after heating. In still air, surface dehydration of glass may decrease its surface energy because the density of hydroxyl groups (silanols) on the glass surface decreases. Otherwise, the PTGlass substrate presented negligible hysteresis and very low contact angles because of the ashing of pollutants produced during the plasma treatment. The new high energy surface was very susceptible to adsorb water. Instead, the Glass substrate revealed low contact angles but greater hysteresis than the PTGlass substrate (see Table 2.1).

We illustrate the receding contact angle of each substrate from the capillary rise (see Section 2.3). We introduced two parallel substrates, separated by a distance of 1mm, into a reservoir of Milli-Q water. A column of liquid is formed between the substrates by capillary rise. Figure 2.2 shows the receding of the contact line on the different substrates prepared driven by pumping the

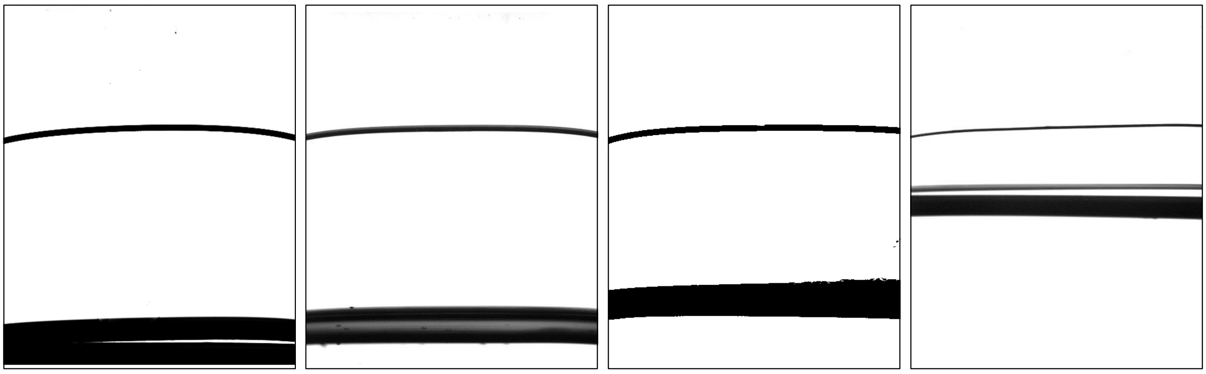
(a) PTGlass (b) Glass (c) HTGlass (d) PMMA

Figure 2.2: Images of the water column formed by capillary rise between the substrates used in this chapter. The height of the column is related to the receding contact angle as Eq. 1.2.

water of reservoir. The height of the liquid column depends on the contact angle as Eq. 1.2. Different height was found as the receding contact angle of each substrate.

2.2 Nanoparticle suspensions

2.2.1 Surface electric charge

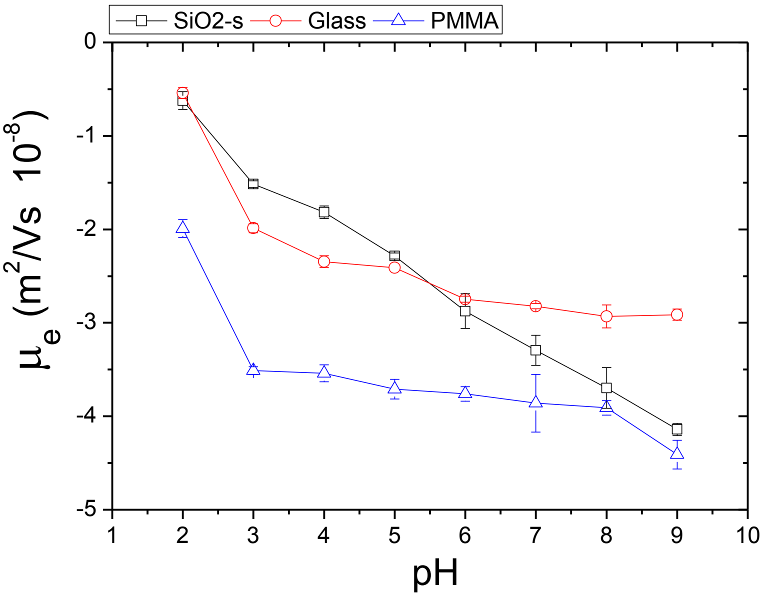

Figure 2.3: Electrophoretic mobility as a function of pH of the SiO2-s, glass and PMMA nanoparticles. The electrophoretic mobility measurements were performed at 0.01% (w/w).

We used commercial aqueous suspensions of spherical nanoparticles (see Appendix A) because we required significant solid concentration and volume of sample. We selected particles with similar properties (wettability and electric charge) to the substrates prepared in Section 2.1. We purchased glass (AttendBio Research, 50nm), PMMA (Microparticles, 105nm) and silica nanoparticles (SiO2-s, 90 nm, kindly supplied by Klebosol). The maximum particle concentration (w/w) of these suspensions was 50% (w/w) for glass and SiO2-s, and 5% (w/w) for PMMA. The electric charge of the glass and SiO2-s particles is due to the dissociation of surface silanol groups in aqueous medium. Instead, the PMMA particles are electrostatically stabilized through surface sulfate groups from the initiator during the polymerization process. The PMMA particles are roughly constantly charged because the strongly acidic sulfate groups are fully dissociated in all relevant solution conditions.

To change the electrostatic double layer interactions (abbreviated below as electrostatic interactions), we varied the particle electric charge through the medium pH (*83*). Particle suspensions were diluted in buffer solutions of low ionic strength (≤15mM) by dialysis. A sample of 10 ml (at maximun concentration for the PMMA particles (5% w/w) and at 25% (w/w) for the SiO2-s particles) of particle suspension was dialyzed against 1 l of buffer solution for 5 h and next, the buffer solution was exchanged twice. We used a dialysis tubing cellulose membrane (D9652, Sigma Aldrich) with a size pore in the range of 1-2nm.

We measured the particle electrophoretic mobility as function of pH value using a Zetasizer Nano device (Malvern, 4mW He-Ne laser, 633nm wavelength). The particle concentration used in all the electrophoretic mobility measurements was 0.01% (w/w). The results are shown in Figure 2.3. The three different nanoparticles were negatively charged for all the pH values studied. Effective electric charge of the glass and SiO2-s nanoparticles at pH2 was very low and for the PMMA nanoparticles it was weak. Instead, all particles presented a maximum unsigned charge at pH9.

2.2.2 Surface tension

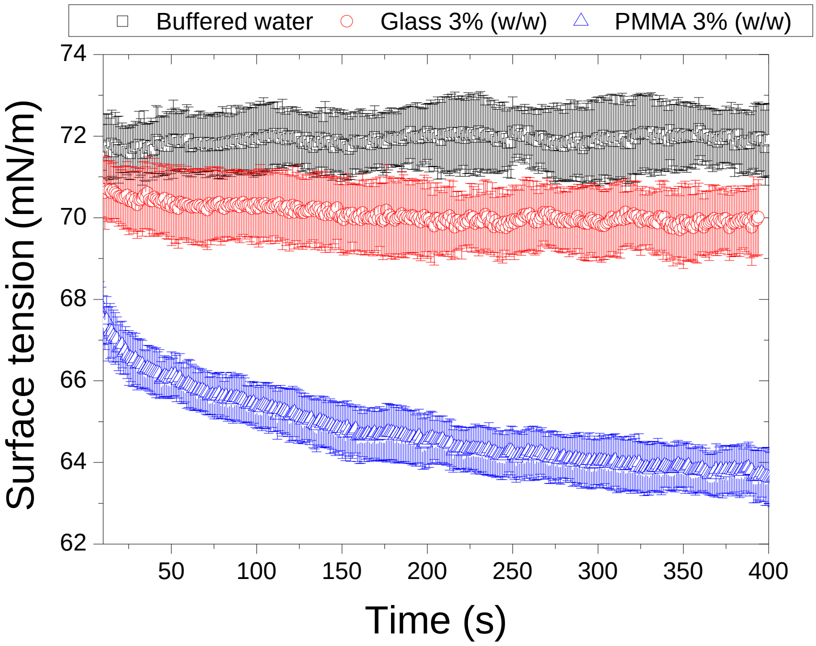

Figure 2.4: Surface tension over time for three different liquid: water, glass suspension and PMMA suspension at pH9. The Glass particles (red) are scarcely surface active. The PMMA particles (blue) were adsorbed at the interface rather than the Glass particles.

We performed pendant drop measurements to study the interfacial activity of the nanoparticle suspensions at 3% (w/w) and pH9 (see Figure 2.4). We concluded that the nanoparticle adsorption at the liquid-air interface of the meniscus was negligible for the glass nanoparticles and very fast although nearly significant for the PMMA nanoparticles (max. surface tension reduction of 17%). We also examined the effect of nanoparticle concentration on the surface tension. We performed pendant drop measurements for increasing concentrations. In Figure 2.5 we plot the surface tension in terms of the solid concentration for the SiO2-s and PMMA suspensions. From these results, we conclude that high particle concentrations significantly decreases the surface tension of the suspension, with a reduction of 27% for the densest system (SiO2-s, 50%) highest concentration of the SiO2-s. We found that pH was not relevant for surface tension measurements because at pH9 and pH2 surface tension exhibited the same behaviour (see Figure 2.6).

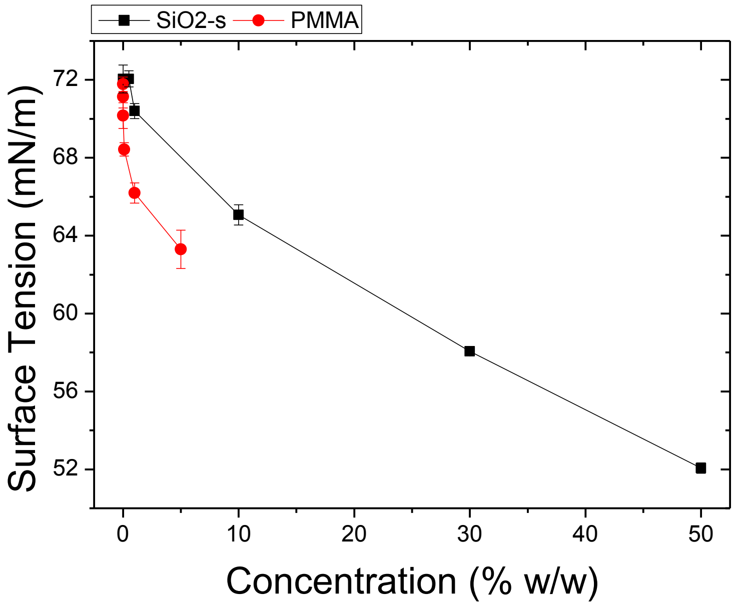

Figure 2.5: Surface tension in terms of the solid concentration for the SiO2-s and PMMA suspensions. The measurements were carried out at room temperature and pH9 to enhance the plausible effects due to surface charge.

We assumed that thermal Marangoni flow was negligible at room temperature in our aqueous systems. From surface tension measurements (see Figure 2.4 and 2.5), we also discarded other sources of Marangoni stress such as surfactant concentration gradients.

2.2.3 Viscosity

Furthermore, we measured the viscosity of SiO2-s for increasing concentrations. Shear viscosity measurements were carried out in a stress controlled rheometer (MCR302, Anton Paar) using a cone-plate geometry (50 mm diameter, 1°). Experiments were performed in isothermal conditions (20°C) after appropriately erasing the mechanical history of the samples. The protocol consisted in three differentiated steps. In the first step the sample was pre-sheared at a constant shear rate (100/s) during 60 seconds. Next the sample was equilibrated, at rest, during 60 seconds.

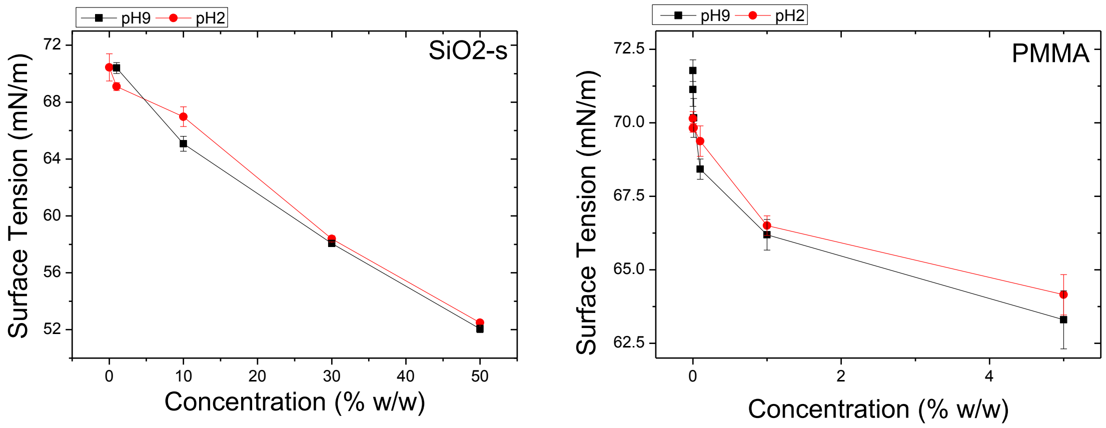

(a) (b)

Figure 2.6: Surface tension in terms of the solid concentration for the two charged states: (a) pH2 and pH9 for the SiO2-s and (b) the PMMA suspensions.

Finally, a shear rate ramp was performed from 1 to 1000 /s during 150 s. The measuring point duration was 5 s. All samples exhibited a Newtonian-like behavior. Data reported in this work were obtained from the arithmetic average of the viscosity between 10 to 1000 /s. From Figure 2.7, the viscosity remains constant up to a concentration of 25% (w/w).

2.2.4 Collective diffusion coefficient

In an evaporating process, where the particle concentration increases, the Stokes-Einstein equation is not valid (*47*). Due to this, we examined the "free" diffusion of the nanoparticles in suspension, not confined. We measured the diffusion coefficient of the nanoparticles used in the driven menisci experiments with a particle size analyzer (ALV-GmbH, 3 mW He-Ne laser, 632.8nm wavelength) operating in back scattering mode (detector at an angle of 173° with respect to the laser) to suppress multiple scattering contributions in concentrated systems. The measurements were performed over the range of particle concentration 0.1-20% (w/w) and for the weakest and strongest interparticle electrostatic repulsions (pH2 and pH9, respectively).

2.3 Exprimental set-up

To produce the nanoparticle deposition in similar conditions to the well-known dip coating technique (*121*), we controlled the receding motion of a meniscus confined between two vertical parallel plates. The sustained evaporation plays a very important role in the drying of nanoparticle suspensions at driven receding contact lines (see Section 1.2). However, evaporation and

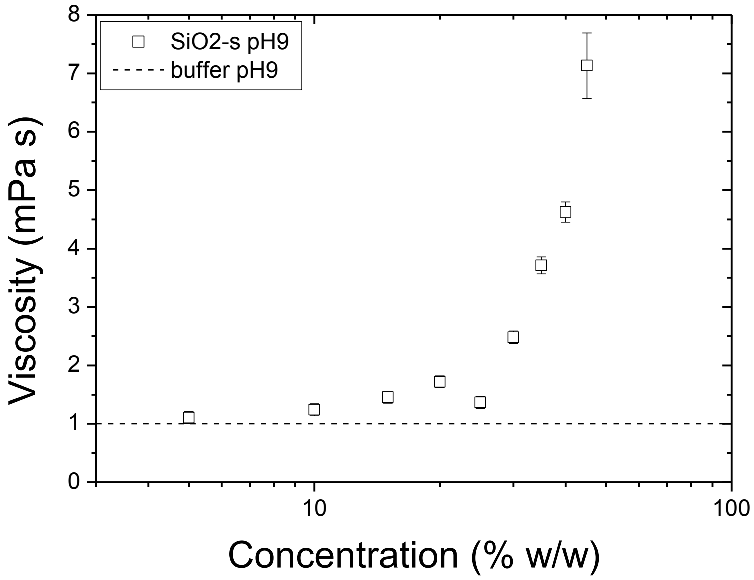

Figure 2.7: Viscosity in terms of the solid concentration of the SiO2-s suspensions. Experiments were performed at 20°C and pH9.

contact line dynamics can be decoupled at the macroscopic scale (*122*). Our experimental device is shown in Figure 2.8. The substrates were placed in a glass cuvette (Hellma) with dimensions 50x50x10mm^3. The cuvette was closed but not sealed. The substrates were carefully separated at the upper and lower positions to maintain a distance of 1mm. The cuvette was filled with 15ml of nanoparticle suspension and the meniscus was formed between the two parallel substrates by free capillary rise, which corresponded to the advancing meniscus configuration. To achieve receding configuration, a small amount of liquid was manually removed from the reservoir until the contact line started to receding. Next, the motion of the meniscus was driven by pumping the suspension with a syringe (Hamilton, 12.5ml) at constant flow rate (3.47μl/s) using a microinjector (PSD3, Hamilton).

To monitor the contact line dynamics of the driven receding meniscus, we acquired images with a CCD (Retiga 1300, QImaging, 16 μm/pixel) and back-light illumination at 1.7 fps during the entire experiment (approx. 1 hour). The images were analyzed using the software Mathematica. This way, the contact line position was determined as a function of time and the contact line velocity was estimated. During the entire experiment, the meniscus contact line and the reservoir level moved at the same velocity separated by a fixed distance (receding capillary rise, see Figure 2.9). We examined the central region of the substrates, far from the borders, which corresponded to a maximum displacement of contact line of 14mm (for the glass substrate). This way, upon minimum evaporation (closed cuvette, Relative Humidity:RH=94-98%), we reproduced uniformly moving contact lines at 7μm/s, which agreed with the nominal linear velocity (6.9μm/s). Due to

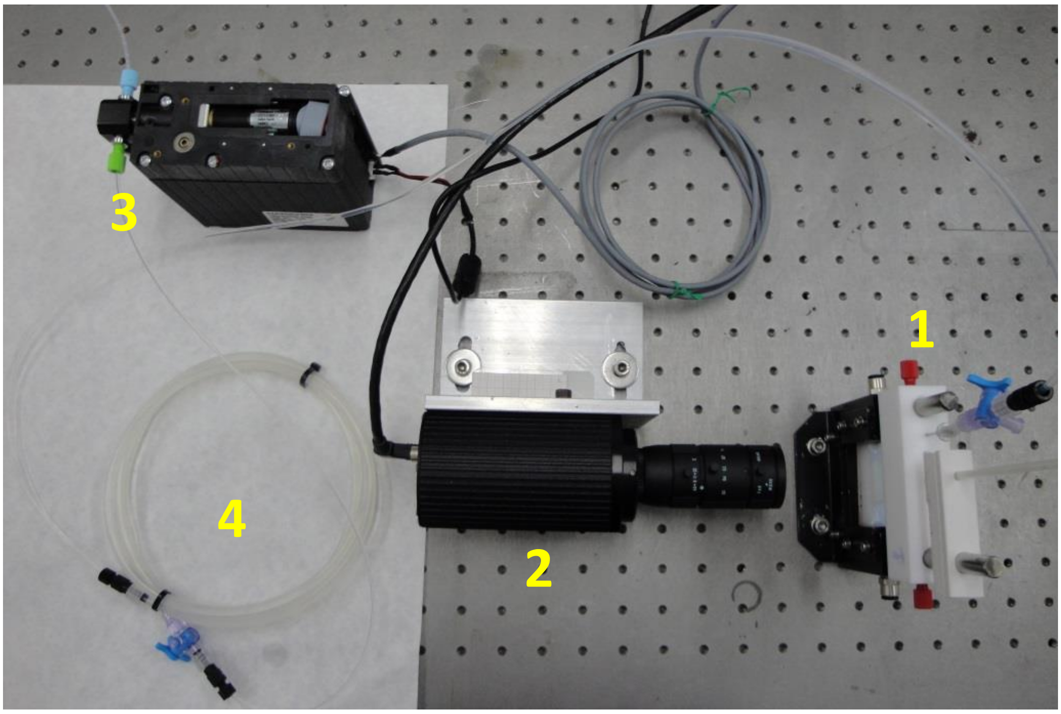

(a)

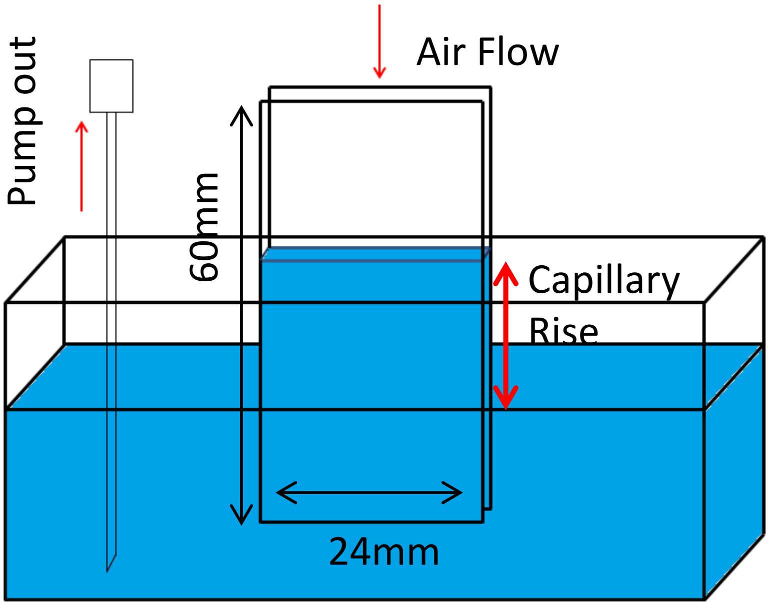

(b)

Figure 2.8: (a) Top-view of the driven menisci set-up: 1) Cuvette holder, 2) input of dry air, 3) output of nanoparticle suspension connected through a long PTFE coil, filled with water, to the microinjector terminal, 4) CCD Camera, 5) long PTFE coil and 6) microinjector and syringe. (b) Detail on the cuvette-plates configuration.

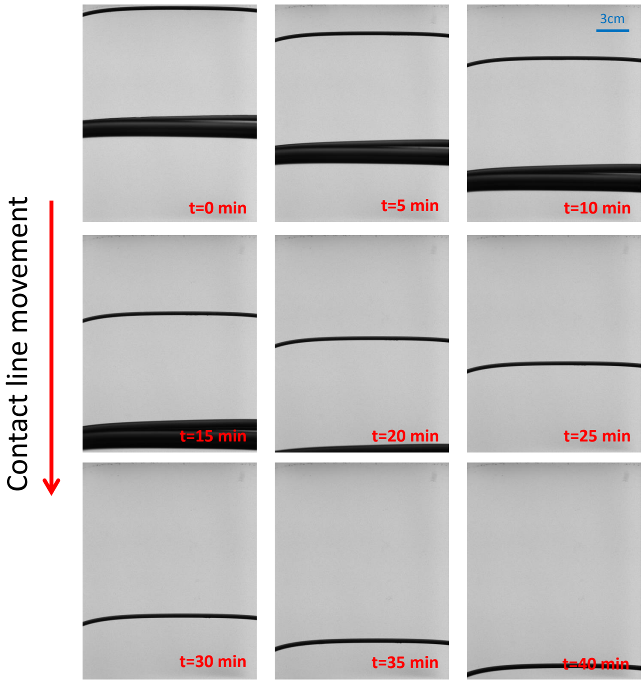

Figure 2.9: Succession of images obtained with our set-up during an entire experiment. It is noteworthy how the meniscus position can be identified with the thin line, while the wide defines the reservoir level. The height of the liquid column remains constant during the entire experiment.

optical magnification and image resolution of our set-up, the stick-slip motion of the contact line was not noticeable at the concentration of 3% (w/w).

We injected inside the cuvette dry air (RH=2%), previously passed through drierite (Sigma-Aldrich) to reduce the actual RH up to ≈65-67%. All experiments were carried out at room temperature (20-23°C). Upon these experimental conditions we observed that the contact line velocity due to evaporation was roughly 1μm/s (see Figure 2.10). Contact line dynamics in our experiments is ruled by the interplay of the local evaporation, at the microscopic scale, and the driven motion. However, the overall evaporation and the dynamics of the whole interface are de facto decoupled.

The final deposits were analyzed using a white light confocal microscope (PLμ, Sensofar Tech S.L.) with 50x and 20x objectives (Nikon, 285.8 x 209.6μm^2 and 694.4 x 510.09μm^2) and occasionally with a 10x objective (Nikon, 1.39 x 1.02mm^2). To visualize the deposits at lower scale, we utilized an atomic force microscope (Nanoscope IV, Veeco). The deposit analyzed correspond the central part of the substrate, to avoid effects of border and of the initial pinning (at the beginning of the deposit) and reminiscent drop (at the end of the deposit). From the deposit profiles we evaluated three linear dimensions: height (H), width (W) and the space between stripes (G), as illustrated in Figure 2.11. An average value of each dimension was obtained from,

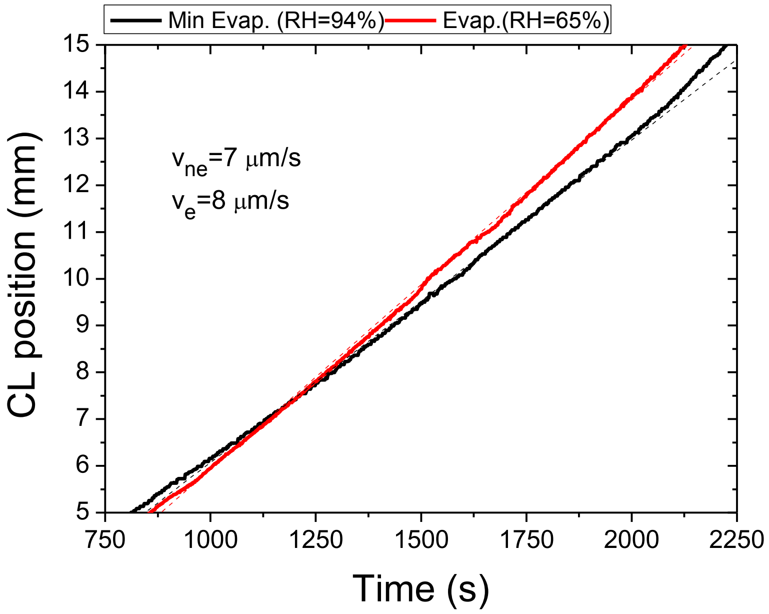

Figure 2.10: Position of the contact line versus time for two experiments: One with the cuvette closed (not sealed) without any air flow (RH≈ 96% in black), and another with a constant flow of air previously dried with drierite (RH≈ 65% in red). Zero position was set to the actual position at time 0s when the meniscus was at the highest position. As the meniscus receded, the downward motion of the contact line was taken as a positive displacement. We could calculate the CL velocity from the slope of each graph. The difference of velocities between both experiments was associated with the velocity due to the evaporation.

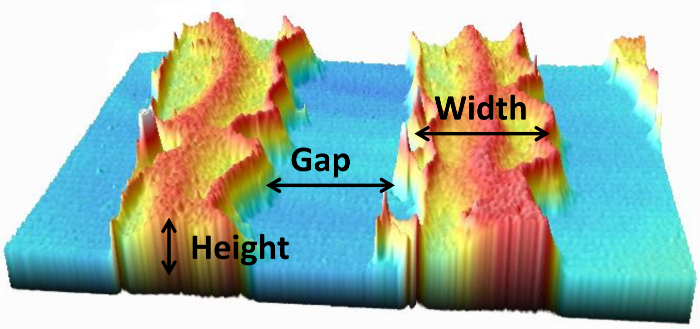

Figure 2.11: Profile dimensions for the stripe-like patterned deposits: height, width and gap.

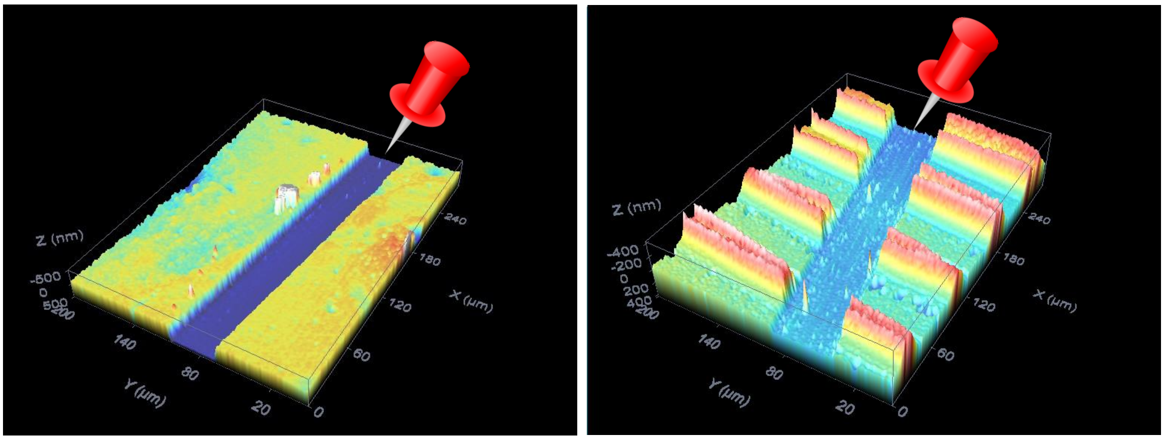

(a) (b)

Figure 2.12: Topography illustrating the method to estimate the amount of mass deposited. Relevance of this technique can be seen because an apparently flat surface (a) can sustain certain thickness.

at least, three profiles. Maximum deviation in these values was $\pm 0.1\mu$m.

To obtain a rough estimate of the amount of mass deposited (number of particles) in each case, we measured the area of the corresponding longitudinal profiles over a fixed substrate region and taking as zero level in height the bare surface of the substrate. To this end we performed a thin scratch on the surface with a small metallic tip (see Figure 2.12).This way we could measure the area sustained by each profile (A). Next, we computed the effective volume of the deposit by multiplying the former area by the substrate width (d=24 mm), because the patterns usually covered all the substrate surface, and the typical deposition length (l=20 mm). This effective volume was divided by the volume of a single particle. We assumed that there were no gaps between the particles deposited (see Eq. 2.1):

$$N_d = \frac{A \cdot l \cdot d}{4/3\pi r^3} \tag{2.1}$$

CHAPTER 3

Effect of the wettability properties of the substrates

In this chapter, we experimentally examined the roles of substrate contact angle hysteresis and receding contact angle in colloidal patterning by convective assembly. We formed driven evaporating menisci like in the dip-coating technique (see Section 2.3). In this part of the study we used the smooth glass substrates treated with three protocols (see Section 2.1) and particles with similar nature as for the substrates (see Section 2.2). For fixed withdrawal velocity, evaporation conditions and particle concentration, we analyzed the morphology of the deposits formed on each substrate. Deposits consisting in periodic horizontal striped assemblies of particles (*41*, *122*) were spontaneously formed with different features as the wettability properties of the substrate studied.

3.1 Results and discussion

Noticeable differences in the deposit morphology were observed as the substrate used. The particle concentration was fixed at 3% (w/w). Figure 3.1 shows different particle deposits for the Glass-Glass system (substrate-particle). A clear transition from a stripe-like pattern to a film was obtained. Very well-defined and separated stripes were observed over the HTGlass substrate. The separation between stripes and their width were reduced on the Glass substrate. Surprisingly, analyzing the profiles of the topographies, an irregular film was observed over the PTGlass substrate (see Figure 3.2a). This behavior was validated with the SiO2-s nanoparticles of greater size (see Figure 3.2b). The topographies for the deposits obtained with SiO2-s are illustrated in Figure 3.3. Deposit height and particle size were correlated because the deposits formed with the SiO2-s nanoparticles were higher than with the glass nanoparticles.

A quantitative analysis of the stripe dimensions (height H and width W) and the spacing between them (gap G) was accomplished. Firstly, a clear dependence of the deposit height with the substrate receding contact angle was found. Figure 3.5a shows how the highest deposits were obtained on the HTGlass substrate (the substrate with the greatest receding contact angle) followed by the Glass substrate. The deposit height agreed with the particle size because the deposits formed with the SiO2-s nanoparticles were higher than with the glass nanoparticles. The minimum height of deposit was reached on the PTGlass substrate where an unresolved monolayer was found with both glass andSiO2-s nanoparticles.

Secondly, we analyzed the deposit shape using two parameters: H·W (Figure 3.5b) related to the material amount contained in each stripe, and H/W (Figure 3.5c) related to the “sharpness” of the stripes. We found that the stripe shape remained constant for each particle size. The confinement of particles as they were pushed towards the triple line was more pronounced for lower contact angles. This explains that the smaller particles formed flatter stripes because they could penetrate further through the interfacial wedge. As expected, the amount of deposited mass increased as the substrate receding contact angle.

Finally, the coverage degree ($W/(W+G)$) enabled to quantify the horizontal deposition on the substrate (see Figure 3.5). When this parameter reached the value 0.5, the substrate was half covered with particles. On the other hand, values lower than 0.5 indicate that the stripes were thinner than the gap between them. This just happened with the HTGlass substrate although coverage degrees greater than 0.5 were observed for the Glass substrate. However, the PTGlass substrate was partly covered with particles following branch-like or fingering structures (see Figure 3.4).

The pattern-to-film transition observed (see Figure 3.1) can be explained in terms of contact angle hysteresis and contact line dynamics. It is known that the contact line of evaporating drops or menisci may describe a stick-slip motion that will determine the formation of periodic patterns (see Appendix B). The time lapsed while the contact line remains static during the evaporation is known as *pinning time* and it becomes important for the pattern morphology (*40*). On a substrate with greater contact angle hysteresis, the system may be trapped in more metastable configurations and this way the triple line will be pinned longer. In driven evaporating meniscus

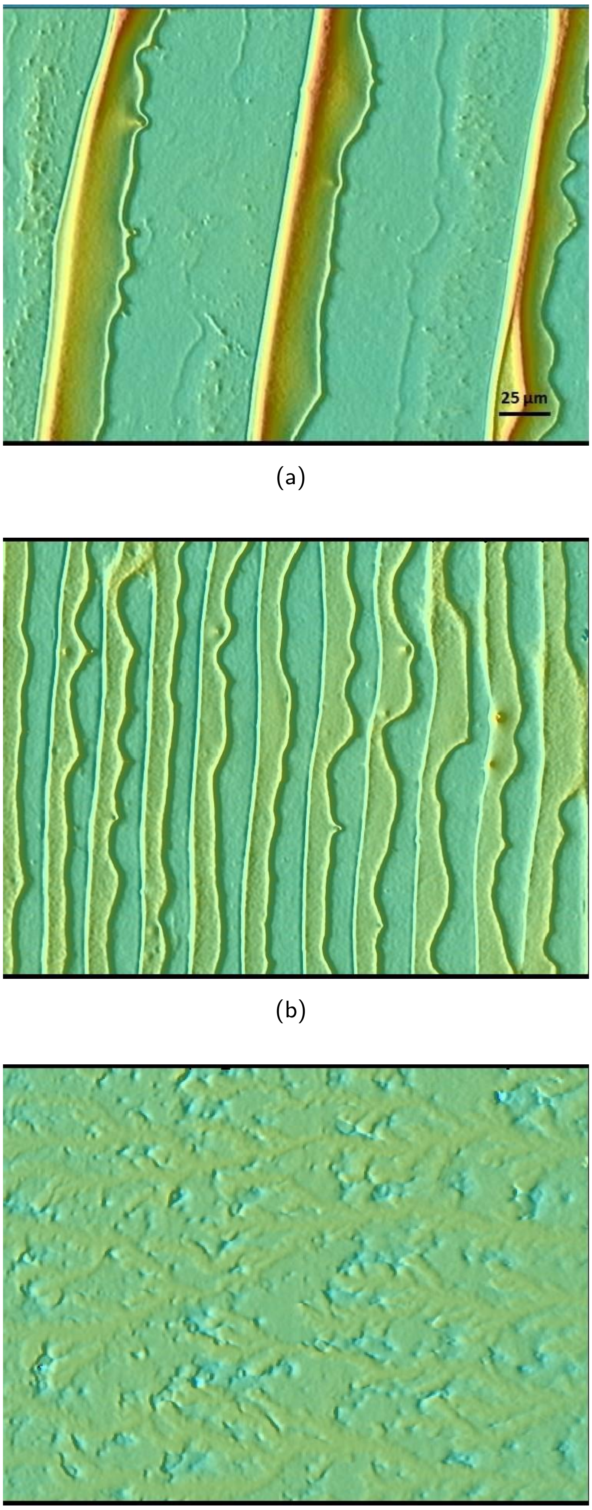

(a)

(b)

(c)

Figure 3.1: Deposits of glass nanoparticles formed on the (a) HTGlass, (b) Glass and (c) PTGlass substrates at 3% (w/w), pH2, RH≈65% and a contact line speed of 7 μm/s. Scale in Z in the topographies was set from 0 to 1 μm so that each color tone correspond to the same height.

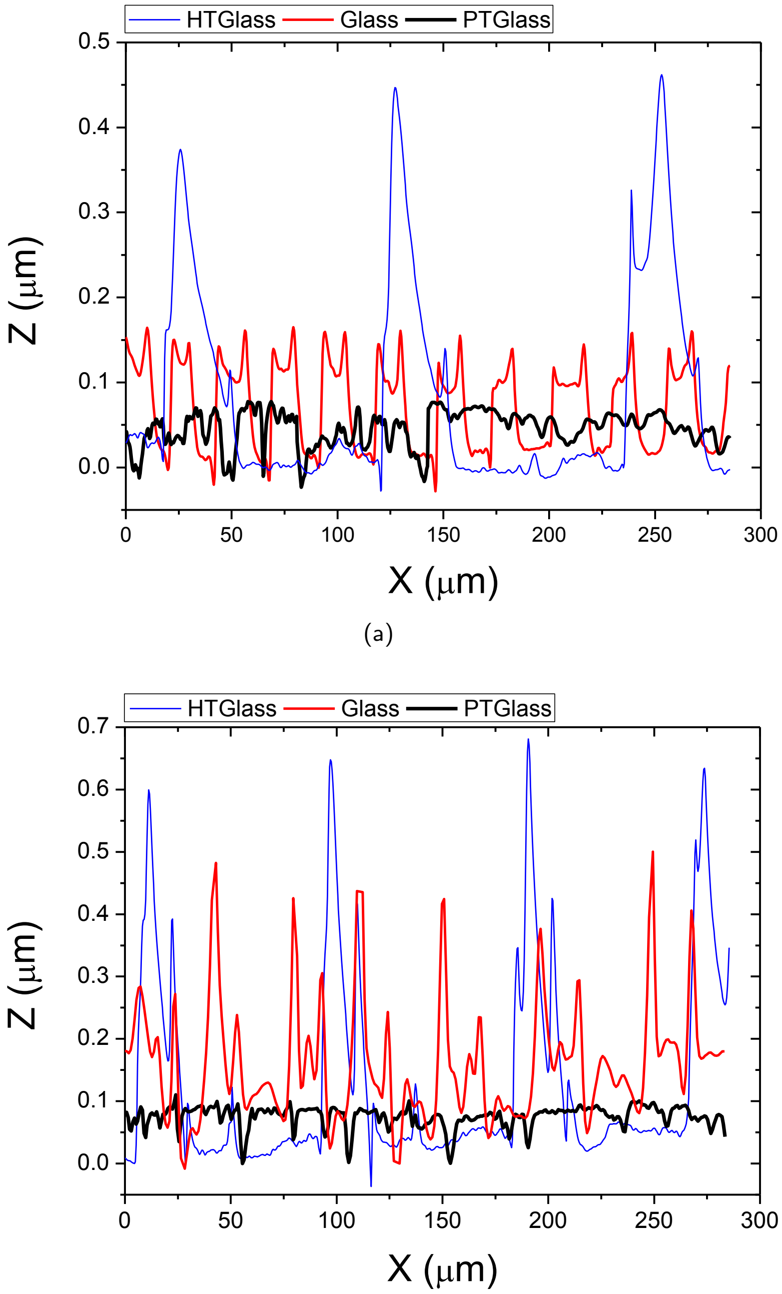

(a)

(b)

Figure 3.2: Profiles of the stripe-like patterns and film formed on the HTGlass, Glass and PTGlass substrates using (a) glass and (b) SiO2-s nanoparticles at 3% (w/w) and pH2.

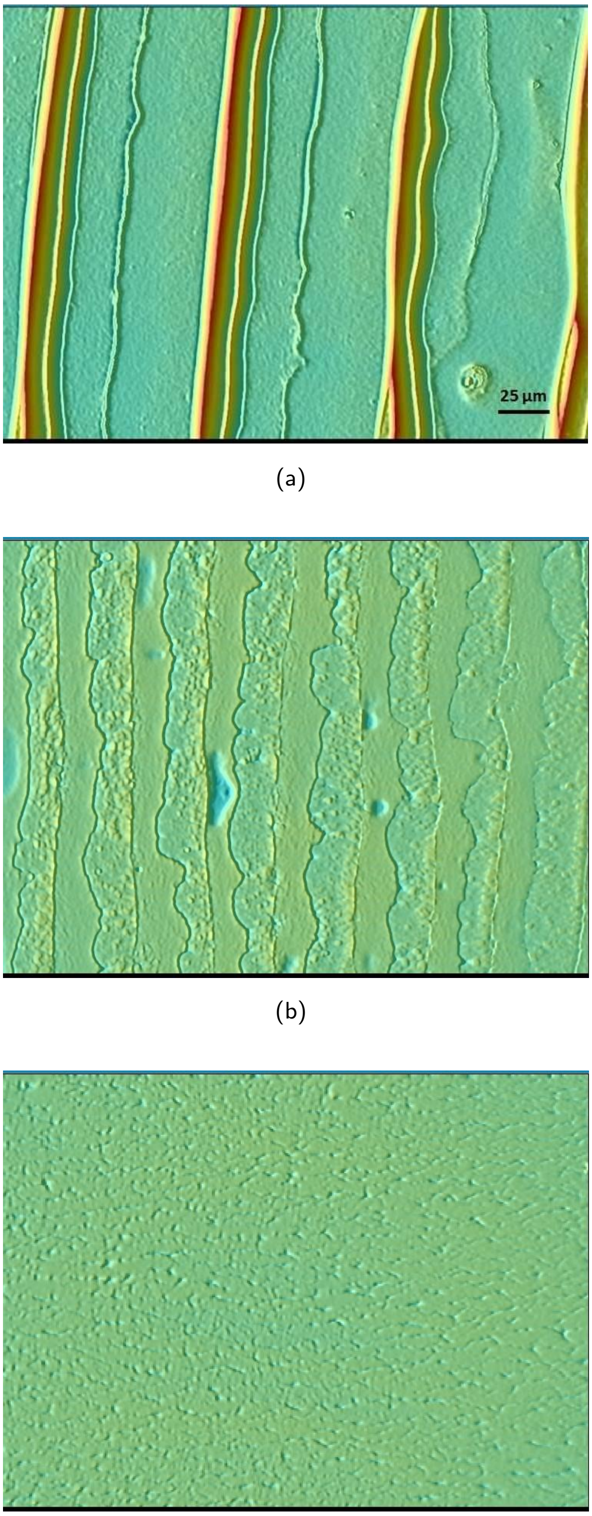

(a)

(b)

(c)

Figure 3.3: Deposits of SiO2-s nanoparticles formed on the (a) HTGlass, (b) Glass and (c) PTGlass substrates at 3% (w/w), pH2, RH≈65% and a contact line speed of 7 μm/s. Scale in Z in the topographies was set from 0 to 1 μm so that each color tone correspond to the same height.

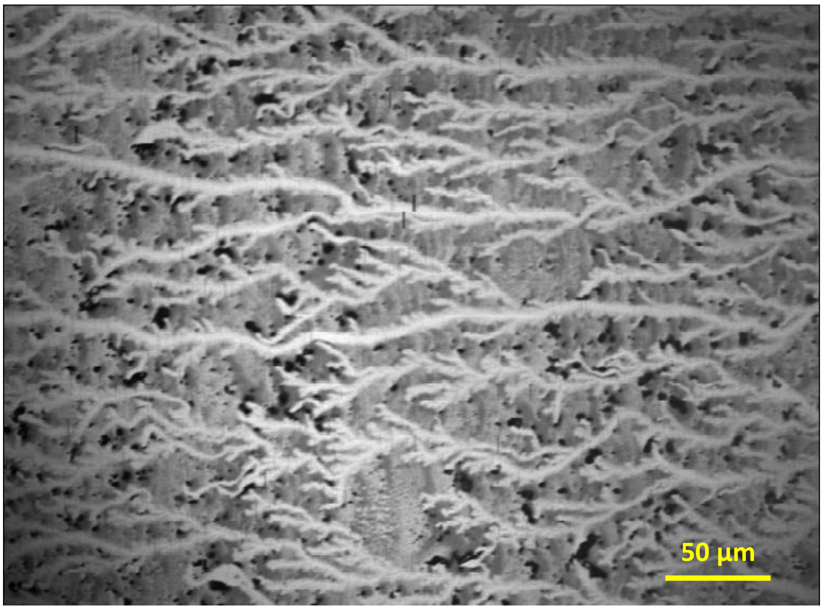

(a)

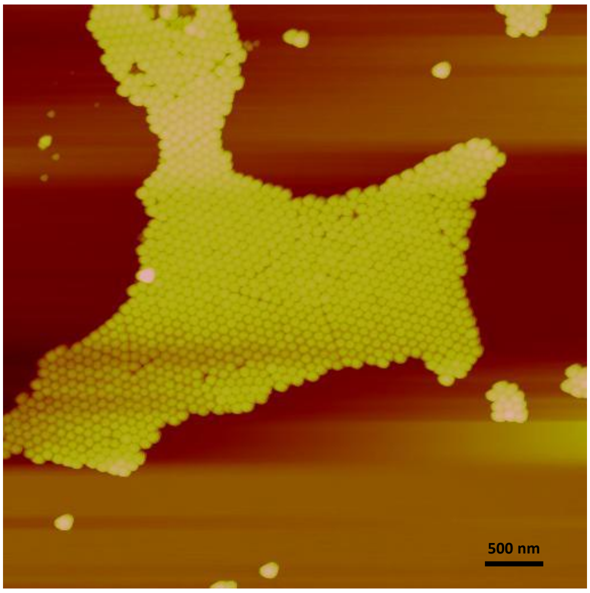

(b)

Figure 3.4: Detail of the deposits formed on PTGlass substrates: (a) optical image of branch-like deposits formed with glass nanoparticles and (b) AFM image of an island formed with SiO2-s nanoparticles.

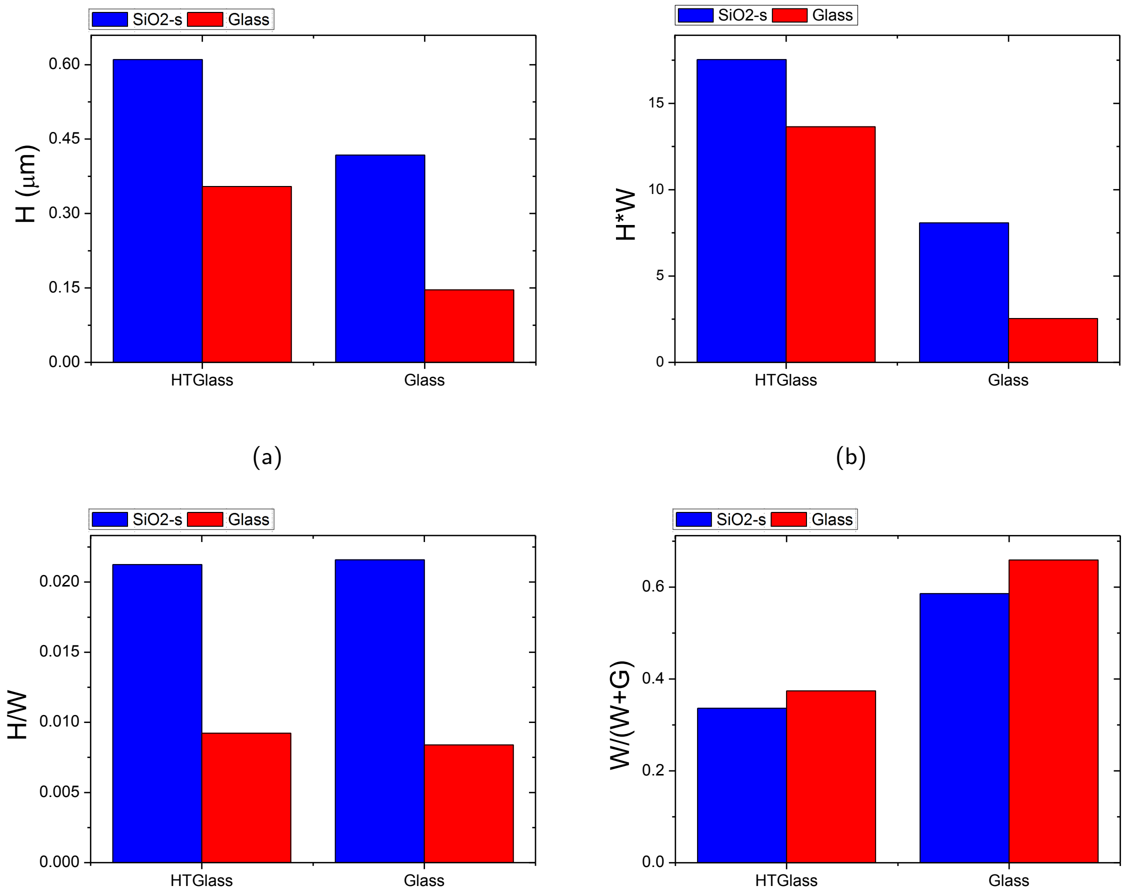

(a) (b)

(c) (d)

Figure 3.5: Analysis of different features of the patterns formed on the HTGlass and Glass substrates: (a) height, (b) deposit shape, (c) material deposited and (d) coverage degree. An average value of each dimension was obtained from, at least, three profiles. Maximum deviation in these values was ±0.1μm.

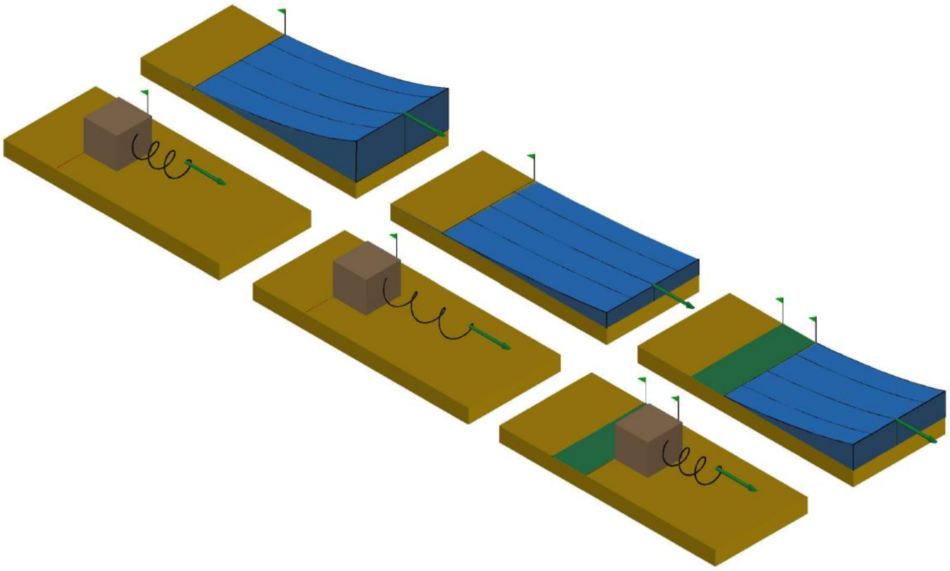

(a)

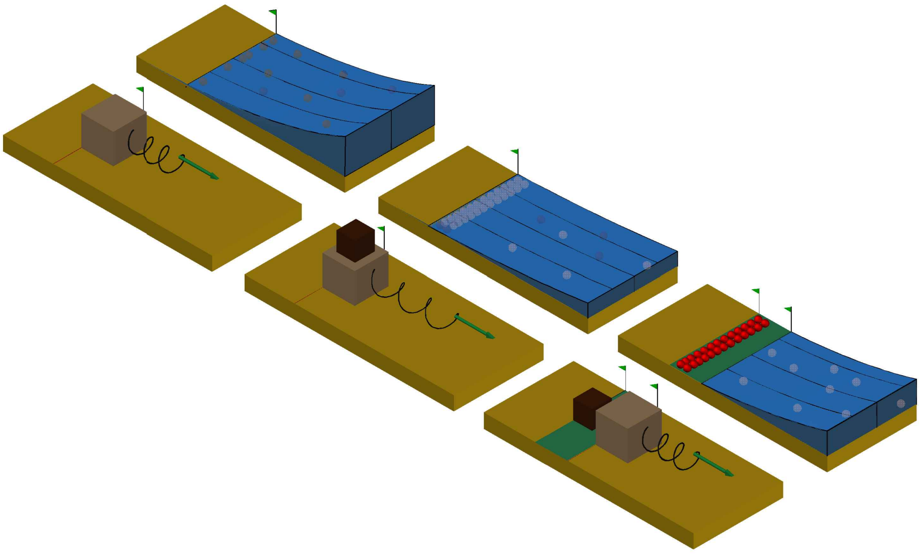

(b)

Figure 3.6: Mechanical analogy of driven receding contact lines. A block connected to a spring whose free end is moving at constant speed describes a stick slip motion. This motion resembles the behavior of the driven menisci due to (a) contact angle hysteresis and (b) self-pinning.

experiments, it is necessary to take further into account the driving force. In the context of guided contact lines, depinning may be better understood in terms of static friction whereas the liquid surface tension acts like an elastic force. Like a block attached to a spring (see Figure 3.6a), if the free end of the spring is moving at constant speed, which emulates the suction in our set-up, the block will undergo a motion similar to the contact line motion. In this mechanistic interpretation, the substrate receding contact angle has no explicit role except for the strength of the evaporative flow and the "interfacial wedge" size. Two substrates with different contact angle hysteresis will correspond to two surfaces with different static friction coefficient. This way, if the contact line were pinned, once it begins to move again because of the suction of the liquid reservoir, it would jump certain distance up to reach a stable static configuration while the reservoir level decreases at constant speed. Greater values of pinning time (hysteresis) agree with larger gaps because the triple line must jump longer distances as happens in the HTGlass substrate (see Figure 3.1a). On the other hand, greater hysteresis leads to a greater pinning time and in consequence, more particles will be driven towards the contact line due to evaporation (self-pinning). This resembles the motion of the block connected to a spring but with a smaller block placed on the top of the first one. In this manner, due to the weight of the smaller block, the larger one will remain *self-pinned* (see Figure 3.6b). In this case, greater self-pinning time leads to higher deposits (see Figure 3.5a), provided that the "wedge effect" allows it. Finally, as contact angle hysteresis is decreased, pinning time is reduced and the stripes get closer and tend to be lower as happens with the Glass substrate. When hysteresis is nearly zero, such as in the PTGlass substrate, no pinning events take place and a film is formed (see Figure 3.1c). The suppression of the coffee-ring effect by contact angle hysteresis has been recently reported by Li et al. (*43*). In this scenario, once the particles are accumulated at the triple line, their number per unit of time (convective-capillary flow) seems to be secondary at driven receding contact lines with low capillary numbers. The occurrence of branches structures or islands rather than a complete monolayer of nanoparticles can be explained by local events of self-pinning (see Figure 3.4 and Appendix C).

3.2 Conclusions

Wettability properties of substrate have been found to be important for colloidal patterning with driven evaporating menisci. The strength of the evaporative-capillary flow at room temperature and RH $\approx$65% in each substrate studied (with different receding contact angle) seems to have a secondary role, as reported by Brutin (*123*). A transition from stripe-like deposit to heterogeneous film was reproduced by varying the wettability properties of substrate. The deposit dimensions increased as the substrate receding contact angle and contact angle hysteresis, although the ratio between deposit height and width remained constant for each particle size. The stripe-to-stripe distance was correlated to the substrate hysteresis due to the contact line pinning. Very low values of receding contact angle and nearly zero hysteresis enabled the formation of a particulate film. Further work should be addressed to optimize the production of colloidal patterns by changing the wettability properties of substrates.

CHAPTER 4

Effect of the particle collective diffusion

In this chapter, we study the effects caused by the collective diffusion of charged nanoparticles in the colloidal patterning. To decouple the sustained evaporation from the contact line motion, we conducted evaporation menisci experiments with driven receding contact lines similar to industrial dip-coating technique. This allowed us to explore convective assembly at fixed and low bulk concentration, which enabled to develop high concentration gradients. At a fixed velocity of driven triple line and a nanoparticle concentration, we explored a variety of substrate-particle systems where the particle-particle electrostatic interaction was changed (via pH) as well as the relative humidity and the receding contact angle using two substrates: glass and PMMA (see Section 2.1). Finally we examine the effect of nanoparticle concentration on the substrate patterning when the particle-particle interactions were minimized (pH2) and also when electrostatic particle-particle repulsion was enhanced (pH9).

4.1 Results and discussion

4.1.1 Diffusion coefficient of nanoparticles

Results of light back-scattering experiments with the glass and PMMA nanoparticles at pH2 and pH9 are shown in Figure 4.1. When the interparticle electrostatic repulsion was strong (at pH9 as Figure 2.3), we found that the diffusion coefficient increased as the particle concentration. However when the interparticle electrostatic interactions were weak (at pH2, see Figure 2.3), a smaller increase of diffusion coefficient was observed compared with the observed at pH9. It is known that, in photon correlation spectroscopy experiments (*124*), when the inverse of the scattering vector is much greater than the mean interparticle spacing (concentration dependent) then the measured intensity and its autocorrelation function are dominated by the collective diffusion of the particles. Due to this, for the size of particles studied, the range of concentration explored and the scattering angle and wavelength of our set-up, a crossover from self-diffusion to collective diffusion is actually measured. However, as expected, our results confirm that collective diffusion increases as particle concentration when the interparticle electrostatic repulsion is enhanced (*124*). This effect should be more remarkable during the arrangement of charged particles at the triple line in the driven receding meniscus experiments.

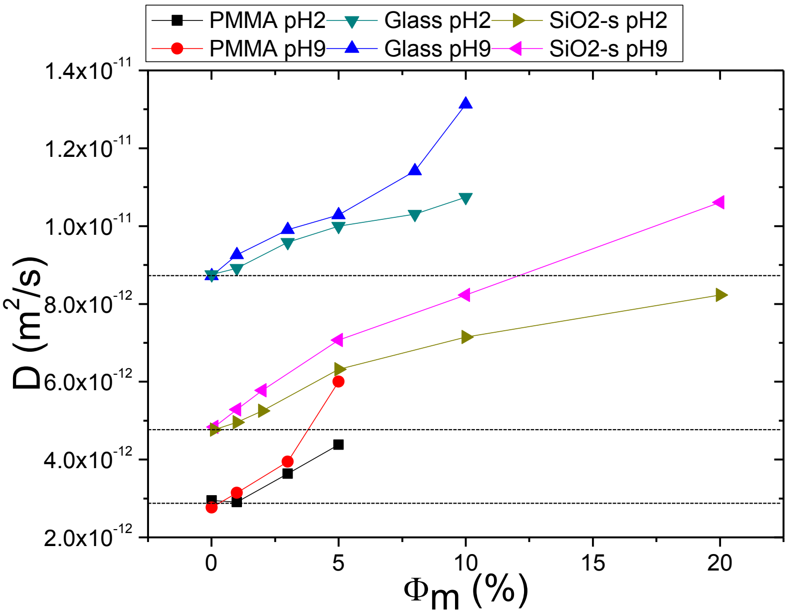

Figure 4.1: Diffusion coefficient as a function of the concentration of glass, PMMA and SiO2-s nanoparticles at two pH values. Dashed lines represent the nominal (self)diffusion coefficient calculated from the Stokes-Einstein relationship for each nanoparticle.

4.1.2 Effects due to particle-particle repulsion

The topographies of the stripe-like deposits formed on the glass substrates with weakly and strongly repulsive glass nanoparticles at 3% (w/w) are shown in Figure 4.2. Differences in the pattern morphology were observed when the particle-particle electrostatic interaction was varied. When the interparticle electrostatic repulsion was negligible (pH2), the stripe width was smaller than the pattern obtained with strong interparticle electrostatic repulsion (pH9). When the substrate receding contact angle was changed, by using PMMA substrates, the results of deposition of glass nanoparticles at pH2 and pH9 were noticeably different (see Figure 4.3). The PMMA-glass system (substrate-particle system) at pH2 revealed unresolved striped deposits although no particle deposit was formed at pH9. To study the plausible role of the particle wettability in the deposit morphology, we performed driven menisci experiments with the glass-PMMA and PMMA-PMMA systems at pH2 and pH9. We also found different morphologies of striped patterns with the glass-PMMA system when the pH was changed. The greatest deposits (width and height) were obtained with the PMMA-PMMA system at pH2 but no particle deposition was observed at pH9, as happened with the PMMA-glass system.

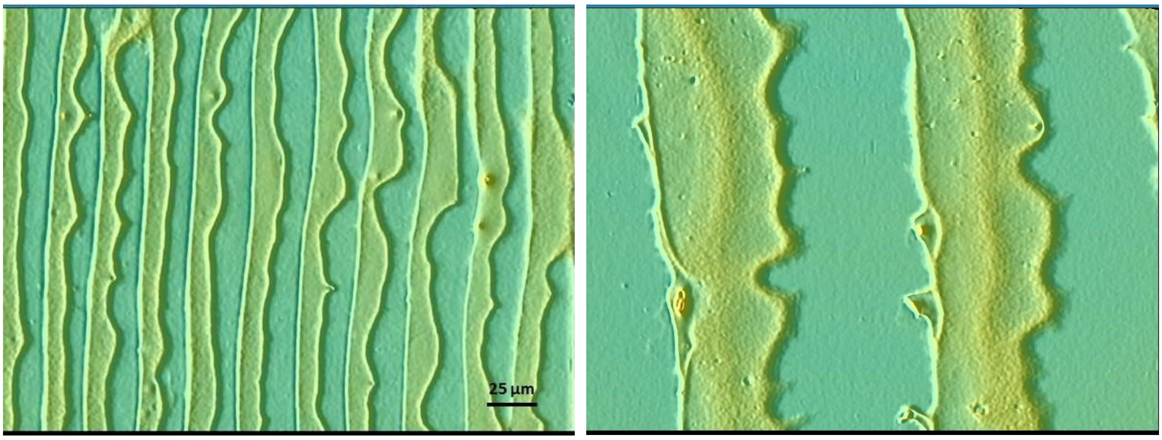

(a) pH2 (b) pH9

Figure 4.2: Stripe-like deposits of glass nanoparticles at pH2 and pH9 on glass substrates obtained with the driven menisci set-up. The concentration of nanoparticles was 3% (w/w).

We classified the different substrate-particle systems studied into symmetrical and asymmetrical systems. In Figure 4.4, we plot the deposit profiles for each type of system. The striped patterns formed with the glass-glass system and the large stripe obtained with the PMMA-PMMA system at pH2 were confirmed. The distance between stripes formed with the PMMA-PMMA system at pH2 was so large that just one stripe at once could be analyzed with the 20x objective. No deposition was found with the PMMA-PMMA system at pH9. At pH2, stripe-like deposits were also obtained with the asymmetrical systems although the glass-PMMA system revealed

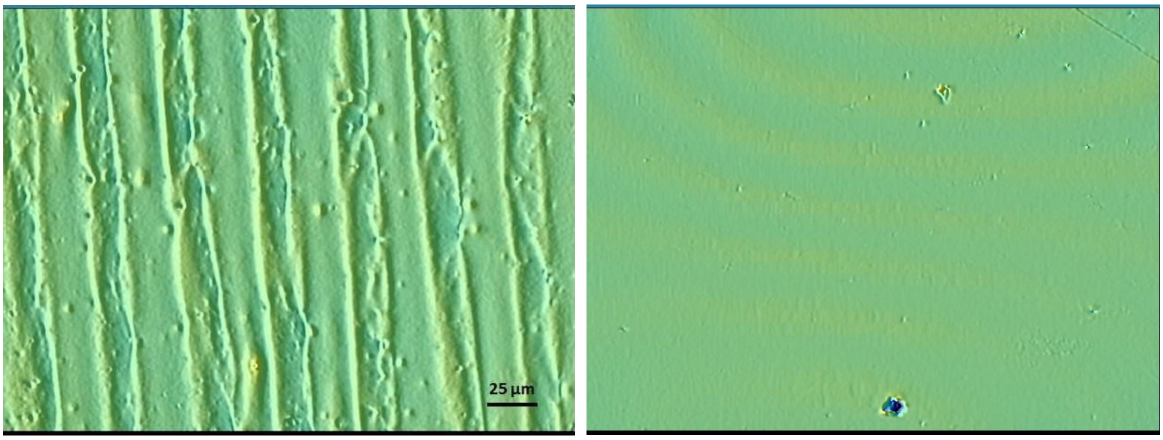

(a) pH2 (b) pH9

Figure 4.3: Deposits of glass nanoparticles at pH2 and pH9 on PMMA substrates obtained with driven menisci experiments. The concentration of nanoparticles was 3% (w/w).

larger deposits. Instead, at pH9, a striped pattern was obtained with the glass-PMMA system but no deposit was formed with the PMMA-glass system.

The main feature of the symmetrical systems is that the substrate-particle wettability contrast (differences between receding contact angles) is minimized. Otherwise, in the asymmetrical systems, the wettability contrast is negative for the glass-PMMA system and positive for the PMMA-glass system. However, there is no correlation between the substrate-particle wettability contrast and the final deposit. When the substrate used was PMMA at pH9, no deposits were formed regardless of the type of nanoparticle used. The glass and PMMA nanoparticles at pH9 may develop higher collective diffusion if a concentration gradient in the suspension is established. Further, these nanoparticles are subjected to a moderate convective flow due to the high receding contact angle of the substrate. As consequence, the nanoparticle deposition at driven receding contact lines was unfavored because the significant diffusive flow canceled or overcame the outwards convective flow. Unlike the case PMMA-glass at pH2, when the PMMA nanoparticles were used in the same conditions (PMMA-PMMA at pH2) the deposits were unexpectedly high and distant. Further work should be addressed to understand this result. To examine the effect of the diffusive flow when the convective flow is minimized, we performed menisci experiments with the glass-glass and PMMA-glass systems at pH2 and pH9. These experiments were carried out under vapor-saturated conditions, with no dry air flow and the cuvette closed (not sealed). This way the relative humidity inside the cuvette increased up to ≈94%. The AFM images obtained for the glass-glass system are shown in Figure 4.5. Particle deposits were only found at pH2. The residual convective flow on the (very hydrophilic) glass substrate was still significant compared with the collective diffusion of nanoparticles at pH2. In the PMMA-glass system, where the convective flow was much less noticeable than on the glass substrate, no deposit was found at both pH val-

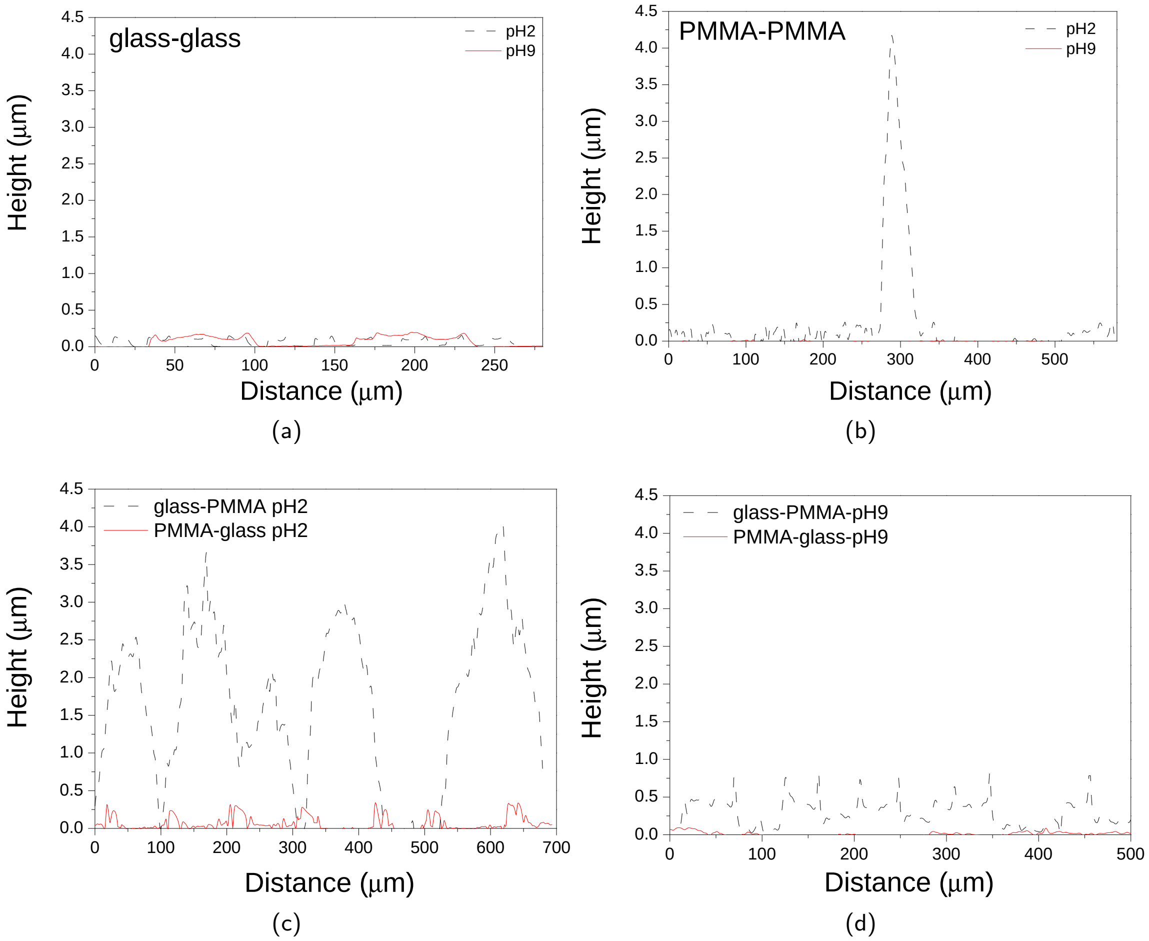

(a)

(b)

(c)

(d)

Figure 4.4: Deposit profiles formed with the symmetrical substrate-particle systems at pH2 and pH9: (a) Glass-glass system and (b) PMMA-PMMA system and the asymmetrical substrate-particle systems at (c) pH2 and (d) pH9. The concentration of nanoparticles was 3% (w/w).

ues. Since the convective flow at RH ≈94% was significantly reduced regardless of the substrate receding contact angle, the driving flow was completely suppressed by collective diffusion at pH9. The substrate charge at low ionic strength seems to be irrelevant in this scenario (*125*), where the intense flows developed close to the triple line are capable to drag charged particles even very close to the like-charged substrate. The role of the substrate seems to be more relevant through its receding contact angle by a two-fold effect: the size of wedge-shaped region near the contact line and the magnitude of the evaporation-driven convective flow.

Regarding the (primary) electroviscous effect (*126*) on the collective diffusion coefficient of stabilized colloidal suspensions, we are aware of the plausible impact of the particle charge on the water viscosity in the vicinity of the particle surface. The expected increase of the viscosity of a suspension containing interacting particles beyond the dilute limit (*126*) should indeed reveal their collective diffusive motion. To include the electroviscous effect in the calculation of the collective diffusion coefficient of interacting particles is certainly difficult. It is known that the electrolyte friction of a single spherical nanoparticle has a weak effect on the self-diffusion coefficient (*127*). The results obtained in this work with the strongly charged PMMA particles on two different substrates (PMMA and glass) and on the same substrate (glass) but at two different RH values (65% and 94-98%), point out that the primary electroviscous effect is negligible whereas the expected increase of the suspension viscosity (*126*) is properly derived from the collective diffusive motion of interacting particles beyond the dilute limit.

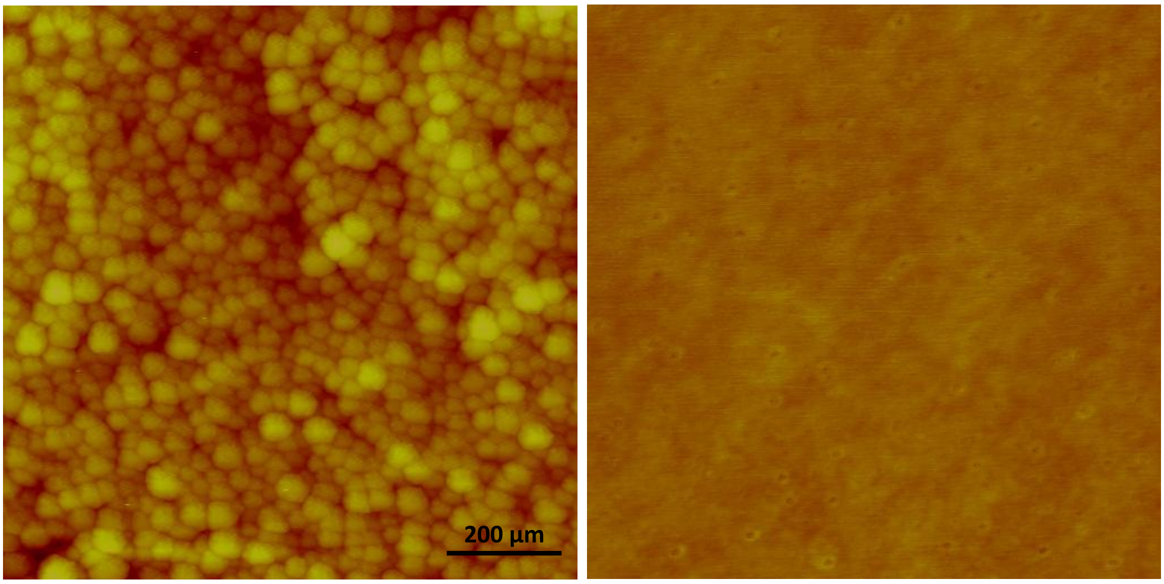

(a) pH2 (b) pH9

Figure 4.5: Atomic force microscopy images of the deposits obtained with driven menisci experiments under saturation conditions (RH ≈94%) for the glass-glass system at pH2 and pH9.

4.1.3 Effects due to nanoparticle concentration

To examine the effect produced by the nanoparticle concentration on the patterning, we conducted experiments on glass substrates with the SiO2-s nanoparticles at increasing concentrations (0.5-30% (w/w)), and at two pH values (pH2 and pH9). This way, the convective flow was fixed by the substrate receding contact angle.

It is clear the transition found in the pattern morphology as the particle concentration was changed, although with differences as the pH value used (see Figure 4.6). The deposit profiles are shown in Figure 4.7. The nearly uncharged nanoparticles formed patterns even at 0.5% (w/w), although unresolved. With these particles, the substrate was completely covered (see Figure 4.7b). Otherwise, when the nanoparticles were charged, almost no deposit was found at 0.5% (w/w) although a spiderweb-like deposit was found at 1% (w/w). However, well-defined striped patterns were formed with both particles from 5% (w/w). At higher concentrations (see Figure 4.8), the resulting striped patterns were more complex due to the plausible occurrence of Marangoni recirculating flows (see Figure 2.5 and the increase of viscosity (see Figure 2.7). The difference found at low particle concentrations might be explained in terms of competition between the outward convective and inward diffusive flows. Less charged particles were transported towards the contact line because they diffused towards the bulk more readily than the barely charged particles (see Figure 4.1).

The number of SiO2-s nanoparticles deposited on glass substrates for increasing concentrations is plotted in Figure 4.9. Significant differences are observed as the particle electric charge. The amount of material forming the deposits is noticeably greater with the barely charged nanoparticles (pH2) up to 5% (w/w). From this concentration, the number of SiO2-s nanoparticles deposited was independent of the pH value. Instead, the deposits formed with the charged nanoparticles grew steadily as the particle concentration up to 25% (w/w), where the deposit growth seems to saturate. The plausible decrease of the concentration gradient between the triple line and the suspension bulk as the bulk concentration increases might explain the disagreement found between the nearly uncharged and charged nanoparticles at low concentration. According to the Fick's law, a lower gradient mitigates the collective diffusion even for the charged nanoparticles.

High differences were observed on the number of particles deposited for different charged particle states. When particles were nearly uncharged, the coverage degree was higher, observing pattern even at 0.5% (w/w). On the other hand, when charged particles were used, almost no particles were deposited for the lowest concentration. A transition to patterned deposit can be observed, obtaining an intermediate state (spiderweb-like deposits) for 1% (w/w) and stripe-like deposits for 5% (w/w) and higher concentrations. This difference for low concentrations could be explained in terms of the competition between convective and diffusive flow. Since convective flow is constant for all the experiments (dependence only on the receding contact angle), the differences

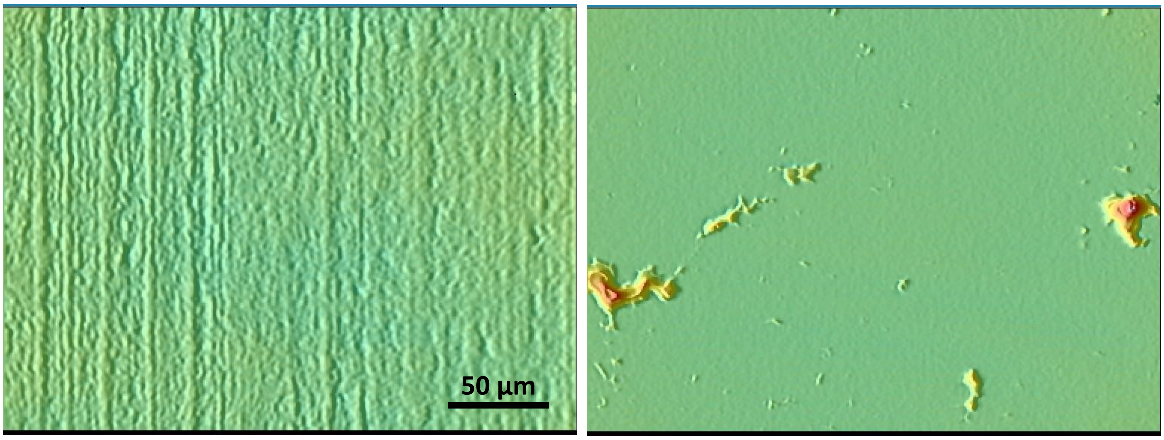

(a) 0.5% pH2 (b) 0.5% pH9

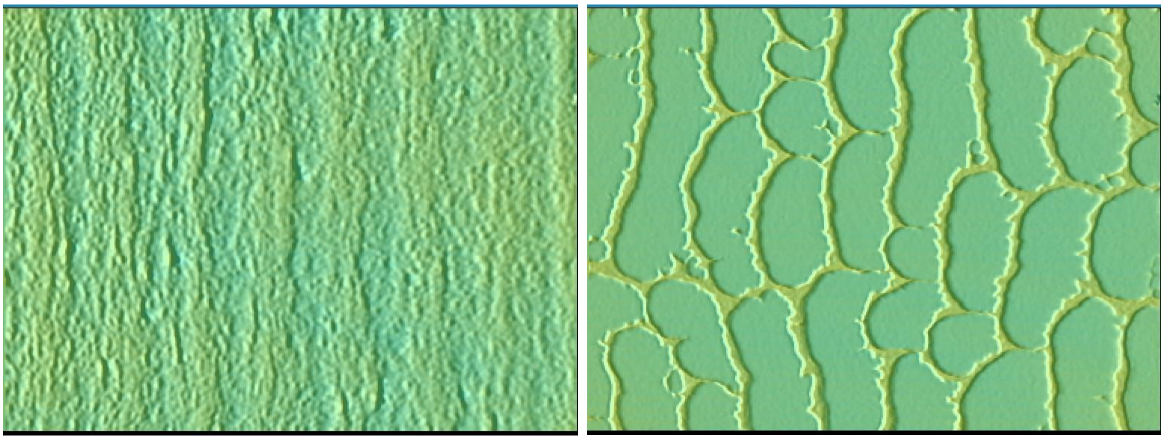

(c) 1% pH2 (d) 1% pH9

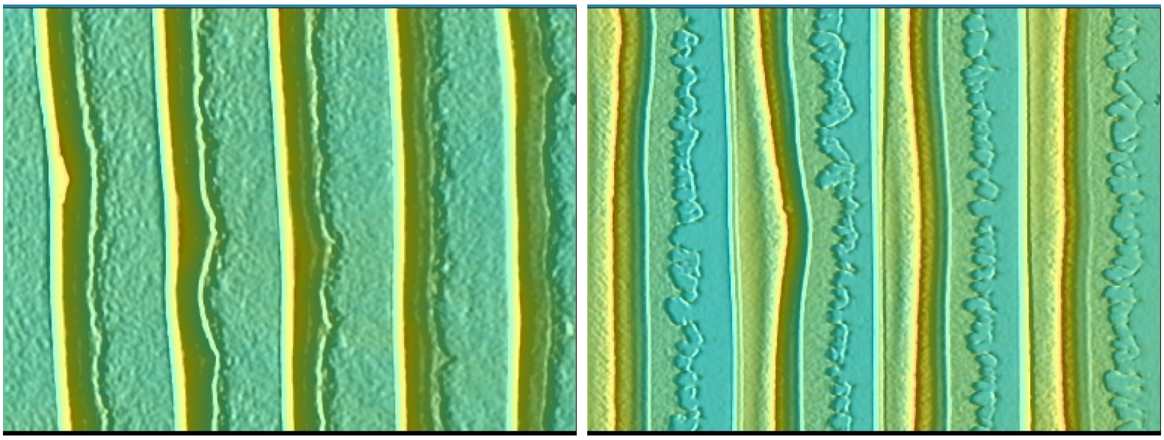

(e) 5% pH2 (f) 5% pH9

Figure 4.6: Deposits obtained of SiO2-s nanoparticles at pH2 and pH9 on glass substrates obtained with the driven menisci set-up. The concentration of nanoparticles was 0.5%, 1% and 5% (w/w).

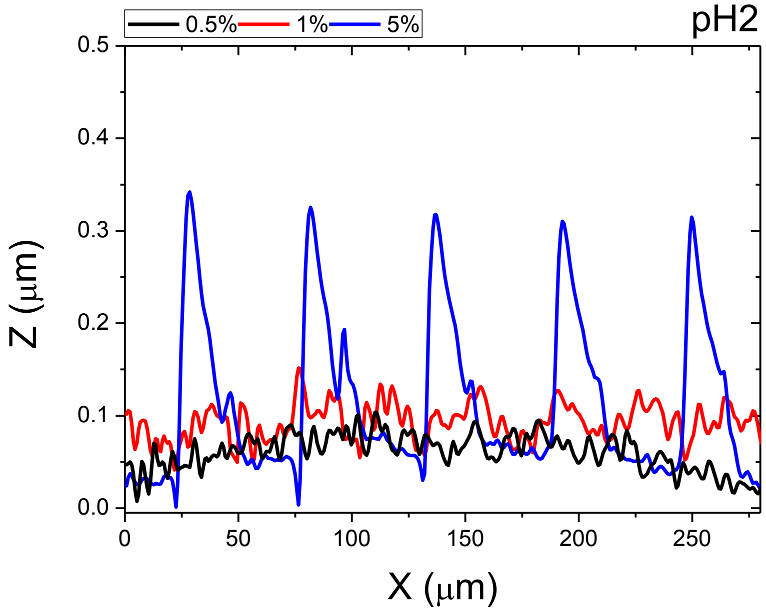

(a)

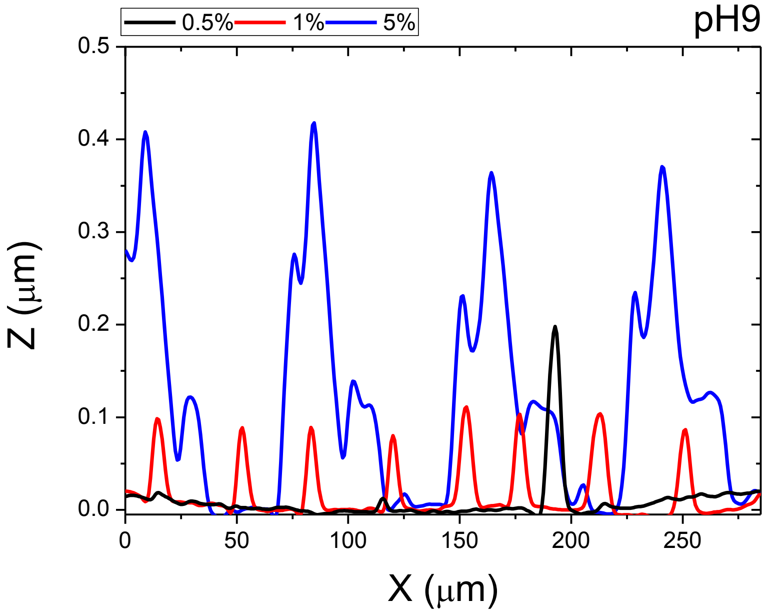

(b)

Figure 4.7: Deposit profiles formed at (a) pH2 and (b) pH9. The concentration of nanoparticles was 0.5%, 1% and 5% (w/w).

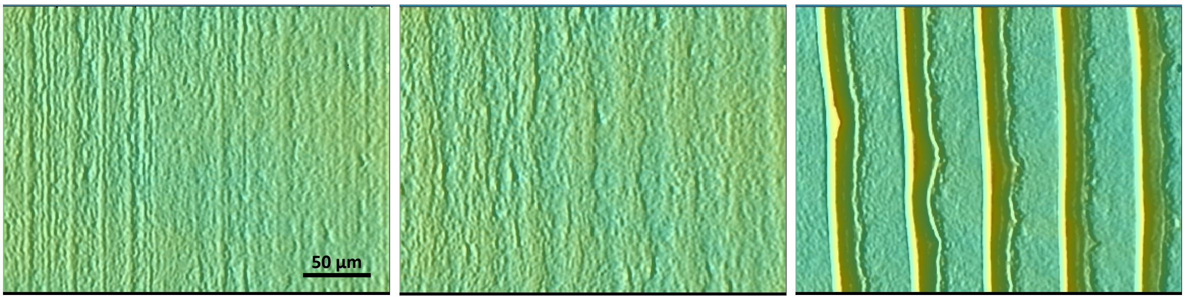

(a) 0.5% (b) 1% (c) 5%

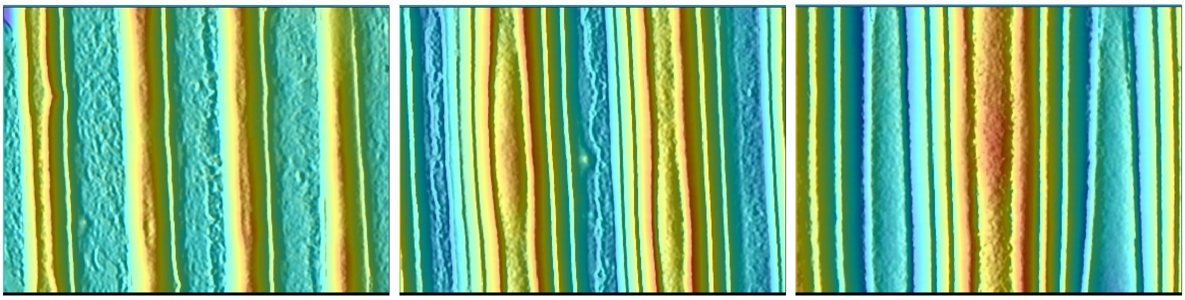

(d) 10% (e) 15% (f) 20%

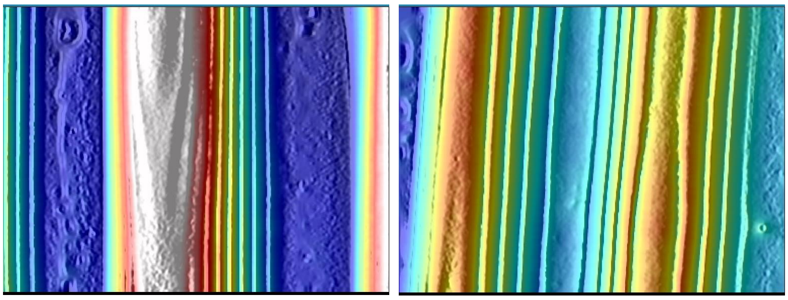

(g) 25% (h) 30%

Figure 4.8: Deposits of the SiO2-s nanoparticles on the Glass substrate at (a) pH2 for increasing concentrations.

observed in the patterns for a fixed concentration but two particle-particle electrical state (pH2-pH9) would be caused by the diffusive flux. At low concentrations when particle gradient between the contact line and the bulk becomes relevant, according to Fick's law, diffusive flow is enhanced. Thus less particles arrive to the contact line in the charged state compared with the uncharged one (diffusion coefficient is higher at pH9 than pH2, see Figure 4.1). On the other hand, as concentration rises, the particle gradient between the triple line and the bulk attenuates. This leads to a similar number of particles deposited (see Figure 4.9)

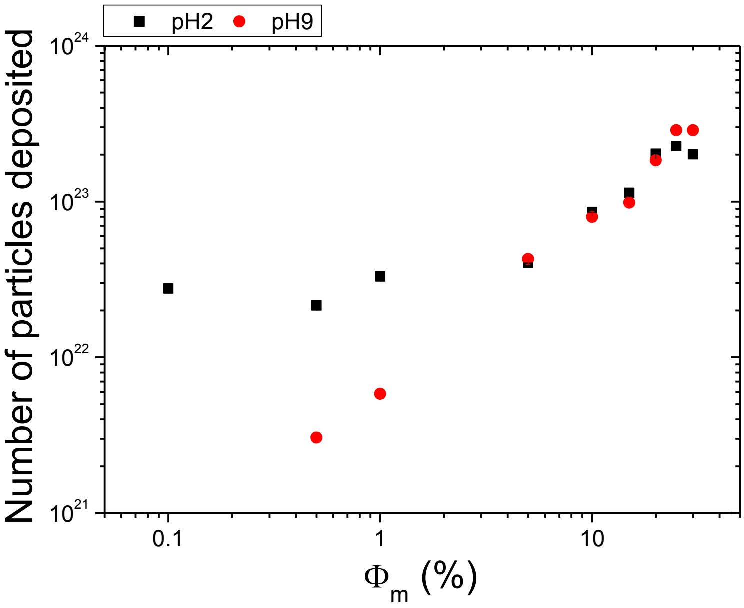

Figure 4.9: Calculations of the number of particles deposited after driven menisci experiments when particle concentration was increased (0.5-30% (w/w)) at pH2 and pH9.

4.2 Conclusions

Unlike typical experiments of free drop evaporation, evaporating menisci experiments with driven receding contact lines allow to explore convective assembly at fixed and low bulk concentration, which enables to develop high concentration gradients. Particle deposition at driven receding contact lines may be controlled by the interplay between evaporative convection and collective diffusion. When the evaporation flow is weak, deposition can be suppressed if the long-range interparticle repulsion becomes important and the diffusion overcomes the particle transport by convection before reaching the triple line. In this scenario, the receding contact angle of the substrate and the relative humidity dictate the strength of the convective velocity field. Diffusive flow takes relevance at low particle concentration, when the gradient between the contact line and bulk is important. In this case, the particle-particle repulsion produces a significant transition in the final pattern morphology and reduces the number of particles deposited.

Part II

Free Evaporating Drops

CHAPTER 5

Materials and methods

5.1 Substrates

We used glass microscope cover slips (see Section 2.1) and polymethyl-metacrylate sheets (PMMA, 0.05mm-thick, Goodfellow) as substrates. These substrates were selected because of their transparency, smoothness and small thickness. The glass cover slips were conveniently cut with a diamond tip. On the other hand, due to the bending of the thin PMMA sheets, we designed a titanium holder (64x26mm^2) with a circular hole of 1cm diameter at its center. This way, the PMMA substrate was not deformed with the immersion objective of the confocal microscope used (see Section 5.3). Before each experiment, the substrates were treated as described in Section 2.1. The values of contact angle hysteresis are collected in Table 2.1.

The root-mean-square roughness with the withe light confocal microscope (see Section 2.3) over 210 x 285 μm^2 was 6.5 nm for the glass substrates and 24.4 nm for the PMMA substrates.

5.2 Particle suspensions

We purchased from Microparticles six aqueous suspensions of spherical particles with different size, density and electric charge response. The main features of these particles are listed in Table 5.1. We used fluorescent-labeled particles of polystyrene (PS), melamine-formaldehyde (MF) and carboxylated-MF (MF-COOH). We also selected non-fluorescent silica (SiO2-l) particles by their density value. The PS particles are constantly charged because their strong acidic sulfate groups are fully dissociated in all relevant solution conditions. The rest of particles have a pH-dependent surface charge due to their different ionizable terminal groups. The particle electric charge was controlled in all experiments. The particles were accordingly diluted in buffer solutions of low ionic strength ($\leq$15mM). We used a Zetasizer Nano device (Malvern, 4mW He-Ne laser, 633nm wavelength) to measure the electrophoretic mobility of the particles (see Figure 5.1). We also measured with the pendant drop method (house-in device) the surface tension of the particle suspensions as received (see Table 5.1) to explore the presence of surface-active traces from the corresponding synthesis.

The experiments of evaporating drops were carried out at very low particle concentration to avoid saturation of the signal detected by the confocal microscope (see Section 5.3). The optimal concentrations were found between 0.002% and 0.01% (w/w). Binary mixtures (1:1 in weight) were also prepared to illustrate in-situ the deposition of particles with different size or charge-mass ratio in the "wedge" region during the drop evaporation. This way, we used the same particle suspension (MF-l, MF-s) to explore the substrate wettability. On the other hand, we studied different type of particle and binary mixtures on a fixed substrate (Glass).

Acronym	**Particle**	**Density** (g/cm^3)	ϕ_{max} (%w/w)	**Diameter** (μm)	γ_{LV}(mN/m)
MF-s	Melamine-Formaldehyde	1.51	2.5	0.366$\pm$0.06	66$\pm$2
MF-l	Melamine-Formaldehyde	1.51	2.5	1.11$\pm$0.05	70$\pm$1
PS-s	Polystyrene	1.05	2.5	0.285$\pm$0.06	70.2$\pm$0.3
PS-l	Polystyrene	1.05	2.5	1.08$\pm$0.04	70.2$\pm$0.3
MF-COOH	Carboxylated-MF	1.51	2.5	1.09$\pm$0.07	68$\pm$1
SiO2-l	Silica	1.8-2	5	1.16$\pm$0.05	68$\pm$1

Tabla 5.1: Particles used in this part.

Particle	**Fluorochrome**	λ_{abs} (nm)	λ_{em} (nm)
MF-s	Rhodamine B	560	584
MF-l	Fluorescein Isothiocyanate	506	529
PS-s	FluoGreen	502	518
PS-l	FluoRed	530	607
MF-COOH	Rhodamine B	560	584

Tabla 5.2: Absorbance and emission wavelength for the fluorescent particles used in this part.

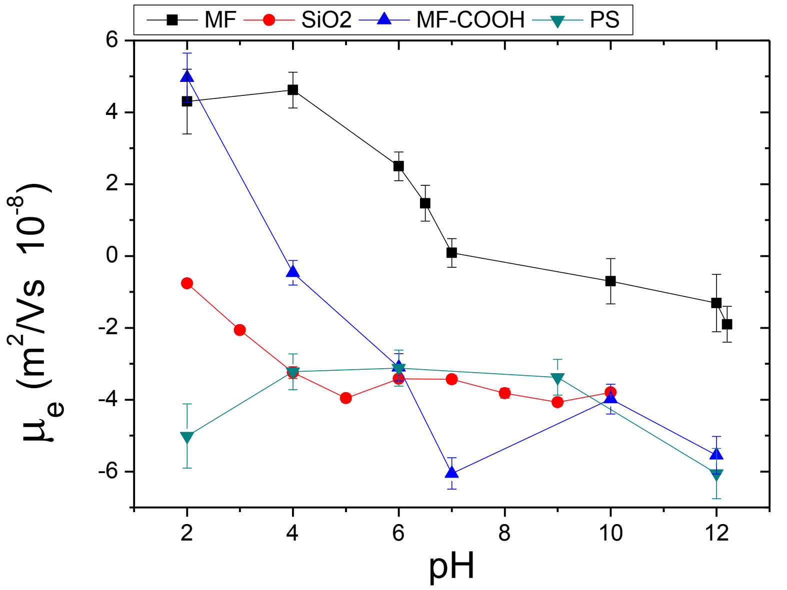

Figure 5.1: Electrophoretic mobilities for the particles used in free evaporating drops. All measurements were performed with low ionic strength buffers at 0.01% (w/w).

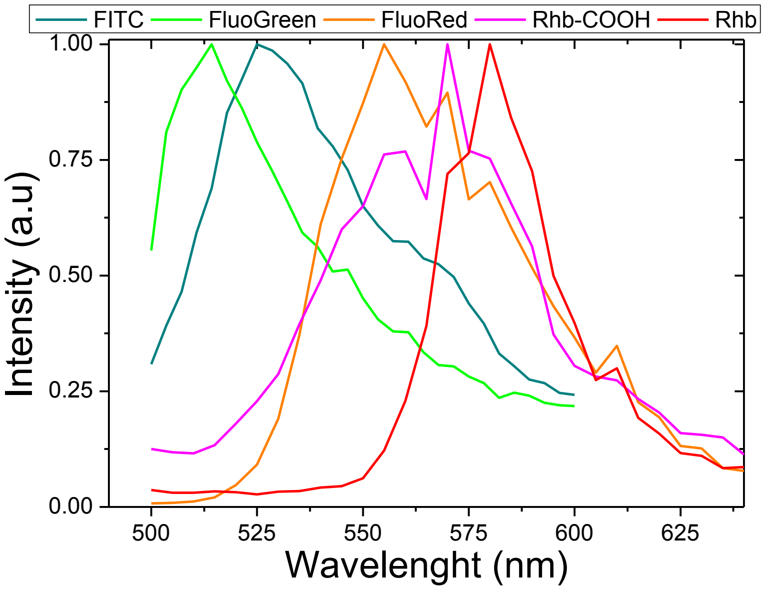

Figure 5.2: Emission spectra for the different fluorochromes of the particles used in this part.

In Table 5.2 we present the wavelength values for absorption and emission of the fluorescent particles. Nonetheless, to optimize the detection of particles with different fluorochromes, we measured their emission intensity with the device described in Section 5.3 over a wavelength range of several nanometers (see Figure 5.2). Intensity values lower than 500 nm were not measured to avoid interference with the lasers as they emitted at 488 and 496 nm. The spectra show different maxima although the red/orange fluorochromes (Rhb and FluoRed) and the green fluorochromes (FITC and FluoGreen) were close. A slight overlap was also observed between FITC and FluoRed. However, we could perform experiments with binary mixtures of particles with these fluochromes by selecting a narrow-wavelength detection window.

5.3 Experimental set-up

We used Confocal Laser Scanning Microscopy (CLSM) with an inverted microscope (DMI6000, Leica) as described in Figure 5.3. The experiment were conducted at the Scientific Instrumentation Center (CIC, Centro de Instrumentación Científica) of the University of Granada. The CLSM device has different lasers (Blue diode of 405 nm, Argon laser [458, 476, 488, 496 and 514 nm] and He/Ne lasers of 543, 594 and 633 nm). We selected the light source depending on the absorbance of the fluorochrome adsorbed to each particle (see Table 5.2). The drop volume was 3μl and the experiments were carried out at ≈22-25°C and a Relative Humidity (RH)≈38-42% (still air). The images obtained (512x512 pixel) were captured each 1.3s and next, analyzed with the public software ImageJ. We reduced our analysis to pinned triple lines over a window of 77.5x77.5μm^2 (100X objective) and occasionally 156x156μm^2 (40X objective). We focused on the top of the substrate. The z-depths of field were 0.7 μm and 1.8μm with the 100X and 40X objectives, respectively. These values allowed to observe mainly the particles deposited just on the substrate near the contact line although, in some cases, it was also possible to observe unfocused particles adsorbed at the water-air interface, close to the substrate (see Appendix E). This way, we mainly monitored the in-plane motion of incoming particles at the contact line (see Figure 5.4).

The fluorescent particles were counted by labeling (*128*) in each frame. We selected a suitable threshold of the corresponding image channel (red or green, accordingly) to individualize the particles (see Figure 5.5) and remove to those unfocused ones (not in-plane). The non-fluorescent SiO2-I particles were analyzed from bright field images also by labeling. However, when the non-fluorescent particles were used in bidisperse mixtures, we counted all particles, next the fluorescent particles by colour segmentation and then both numbers were subtracted to obtain the number of non-fluorescent particles arriving at the contact line. Nanoparticles (MF-s and PS-s) were counted from the number of red or green pixels per frame divided by the pixels occupied by a single particle. We evaluated the particle increment in the region of interest from the beginning of the image

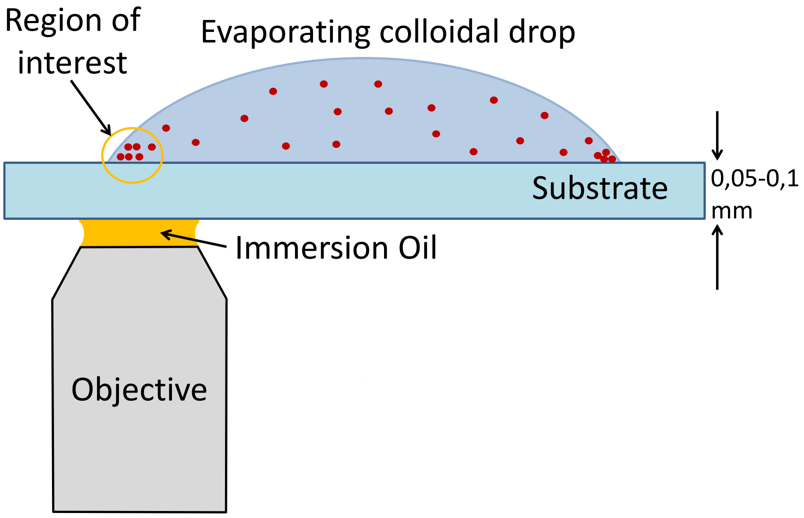

Figure 5.3: Set-up used to count the particles arriving at the triple line. The region of interest is reduced to the triple line and its immediate vicinity, considering a square window of 77.5 or 156 μm side as the magnification used.

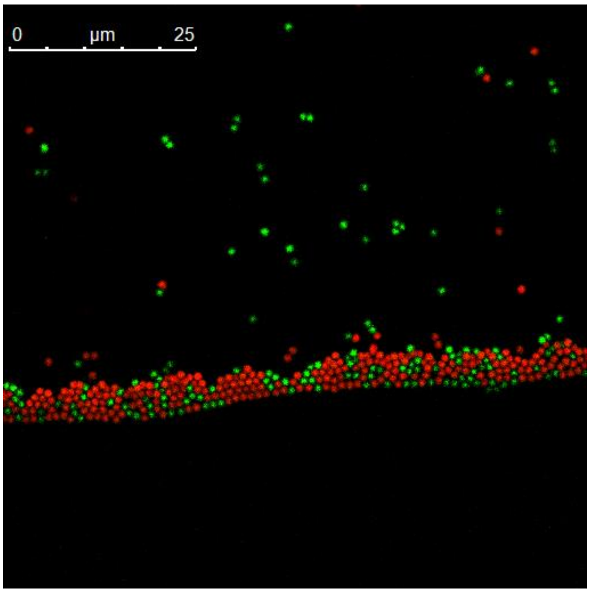

Figure 5.4: CLSM image of a mixture of MF-I and MF-COOH particles arriving at the triple line. Two colors can be observed and individual labeling can be performed.

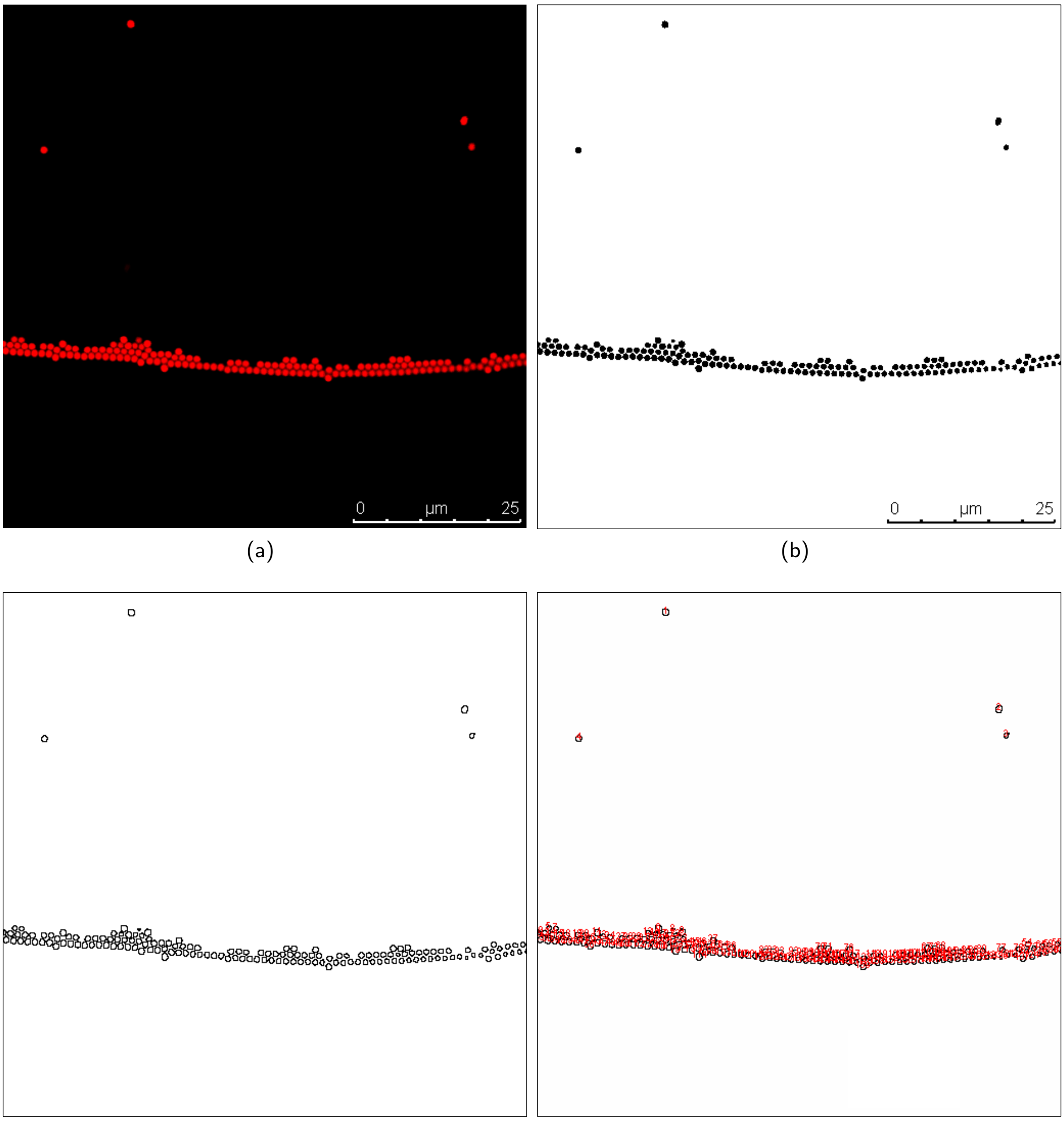

(a) (b)

(c) (d)

Figure 5.5: Process of particle counting by labeling. For each frame (a) we apply a threshold (b) then the particle contours are obtained (c) and the particles are numbered (d) and counted.

acquisition, once the triple line was localized, the magnitude of excitation signal was adjusted and the moving particles were focused. Due to this, the zero time in our experiments does not strictly correspond to the onset of drop evaporation. However, the time delay was always lower than 1 min. We selected the region of interest including the contact line (see Figure 5.4), The particle increment was divided by the drop area visualized in each experiment. In the experiments where the contact line receded, the particle counting was interrupted because the wet area varied. When we compared two particles with different density, the number of each particle in the bulk was also different at the same solid concentration. This way, to normalize by the total number of each particle, we divided the particle increment per unit of wet area nearby the contact line ($\Delta N/A$) by the particle number in a 3μl drop (N_0).

Unfortunately, we could not perform particle tracking. We could not track a single moving particle in 2-D dimensions in real time. In order to continuously track a particle, its position must be determined on-the-fly, and this is possible if the spatial and temporal resolutions are adequate. Our maximum temporal resolution was 1.3 s per frame instead of the typical values of milliseconds per frame. In Figure 5.6 we describe the stages reproduced in a typical plot of increment

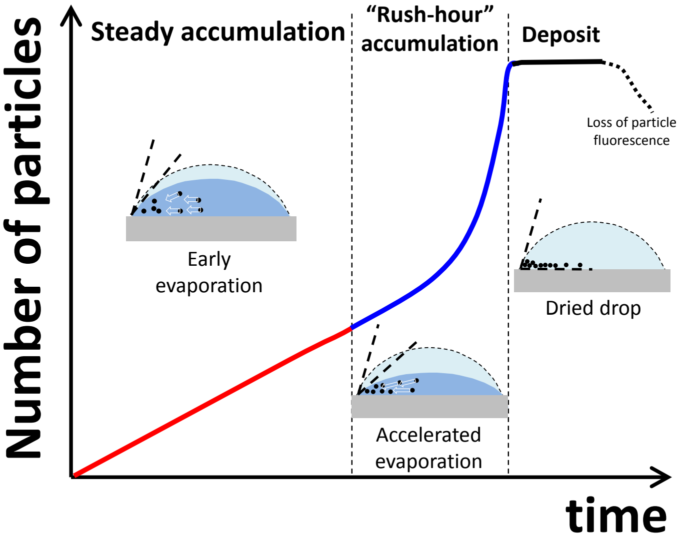

Figure 5.6: Typical behavior of the particle increment per unit area in terms of time. Three stages with different slope can be identified: steady accumulation, "rush-hour" accumulation and deposit formation.

of particles per wet area in terms of time. There are three recognizable stages with different slope (flow rate). During the early evaporation, with small variations of volume and contact angle, the particles are steadily accumulated at the pinned triple line. The zero time for each plot corresponds to the beginning of the image acquisition after the drop deposition and plane focusing. The time delay was lower than 1 min. When the evaporation accelerates, the contact angle significantly decreases and the convective flow increases. We identify this "rush-hour" effect in the deposition rate (*76*) with the drop collapse (see Appendix D). The "rush-hour" stage can be more or less pronounced according to the experimental conditions and the system characteristics. Finally, once the number of particles accumulated saturates because no more particles are arriving to the fixed triple line, the region of drop analyzed is dried. During this final stage, the particle counting (fluorescence signal) can fluctuate or even decrease due to the dehydration of the particles and proximity between them leading to resolution artifacts. Depending on the contact line dynamics, firstly ruled by the receding contact angle of substrate and the occurrence of self-pinning (*1*), the overall time of the experiments was different. We measured the particle flow per unit of wet area during the early evaporation with a reproducibility level of 25-40%. The final amount of material deposited (particles/μm^2) was roughly estimated.

To validate this technique and ensure that we count the particles deposited on the substrate, we analyzed the colloidal deposition of PS-I particles at 0.01% (w/w). This particles are more likely to be adsorbed at the water-air interface (see Appendix E). We monitored the particle increment nearby the contact line at both fluorescent and bright-field channels (see Figure 5.7). We observed that the number of particles at both channels did not agree. Analyzing the fluorescence channel, there were some particles that were slightly out of focus (weak fluorescence). On the other hand, at the bright-field channel, some particles at the background (water-air interface) were completely out of focus (not visible) at the fluorescent channel.

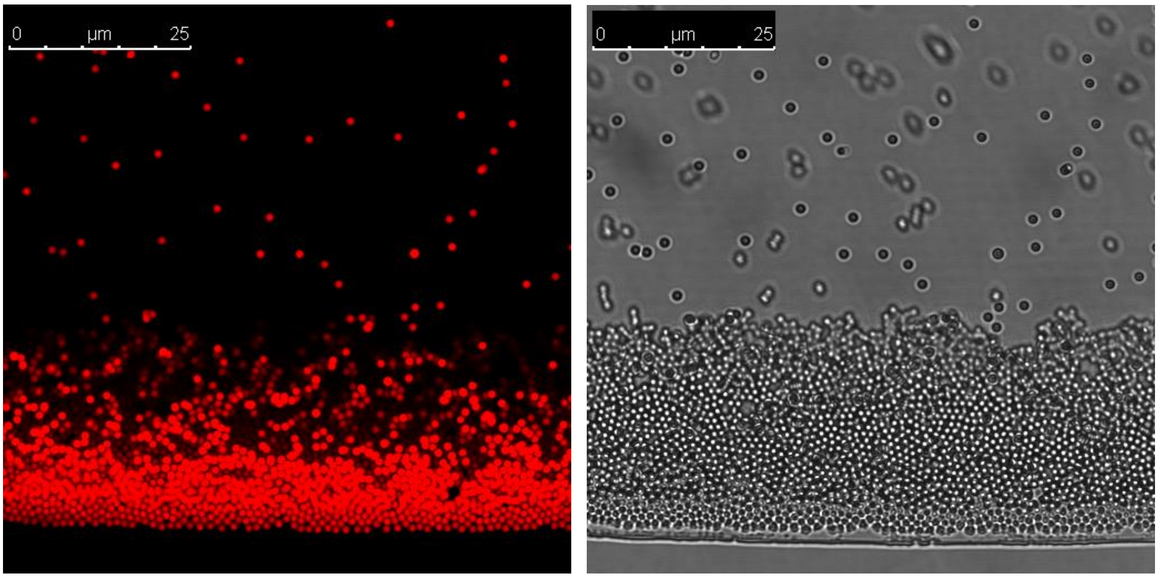

(a) (b)

Figure 5.7: CLSM images of colloidal deposition of the PS-I particles at pH6 and 0.01% (w/w) for fluorescent channel (a), and bright field channel (b). For the fluorescence channel only particles on top of the substrate are on focus. Particles in the background (water-air) interface are visible just in the bright field channel.

Figure 5.8 shows the particle increment per unit of wet drop against the time at the triple line for both channels. The rate of particle incoming at the contact line was greater in the bright-field images because the particles far from the substrate were also counted. On the other hand, the particle increment in the fluorescence images has the typical behaviour (see Figure 5.6). At the final stage of the experiment (complete drop evaporation), both increments agree because the particles at the water-air interface "fell" on the substrate due to the drop collapse. This way, we assure that the CLSM technique for fluorescent particles is a good method to monitor in-plane colloidal assembly by convective deposition.

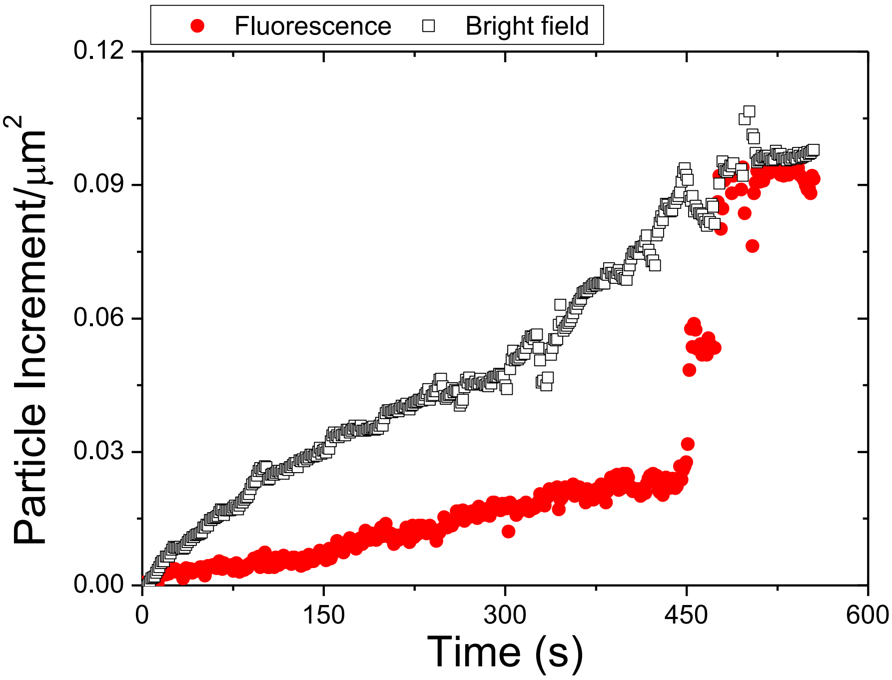

Figure 5.8: Particle increment per wet area in term of time for the PS-I particles at 0.01% (w/w) at pH6 analyzed in bright field and fluorescence channel. The particle increment overlap in the final stage (drop collapse) when particles at the water-air interface deposit on the substrate.

CHAPTER 6

Effect of the wettability properties of the substrates

Wettability properties can alter the colloidal self-assembly by convective deposition (*39*). The final deposit of free evaporating drops can reveal the receding contact angle and contact angle hysteresis of the substrates used (*67*). In this chapter, we analyzed the deposits of the SiO2-l particles (see Section 5.2) formed with evaporating sessile drops, on the substrates described in Section 5.1. To illustrate the effect, we gently placed 13 μl drops of SiO2-s suspensions at 0.01% (w/w) on the substrates to study. The drops evaporated freely into a closed chamber (not sealed) where a constant flux of dry air (RH$\approx$2%) was insufflated. Figure 6.1 shows the cenital image of the deposits. It is clear that the wettability properties alter the final morphology of the stains. However, in-situ measurements of the particle accumulation provide further information about the effects of the wettability properties of the substrates on colloidal self-assembly by capillary-driven deposition.

In this chapter, we monitored the accumulation of particles arriving at the contact line of evaporating sessile drops by CLSM. From particle counting, we evaluated the particle increment per unit of drop area over the time. We used four substrates with different contact angle hysteresis and receding contact angle (see Table 2.1). We used particles with different diameter to illustrate

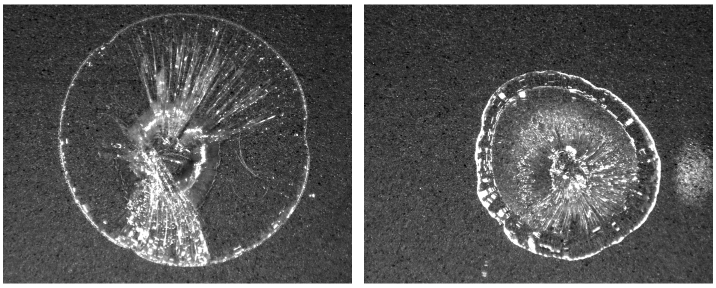

(a) PTGlass (b) Glass

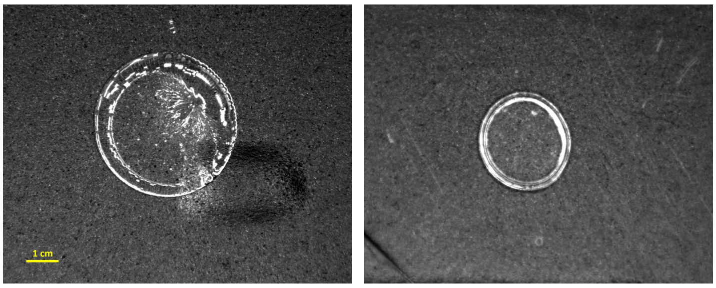

(c) HTGlass (d) PTGlass

Figure 6.1: Cenital images of 13μl drops of the SiO2-l particles at 0.01% (w/w) on the substrates used in this chapter. Different morphology is observed as the substrate used.

the importance of the “wedge”-shaped region nearby the contact line (see Section 1.2.2).

6.1 Results and discussion

We confirmed the receding contact angle of our substrates by using binary suspensions of PS particles with different size (3:1 in particle number). The experiments were conducted under the same evaporation conditions. The size segregation, observed in Figure 6.2, due to the so-called “wedge effect” correlates to the receding contact angle of each substrate. On the PMMA substrate, there is no significant segregation (see Figure 6.2a). On the HTGlass substrate, the separation between the smaller particles (PS-s) and larger ones (PS-l) is noticeable (see Figure 6.2b). On the Glass substrate, the segregation is very clear (see Figure 6.2c). Finally, on the PTGlass substrate a change of magnification was necessary to show the two types of particle deposited on the substrate (see Figure 6.2d). Evaporation experiments on the PTGlass substrate were hard to accomplish because the drop completely spread on the substrate and dried in few seconds.

Figure 6.3 shows the number increment of incoming particles per unit of wet area on different substrates. In each graph, the experiments were conducted at the same evaporation conditions. We can mostly identify three different stages according to the horizontal flow rate (see Figure

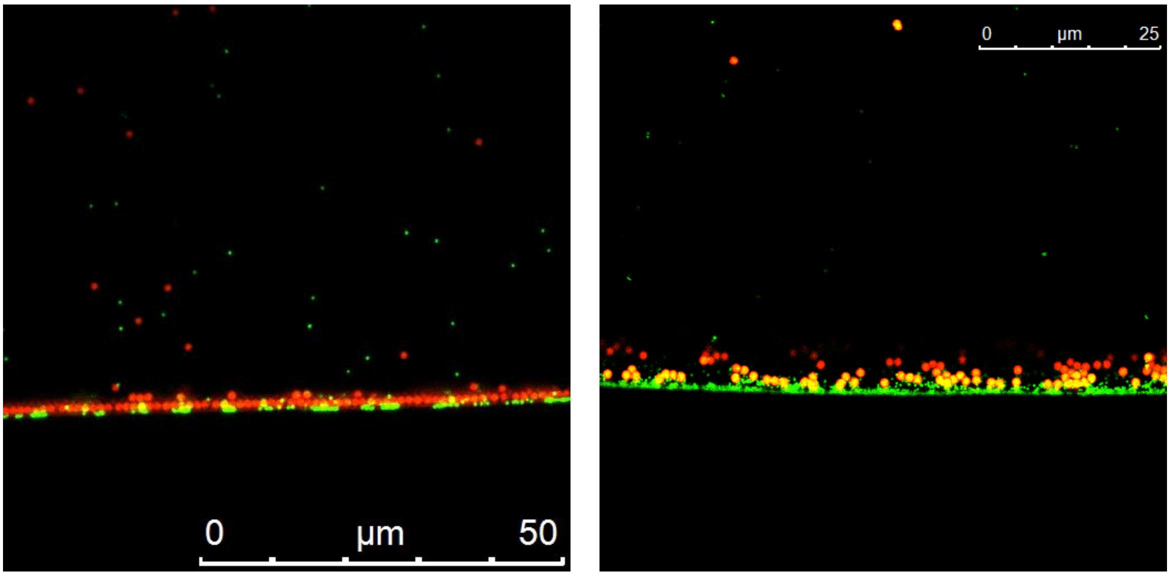

(a) PMMA

(b) HTGlass

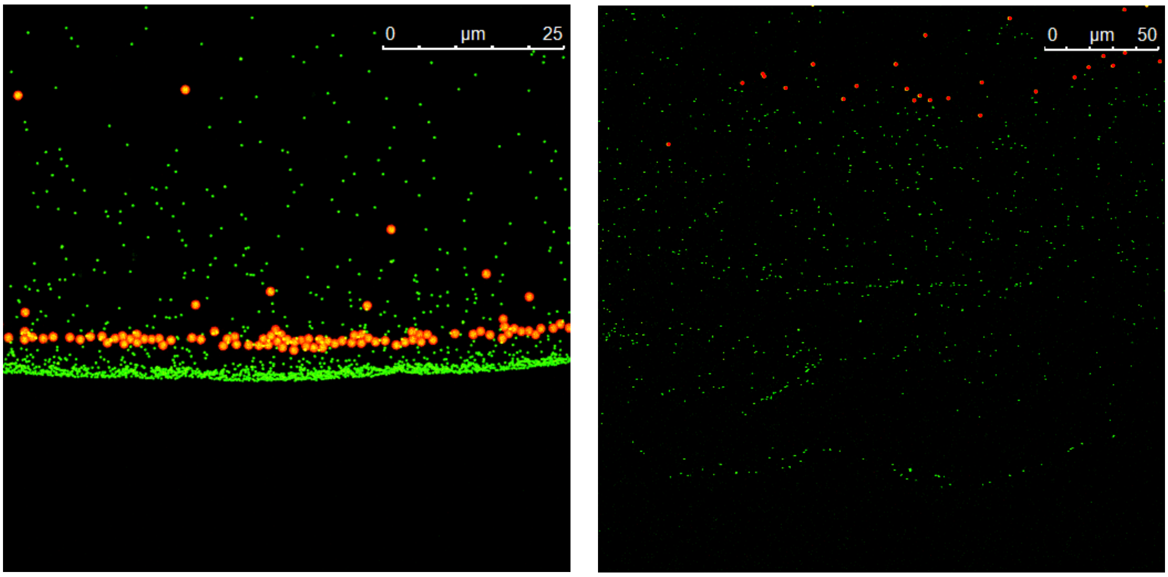

(c) GLass

(d) PTGlass

Figure 6.2: CLSM images of the contact lines of sessile drops containing a 3:1 mixture of PS-s and PS-l particles on the different substrates. The observed size segregation at the triple line agrees with the receding contact angle of each substrate.

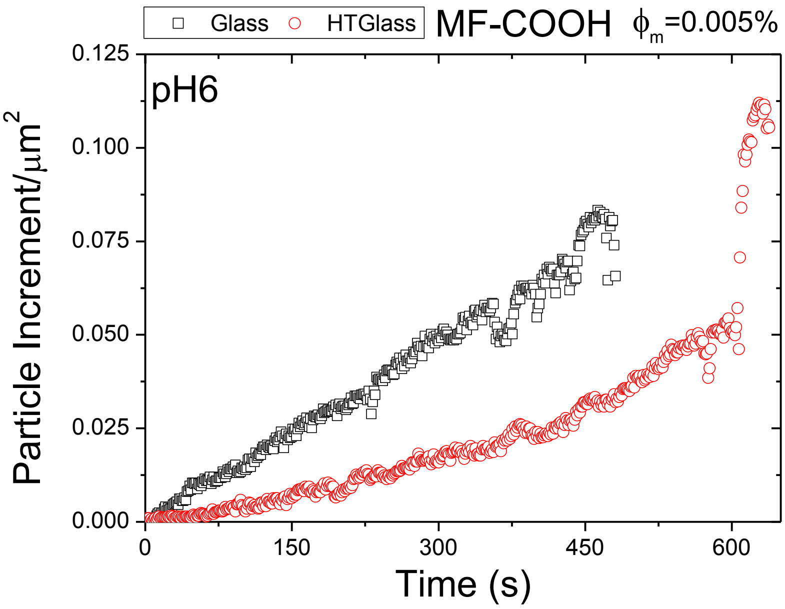

(a)

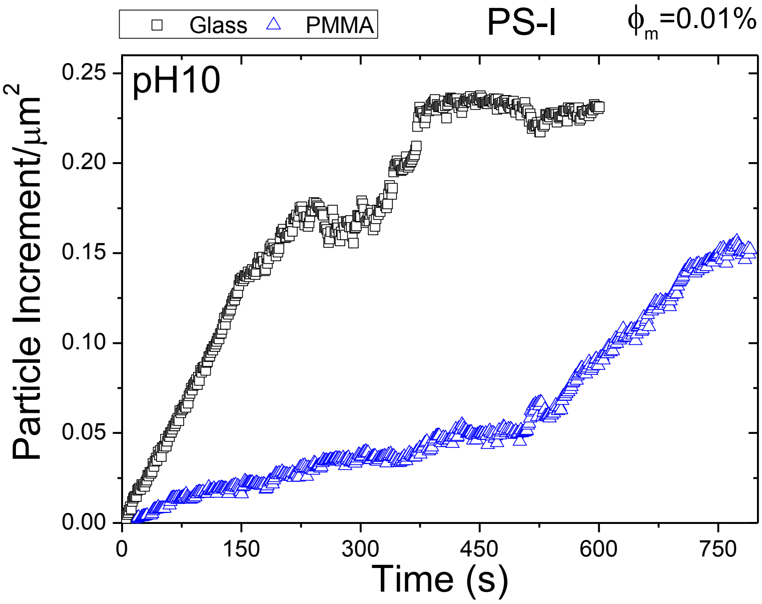

(b)

Figure 6.3: Number increment of particles per unit of wet area in terms of time on different substrates. (a) Negatively charged MF-COOH particles (pH6) at 0.005% (w/w) on the Glass and HTGlass substrates. (b) Negatively charged PS-I particles (pH10) at 0.01% (w/w) on the Glass and PMMA substrates.

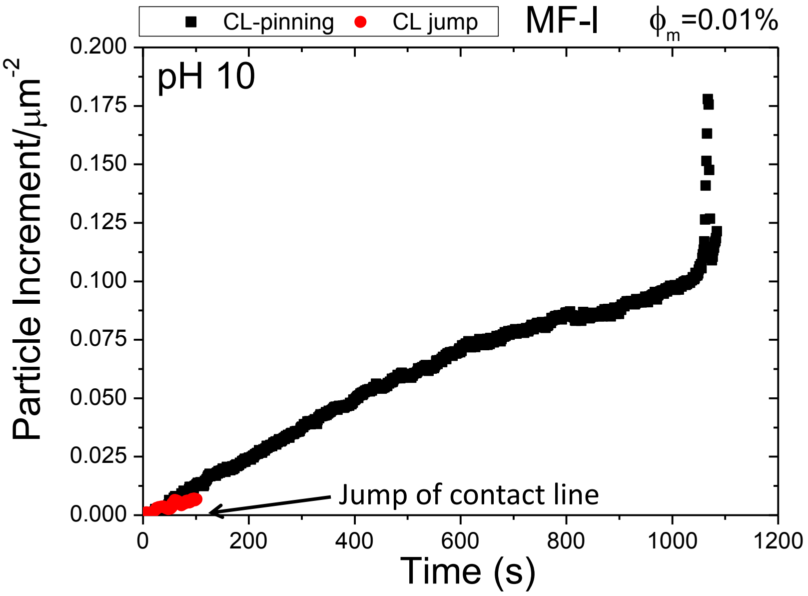

(a)

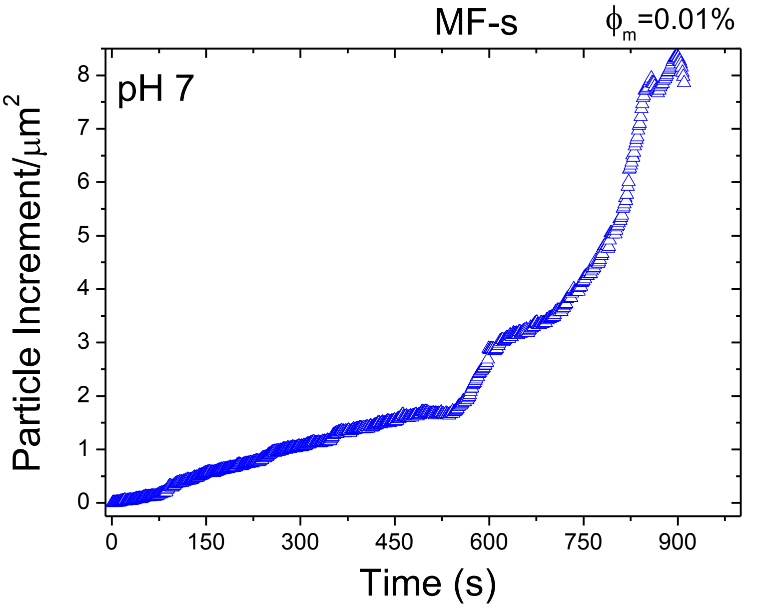

(b)

Figure 6.4: Number increment of particles arriving at the contact line per unit of wet area on the PMMA substrate for (a) the negatively charged MF-l particles (pH10) at 0.01% (w/w) and (b) the barely charged MF-s particles (pH7) at 0.01% (w/w).

5.6).We performed linear fits to the data corresponding to the "steady" stage and next compared the slopes for each substrate-particle system. We found that the deposition rate of the negatively charged MF-COOH particles at the contact line was 2.8 times faster on the Glass substrate than on the HTGlass substrate (see Figure 6.3a) and with the negative charged PS-I particles, 7 times faster on Glass than on PMMA (see Figure 6.3b). The different accumulation rate on each substrate was observed regardless of the particle concentration, charge and density. This is due to the lower evaporation rate on the HTGlass and PMMA substrates because of their higher receding contact angles. Although the drop evaporation took longer on the HTGlass and PMMA substrates, the triple line did not recede because the contact angle hysteresis enhanced the self-pinning (*39*) of the contact line by increasing its natural pinning time. However, due to the high value of contact angle hysteresis of the PMMA substrates, in some experiments, the self-pinning was not eventually assured and the triple line receded (see Figure 6.4a). The barely charged MF-s particles at 0.01% (w/w) perpetuated the self-pinning (see Figure 6.4b) because much more particles were available in the bulk to be transported by the convective flow.

From the above-described results found for different pH values and on different substrates, the substrate electric charge seems to play a minor role in the particle deposition. The substrate mainly affects the particle accumulation close to the contact line by setting the wedge-shaped region, pinning time of contact line and evaporation-driven capillary flow.

6.2 Conclusions

We performed in-situ particle counting in the vicinity of the contact line with the CLSM technique. Beyond the size segregation produced by the so-called "wedge" effect, we confirmed that the wettability properties of substrates are very relevant for colloidal assembly driven by evaporative convection. The particle deposition rate strongly depends on the receding contact angle of the substrate. The substrate does modulate the particle increment close to the contact line through the evaporation-driven capillary flow due to receding contact angle. In particle deposition, the substrate wettability properties can alter the accumulation nearby the contact line both are correlated: On one side, the particle increment at the triple line depends, among other factors, on the time of natural pinning, the space available at the wedge-shaped region and specially, the convective flow. On the other hand, self-pinning due to particle deposition affects to contact line dynamics.

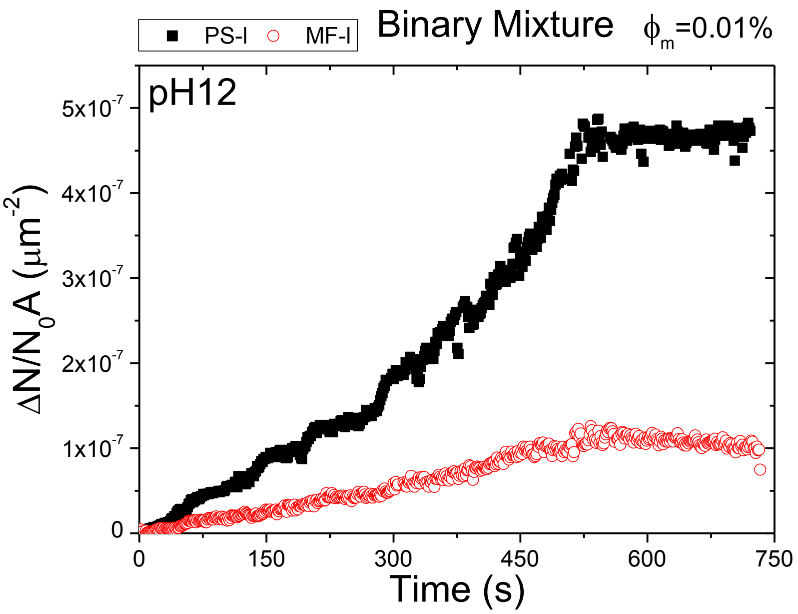

(a)

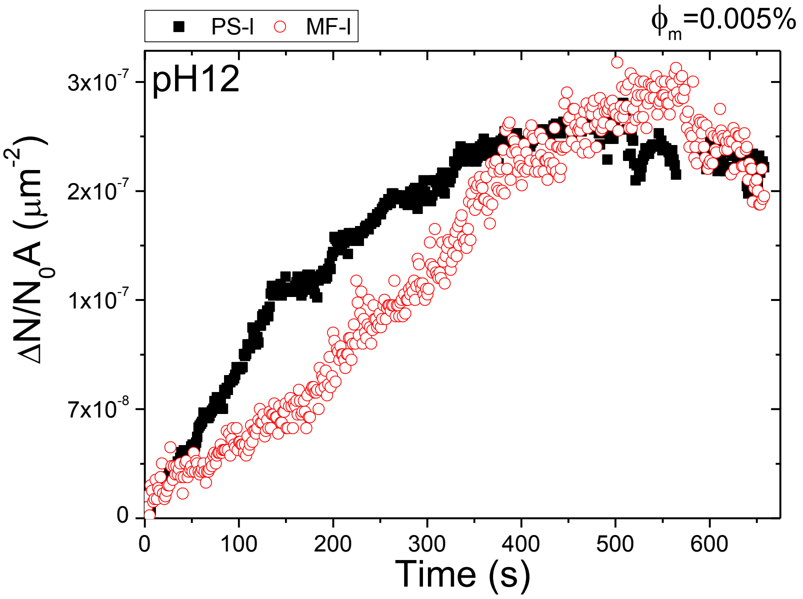

(b)

Figure 6.5: Normalized particle accumulation per area in terms of time for the PS-I and MF-I particles on Glass in: (a) a 1:1 binary mixture at pH12 and 0.01% (w/w) and (b) the corresponding monodisperse suspensions at pH12 and 0.005% (w/w).

CHAPTER 7

Effect of particle collective diffusion

The aim of this chapter is to examine the role of the particle electric charge in convection-driven self-assembly. We also performed in-plane counting of fluorescent particles in the vicinity of the triple line of evaporating drops by using CLSM. For the same evaporation conditions , fluorescent-labeled particles with different charge-response (see Section 5.3) over the pH scale were studied. Size, concentration and electric charge of the particles were conveniently selected accordingly (see Section 5.2). The use of two substrates with different receding contact angle allowed to explore different evaporation convective flows (see Section 5.1).

7.1 Results and discussion

gradients is not discarded. In the experiments carried out on glass substrates under the same evaporation conditions, we observe that the uncharged particles accumulated at the contact line at faster rate than the charged ones (see Figure 7.1). This behavior was found regardless of the particle size (see Figures 7.1a and 7.1b), the type of particle (see Figures 7.1b and 7.1c), and the particle concentration (see Figures 7.1b and 7.1d). From the linear behavior of each particle increment, we compared the slopes obtained. The nearly uncharged MF-s particles arrived to the contact line 47.3 times faster than the charged ones, and the ratio between amount of

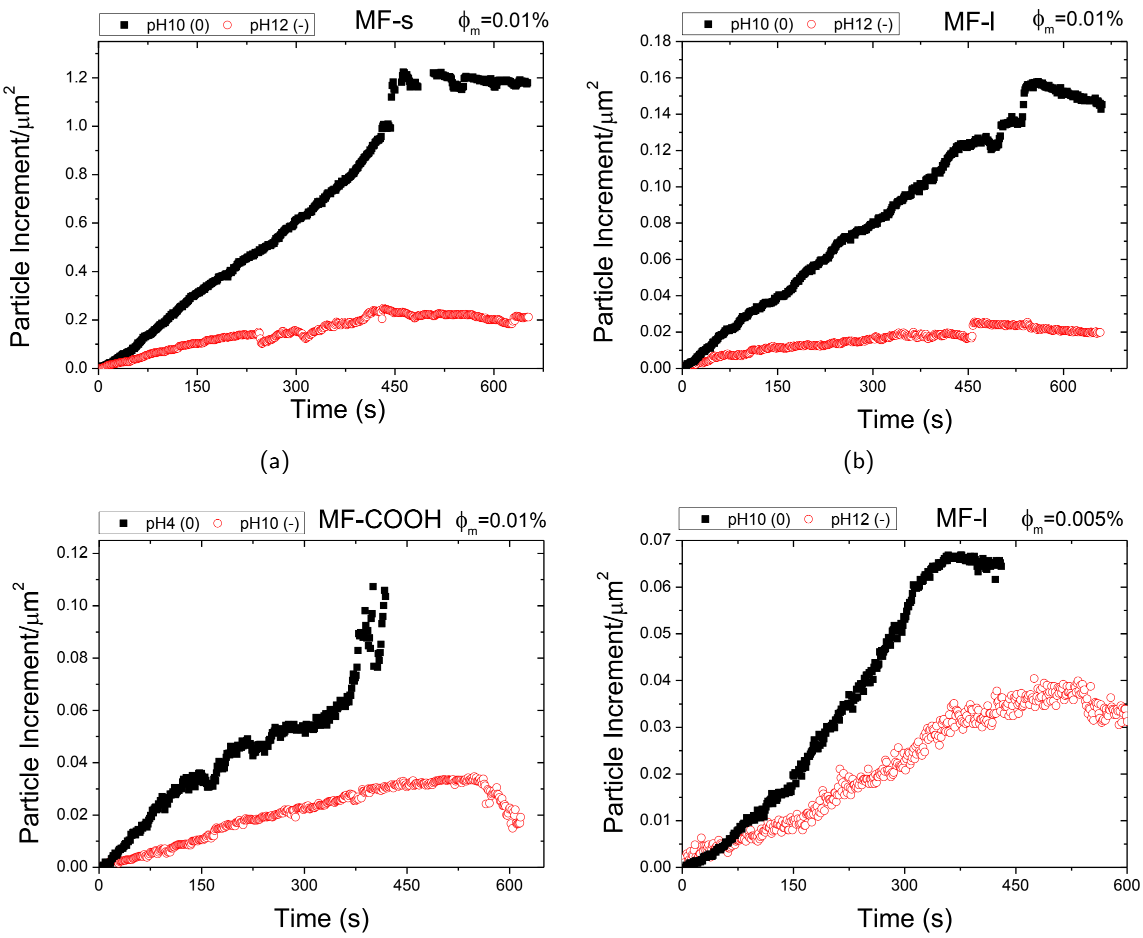

(a) (b)

(c) (d)

Figure 7.1: Number increment of particles per unit of drop area with different size, nature and concentration deposited on glass substrates for two electric states. The particles used were: (a) MF-s at 0.01% (w/w), (b) MF-l at 0.01% (w/w), (c) MF-COOH at 0.01% (w/w) and (d) MF-l at 0.005% (w/w).

material deposited was 5. At the same solid fraction (0.01% (w/w)), the barely charged MF-l particles accumulated 7.4 times faster than the charged MF-l particles due to the lower number of larger particles although the ratio between the masses of final deposit was 6. The uncharged MF-COOH particles, at the same concentration than the MF-l particles and with similar size, accumulated 2.2 times faster than the charged MF-COOH particles and the mass of the final deposit was 3 times greater. The difference between the charged MF-l and MF-COOH particles might be explained by the type of the interparticle interaction potential (surface electric potential, hydration layer, range), which can affect differently the osmotic compressibility of the dispersion and the hydrodynamic interactions. Finally, at lower particle concentration (0.005% (w/w)), the deposition of the barely charged MF-l particles was mitigated although it was 2.5 times faster than for the charged MF-l particles and the mass deposited was 1.7 times greater. The rate of deposition of charged particles revealed the particular balance between the outward convective flow and the inward diffusive flow. The interacting particles are transported towards the contact line at the same time while they intend to diffuse away from it, rather than the uncharged particles, due to their greater diffusion coefficient near the contact line. Decreasing the bulk concentration (number of particles), the relative difference between uncharged and charged particles is also reduced because the evaporation-driven convective flow produces lower concentration gradients. Although our measurements were restricted just to the horizontal surface of the substrate, the development of vertical concentration

The accumulation of barely charged particles was also favored on PMMA substrates, rather than with the charged ones, under the same evaporation conditions (see Figure 7.2). However, the particle deposition was less favored than on the glass substrates by the low convective flow developed on the PMMA substrates due to their higher receding contact angle. This reduced significantly the differences between nearly uncharged and charged particles except for the "rush-hour" stage, where the convective flow became significant as well as the local particle concentration. At 0.01% (w/w), the uncharged MF-COOH particles initially arrived at the contact line on the PMMA substrate only 1.5 times faster forming a deposit 2 times greater (see Figure 7.2a) whereas the uncharged MF-s particles accumulated 1.3 times faster than the charged ones and the final deposit was 1.9 times greater (see Figure 7.2b). With charged MF-l particles at 0.01% (w/w), the contact line mostly receded on the PMMA substrates with micron-sized particles although the faster accumulation of uncharged particles could delay, or even occasionally frustrate, this receding motion by enhancing the self-pinning. However, by using nanometer-sized particles at the same solid fraction, the triple line remained pinned during the complete evaporation of the drop, regardless of the particle charge. In Figure 7.2b, we also observe a unexpected behaviour of the nearly uncharged MF-s particles. They were transported faster than the charged ones at the beginning of the drop evaporation, but their deposition was suddenly retarded and as consequence there was a greater increment of charged MF-s particles at the triple line. At the time that the drop containing charged MF-s particles collapsed and dried, the nearly uncharged MF-s particles

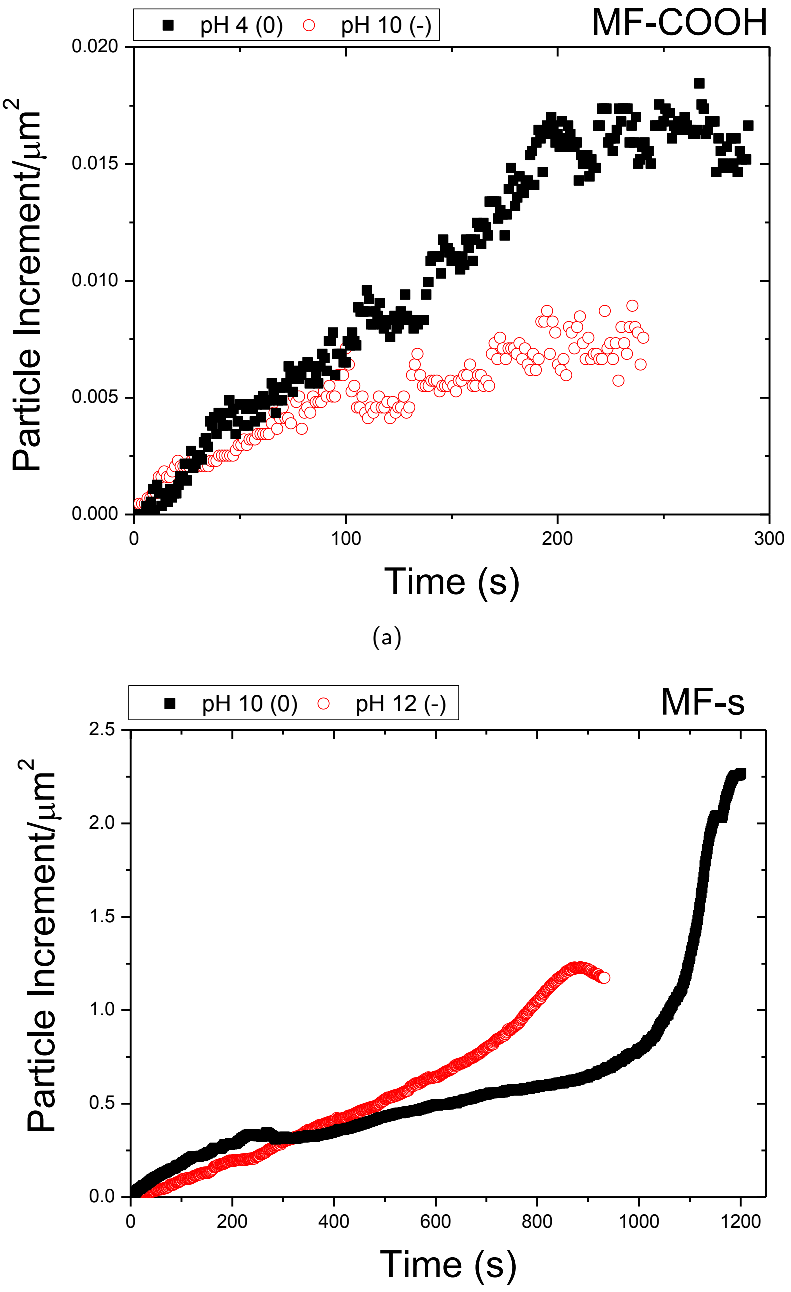
(a)

(b)

Figure 7.2: Particle increment per unit of drop area obtained on PMMA substrates for different charge states of (a) the MF-COOH particles and (b) the MF-s particles at 0.01% (w/w).

began to describe a marked "rush-hour" motion up to exceed significantly the number of charged MF-s particles accumulated at the contact line at the end of drop evaporation, as shown in Figure 7.1a on the glass substrate. When we used smaller particles (MF-s) on the PMMA substrate, a much greater number of particles arrived to the contact line despite of the low convective flow. This scenario should enhance the collective diffusion of charged nanoparticles, as happens at short times, but the own arrangement of the uncharged MF-s particles at the contact line could affect the local evaporation rate of the drop and as consequence, the "coffee-ring" effect. Due to the high receding contact angle of the PMMA substrate, the plausible piling up of particles inside the interfacial "wedge" of the drop and the resulting adsorption at the water-air interface (skin formation) might explain both the slower drop evaporation and the late avalanche-like outward motion of the barely charged nanoparticles. On the glass substrate, this effect was not found because the small "wedge" enabled the formation of a particulate film (*39*) rather than the particle piling up and besides the strong evaporative flux was hardly decreased.

We further conducted experiments with 1:1 binary mixtures of the MF-I and MF-COOH particles at 0.01% (w/w) (0.005% (w/w) per particle) on glass substrates. Although the bulk concentration and size was the same for both particles, the collective diffusion coefficient was expected to be different (*51*). At pH4, the MF-COOH particles were nearly uncharged while the MF-I particles were positively charged and at pH10, the MF-I particles were nearly uncharged while the MF-COOH particles were negatively charged (see Figure 5.1). Figure 7.3 shows the number increment of particle for the two bi-disperse suspensions. The rate of accumulation of the nearly uncharged MF-I particles was 4.9 times greater than the negatively charged MF-COOH particles whereas the final amount of material deposited 3.9 times greater (see Figure 7.3a). In Figure 7.3b, the rate of accumulation during the initial evaporation was identical for both particles. However, during the "rush-hour" stage, the increment of the barely charged MF-COOH particles overcomes the positively charged MF-I particles. It is important to take into account that these MF-I particles moving close to the negatively charged substrate should be further pushed towards it. Unlike the negatively charged particles, the positively charged particles are transported by three different mechanisms: the outward convective flow, the electrostatic attraction and the inward diffusive flow. This way, the identical early behaviour of the MF-I and MF-COOH particles can be explained once the collective diffusion and substrate-particle attraction were mutually canceled. However, during the "rush-hour" stage, the gradient of particle concentration was high enough so that the particle diffusion overcame the electrostatic interaction and mitigated the arrival of charged MF-I particles. This result points out to that the effect of the electrostatic substrate-particle interaction, even when the substrate and the particle are mutually attracted, is weaker on the final deposition than the electrostatic particle-particle interaction.

In binary mixtures, it is important to take into account that certain competing effects were present. Hydrodynamic and direct interactions might affect the osmotic pressure in a different

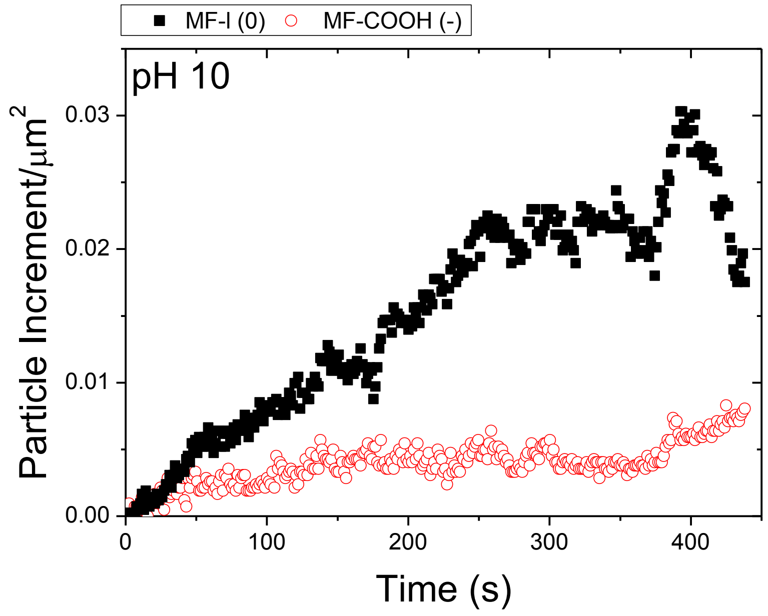

(a)

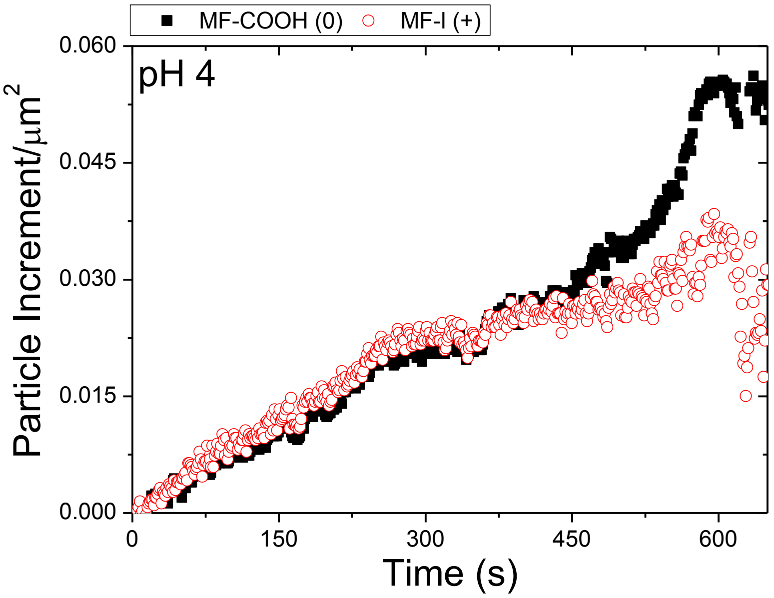

(b)

Figure 7.3: Particle increment per unit of drop area obtained with bi-disperse suspensions on glass substrates. The suspensions were prepared at 0.01% (w/w), 1:1 in number of particles and with different charge states: (a) nearly uncharged MF-I and negatively charged MF-COOH particles (pH 10), (b) nearly uncharged MF-COOH and positively charged MF-I particles (pH4).

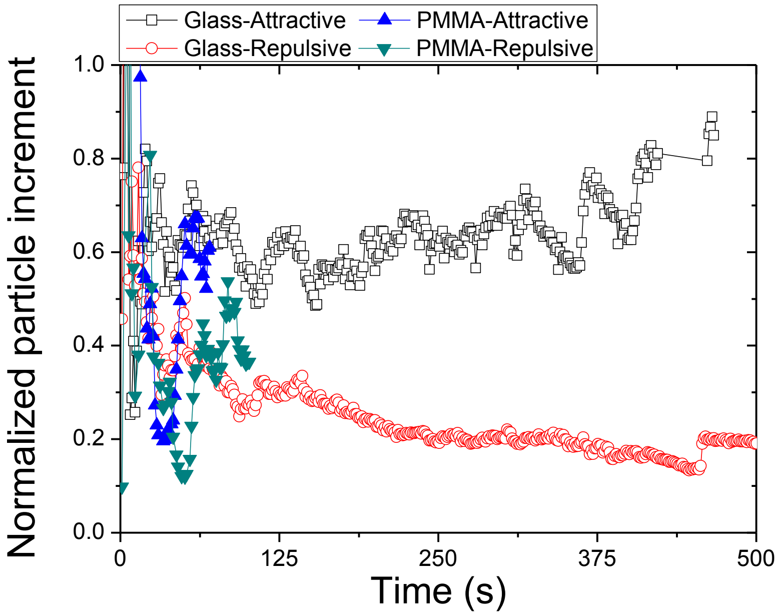

Figure 7.4: Normalized number increment of the charged MF-I particles at 0.01% (w/w) over the glass and PMMA substrates for different substrate-particle interaction. The increment per unit of wet area of the charged particles was divided by the increment per unit of wet area of the nearly uncharged particles, under the same evaporation conditions.

manner than in a monodisperse suspension prepared at the same concentration. For this purpose, we compared Figure 7.3a with experiments carried out under the same conditions but with the corresponding monodisperse suspensions (not shown). The relative rate of accumulation between nearly uncharged MF-I and negatively charged MF-COOH particles was greater in binary mixtures (4.9 times) than in separate monodisperse suspensions (2.8 times). Despite these effects, the role of the particle electric charge proved to be significant for the particles arriving at the triple line.

Finally, we explored the substrate-particle interaction. Three experiments were performed with the MF-I particles at 0.01% (w/w) on the glass and PMMA substrates: 1) negatively charged particles (substrate-particle repulsion), 2) positively charged particles (substrate-particle attraction) and 3) nearly uncharged particles (no significant interaction with the substrates). Results are summarized in Figure 7.4. We normalized the increment of charged particles arriving at the triple line per unit of wet area by the corresponding increment of uncharged particles, under the same evaporation conditions. From the values of contact angle hysteresis and receding contact angle, the drop evaporation on the PMMA substrate took longer than on the glass substrate. However, the experiment time was longer with the glass substrates because the triple line remained pinned until the complete evaporation. Whereas, for the PMMA substrates, the particle counting was interrupted when the contact line started to recede. Although, electrostatic attraction between particle and substrate enhances the deposition, it can be observed that all data are lower than the unit regardless of the type of substrate-particle interaction. This reveals that the positively and negatively charged particles are alike transported towards the contact line at a slower rate than the nearly uncharged particles, regardless of the substrate used. The balance between diffusive and convective flows seems to overcome the interaction between particle and substrate.

7.2 Conclusions

We found that collective diffusion mitigated the arrival of charged particles to the contact line, regardless of the type of particle and substrate used. The barely charged particles accumulated at the contact line from 40 up to 1.3 times faster than the charged particles, according to the case (concentration, particle size, type of substrate).The experiments carried out with binary colloidal mixtures plainly illustrate the influence of collective diffusion on the particle deposition. This opens up a new route in convective/capillary self-assembly for the particle segregation ruled by electric charge. These results may serve as a basis for the development of advanced theoretical models that describe the transport of the colloidal particles with the full convection-diffusion equation. In this scenario, substrate-particle electrostatic repulsion has no significant effect because, even for unlike charged substrate-particle systems (preferential deposition), the deposition was more favored with uncharged particles than with charged ones. However, the substrate does modulate the particle increment close to the contact line through the evaporation-driven capillary flow. The deposition of charged and nearly uncharged particles at short times is significantly different on substrates with small receding contact angles (high convective flows).

CHAPTER 8

Effect of the “colloidal Brazil” nut effect

In this chapter we focused on the behaviour of highly charged particles suspended in a “salt free” media. We investigated the importance of the charge-mass ratio of the particles on the convective-capillary self-assembly using the CLSM technique (see Section 5.3). The work the substrates used were Glass to fix the receding contact angle and to reduce the contact angle hysteresis. We modified the charge-mass ratio by selecting particles with different surface charge and density (see Section 5.2).

8.1 Results and discussion

In Figure 6.5, we plot the experiments performed on the Glass substrates with a 1:1 binary mixture of PS-I and MF-I particles at 0.01% (w/w) (3:1 in particle number) and the corresponding monodisperse suspensions at 0.005% (w/w). At pH12 both particles are negatively charged but the PS-I particles have higher unsigned charge (see Figure 5.1) This way, the charge-mass ratio for the PS-I particles is 6.7 times greater than for the MF-I particles. In the binary mixture (see Figure 6.5a), we observe that the PS-I particles arrived at the triple line 3.2 times faster than the MF-I particles and the final particle accumulation after the complete drop drying was 4.6 times greater. In the monodisperse cases (see Figure 6.5b), we observe that the deposition rate was 2.7

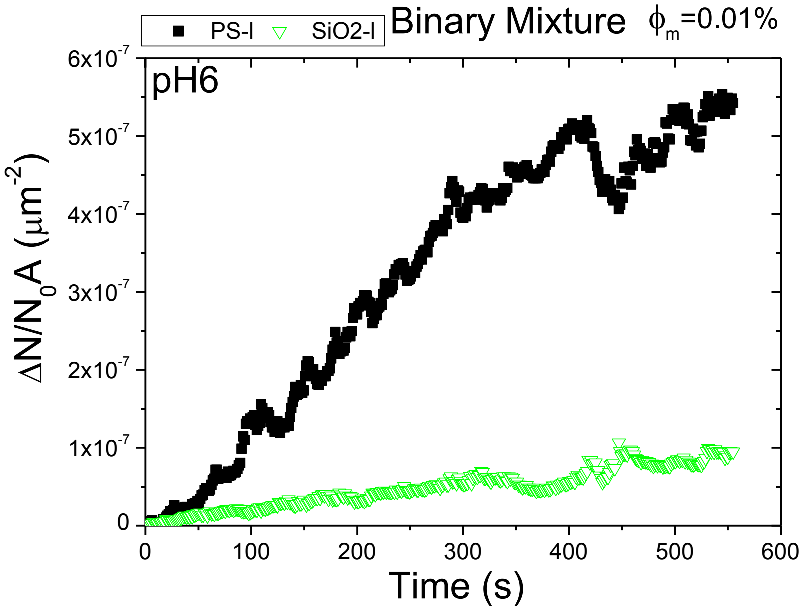

(a)

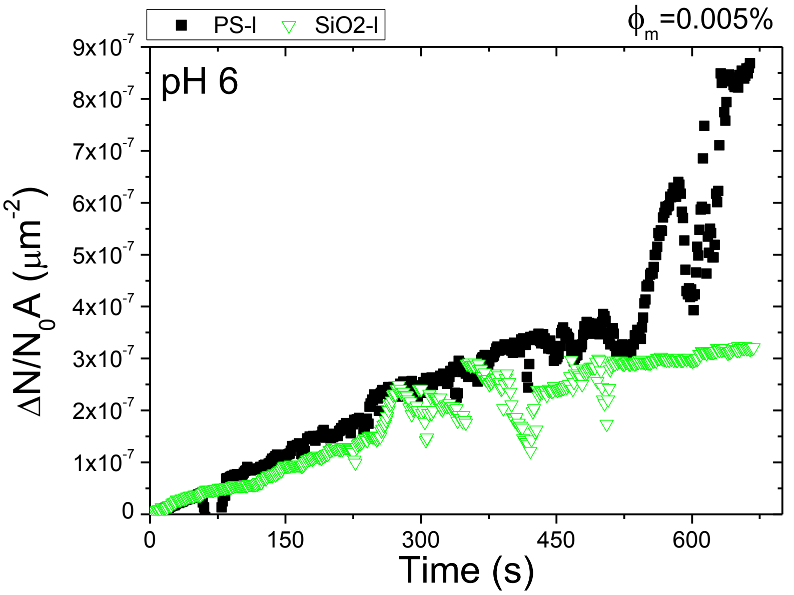

(b)

Figure 8.1: Normalized particle accumulation per area in terms of time for the PS-I and SiO2-I particles on Glass in: (a) a 1:1 binary mixture at pH6 and 0.01% (w/w) and (b) the corresponding monodisperse suspensions at pH6 and 0.005% (w/w).

times greater for the PS-l particles than for the MF-l ones, although the final deposit of particles was very similar. This behavior might be explained as follows. The PS-l particles are very charged over the entire pH scale. Strongly charged particles in "salt-free" media are known to suffer an "entropic lift" as the counter-ions move into the solvent seeking to maximize their entropy and homogeneity (*129*). This way, to maintain the macroscopic electro-neutrality the diffusing counter-ions pull the colloid avoiding its sedimentation. This effect causes segregation in binary mixtures where the micron-sized particles with lower charge-mass ratio sediment while the other ones are pushed upward by the former ones (*52*). In our experimental scenario, the MF-l particles partially settled from the bulk of the drop whereas the PS-l particles mostly remained suspended in the bulk or even close to the drop apex. This segregation within the bulk of the drop dictates the behavior nearby the contact line. The particles more susceptible to sedimentation (MF-l) arrived at the contact line in a lower number. On the other hand, all stable particles suspended in bulk (PS-l) were available to be pushed towards the contact line by the evaporation-driven flow. This behavior was observed with the binary mixture rather than with the monodisperse suspensions. The final accumulation of particles was higher for the PS-l particles in the binary mixture than in the monodisperse suspension. However, the MF-l particles accumulated less in the binary mixture than in the monodisperse case. This clearly points out to a particle segregation in the mixture due to the "colloidal Brazil nut" effect. Deposition is enhanced for the PS-l particles as they are "lifted" by the downward motion of the MF-l particles, while the accumulation of the latter ones is unfavoured as they are "sunk" due to the reciprocal mechanism. In the monodisperse experiments each particle in suspension was exclusively affected by sedimentation, with different rate, although the PS-l particles also deposited faster at the contact line than the MF-l particles.

The same result was found for the system formed by the PS-l and SiO2-l particles at the same concentration (5:2 in particle number) (see Figure 8.1). In the bidisperse mixtures (see Figure 8.1a), the SiO2-l particles arrived at the contact line 8.1 times slower than the PS-l particles. In the monodisperse suspensions (see Figure 8.1b), the PS-l particles accumulated 1.5 times faster than the SiO2-l particles. In this case, the SiO2-l and PS-l particles were equally charged (see Figure S2), but silica is much denser than polystyrene, thus the charge-mass ratio was 1.8 times greater for the PS-l particles than for the SiO2-l particles. The segregation was more significant than with the mixture of PS-l and MF-l. This points out to that in addition to the "colloidal Brazil nut" effect, other mechanisms should be further considered such as hydrodynamic interactions (*130*).

We further performed experiments with nanometer-sized particles to reduce the sedimentation (see Figure 8.2). We decreased the solid concentration of the mixture up to 0.002% (w/w) to allow a better counting without signal saturation (see Figure 8.2a). In this experiment, the "colloidal Brazil nut" effect was scarcely relevant because the MF-s particles accumulated nearby the triple line 1.3 times faster than the PS-s particles. Otherwise, in the monodisperse suspensions, the

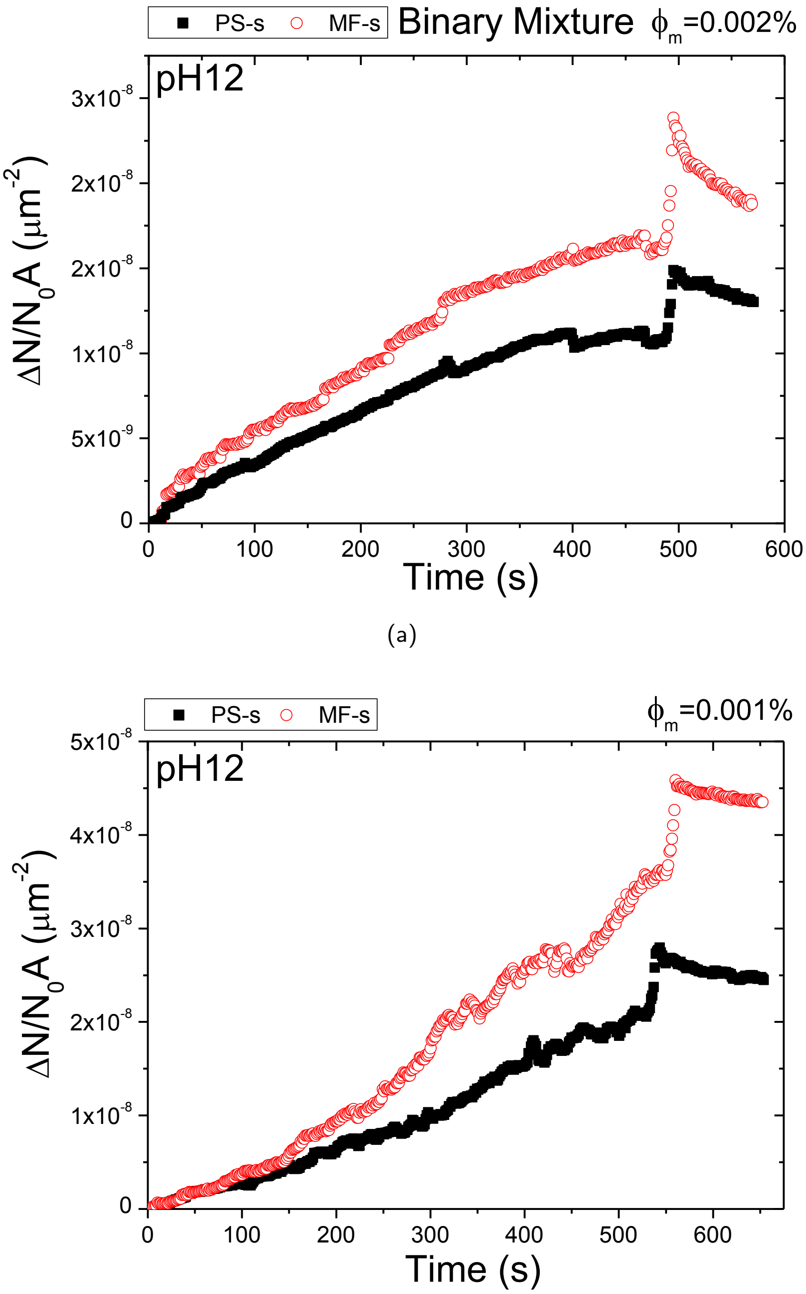

(a)

(b)

Figure 8.2: Comparison between the normalized particle increment per wet area in terms of time for the MF-s and PS-s particles in: (a) a 1:1 binary mixture at pH12 and 0.002% (w/w) and (b) the corresponding monodisperse suspensions at pH12 and 0.001% (w/w).

PS-s particles deposited at the triple line 1.4 times faster than the MF-s particles. This results is expected because all nanoparticles were suspended in the interior of the drop and then they were available to be pushed towards the contact line by the convective capillary flow. In the case of monodisperse suspensions, the final deposition was greater for both particles than in the binary mixture. This indicates no segregation of nanoparticles ruled by the "colloidal Brazil nut" effect.

8.2 Conclusions

Sedimentation of micron-sized particles affects the accumulation at their triple line. In "salt-free" media, polystyrene particles (charged) can be subjected to an "entropic lift" against sedimentation. Binary mixtures of particles with different charge-mass ratio revealed segregation as the "colloidal Brazil nut" effect. This effect was not observed with nanoparticles. In this scenario, we found that the charge-mass ratio of particles also modulates their deposition nearby the contact line.

Part III

Conclusions and Appendices

CHAPTER 9

Conclusions

In this thesis we have studied the assembly of colloidal particles by convective deposition. We have examined the effect of three factors: particle electric charge, wettability properties of the substrate, and charge-mass ratio of the particles by using two experimental approaches: driven evaporating menisci and free evaporating drops.

The set-up for driven evaporating menisci is very similar to the dip-coating technique frequently used in the coating industry. This set-up provides a controlled environment to develop protocols for reproducible coatings. The surface coverage is greater than with millimeter-sized drops although, of colloidal particles required is higher as well. We fixed the withdrawal velocity with this method, the particle concentration in bulk remains constant over the entire experiment. Hence, the effects due to the particle concentration gradient can be noticeable. We used smooth substrates with very different wettability properties. Three cleaning protocols were developed to alter the wettability properties of the substrates used. We measured the receding contact angle and contact angle hysteresis with the captive bubble technique. We also used nanoparticles of different surface charge and size. The morphology of the final deposits was analyzed by confocal microscopy and the contact line dynamics by optical microscopy. We modulated the evaporative flux through the relative humidity, the particle concentration and the substrate-particle system. Particle-particle and substrate-particle electrostatic interactions were varied through the medium pH.

Free evaporating drops in still air were used to explore the particle behaviour just at the vicinity of the contact line. We used Confocal Laser Scanning Microscopy to acquire real time images of the triple line of an evaporating colloidal sessile drop. We performed particle counting to estimate the in-plane accumulation per unit of drop area over the time. We used two transparent substrates with different wettability properties and six types of fluorescent particles selected as their fluorochrome, size, surface charge and density.

By using the two methodologies, the wettability properties of the substrate were found to be important for colloidal assembly. Driven evaporating menisci experiments showed different surface patterning as the substrate used. A transition from stripe-like deposit to heterogeneous film was reproduced as the substrate. Receding contact angle was directly related to the deposit dimensions and contact angle hysteresis was related to the gap between the bands. The stripe-to-stripe distance increases as the pinning time of the contact line (while the contact line remains static). We found that the pinning time correlated to the contact angle hysteresis because the meniscus could reach different meta-stable configurations. Very low values of the receding contact angle and nearly zero hysteresis enhanced the formation of an unresolved colloidal monolayer. We confirmed that the receding contact angle imposes a geometrical constraint for the particles at the triple line and due to this, size segregation of binary suspensions was observed with CLSM. Further, the particle deposition rate strongly depended on the value of the receding contact angle of the substrate. The effects of wettability properties of the substrate on the colloidal assembly are coupled because self-pinning affects contact line dynamics, and the particle accumulation depends at different extents on the space available near the contact line, the time of natural pinning and mostly, the convective flow. Further work should be addressed to optimize the production of colloidal patterns by changing the wettability properties of substrates.

We found that collective diffusion mitigated the arrival of electrically charged particles to the contact line, regardless of the type of particle, the substrate or the methodology used. The rate of accumulation for the barely charged particles was always lower than for the charged ones. From the experiments of driven receding contact lines, we conclude that the particle deposition may be controlled by the interplay between evaporative convection and collective diffusion. When the evaporation flow is weak, deposition can be suppressed if the long-range interparticle repulsion becomes important and the diffusion overcomes the particle transport by convection before reaching the triple line. this was observed in free evaporating drops with receding contact lines: high values of receding contact angle and low convective evaporative flows. Experiments carried out with binary colloidal mixtures illustrated the influence of collective diffusion on the particle deposition. With the same mixture, the pH variation always promoted the accumulation of the nearly uncharged particles. Likewise, barely charged particles enhanced the self-pinning of the contact line because their diffusion towards the bulk was reduced. Diffusive flow in drops takes relevance at low particle concentration, when the gradient between the contact line and bulk is important.

Instead, in driven evaporating menisci the bulk concentration remains constant and the effects due to concentration gradient are enhanced. In both scenarios, substrate-particle interactions seems to play no significant role because the deposition of particles was favored for the nearly uncharged particles rather than the charged ones, even for the opposite charged substrate-particle system. This opens up a new route in convective/capillary self-assembly for the particle segregation ruled by electric charge.

Finally, we found that the analysis of assembly of strongly charged particles (such as polystyrene) in a "salt free" media should be addressed carefully. For particles suspended in these conditions, ion condensation can produce an "entropic lift" against sedimentation. Binary mixtures of particles with different charge-mass ratio revealed segregation as the "colloidal Brazil nut" effect. This segregation produced an increase of the rate of accumulation of the particles suspended with higher charge-mass ratios. Otherwise, the particles with lower charge-mass ratio arrived at the contact line at lower rate. This effect was not observed with nanometer-sized particles as they did not develop sedimentation. This way, we found that the charge-mass ratio of particles further modulates the colloidal assembly by convective deposition nearby the contact line.

Conclusiones

En esta tesis hemos estudiado el ensamblaje de partículas coloidales mediante deposición convectiva. Hemos examinado el efecto de tres factores: la carga eléctrica de la partícula, las propiedades de mojado del sustrato y la relación carga-masa de las partículas a través de dos técnicas experimentales: meniscos líquidos guiados y gotas evaporándose libremente.

El dispositivo usado para los meniscos líquidos guiados es muy parecido al dispositivo de recubrimiento por inmersión que se usa en la industria de los revestimientos. Este dispositivo proporciona un entorno controlado para desarrollar protocolos para recubrimientos reproducibles. El área revestida es mayor con gotas milimétricas aunque, la cantidad de partículas coloidales necesaria es también mayor. Con este método hemos fijado la velocidad de succión y la concentración de partículas en el seno del reservorio permanece constante durante todo el experimento. Por lo tanto, los efectos de gradientes de concentración de partículas se hacen patentes. Hemos usado sustratos lisos con propiedades de mojado muy diferentes para lo que se han alterado debidamente los sustratos. Hemos medido el ángulo de contacto de retroceso y la histéresis en el ángulo de contacto con la técnica de burbuja cautiva. También hemos usado nanopartículas con carga superficial y tamaños diferentes. La morfología del depósito final se ha analizado con microscopía confocal y la dinámica de la línea de contacto con microscopía óptica. Hemos variado el flujo evaporativo por medio de la humedad relativa, la concentración de partículas y el propio sustrato. Las interacciones electrostáticas, tanto la sustrato-partícula como la partícula-partícula, han sido alteradas variando el pH del medio.

La técnica con gotas evaporándose libremente se ha utilizado para analizar el comportamiento de las partículas muy cerca de la línea de contacto. Hemos usado Microscopía de Barrido Láser Confocal (CLSM, de las siglas en inglés) para adquirir imágenes a tiempo real dentro de una gota sésil conteniendo coloides evaporándose. Hemos analizado las imágenes realizando un contaje temporal de las partículas acumuladas por área mojada para estimar el incremento de las mismas justo en el plano sobre sustrato. Se han usado dos sustratos transparentes con diferentes propiedades de mojado y seis partículas fluorescentes escogidas según su fluorocromo, tamaño carga superficial y densidad.

Con ambas configuraciones se obtuvo que las propiedades de mojado del sustrato son muy importantes para el auto-ensamblado coloidal. Los meniscos líquidos guiados produjeron diferentes patronados según el sustrato utilizado. Se formó un patronado a bandas evolucionando hacia una película homogénea según las propiedades de mojado de los sustratos utilizados. Las dimensiones de estas bandas estaban directamente relacionadas con el ángulo de contacto de retroceso y el espacio entre bandas ligado a la histéresis del ángulo de contacto. El salto entre bandas aumenta según aumenta el tiempo de anclado de la línea (mientras la línea permanece estática sin retroceder). Este lapso temporal está relacionado con la histéresis del ángulo de contacto porque el menisco puede adoptar más estados meta-estables cuanto mayor sea su histéresis. Sin embargo, valores muy bajos de la histéresis de ángulo de contacto, así como ángulos de retroceso muy bajos, favorecieron la formación de una monocapa coloidal incompleta. Hemos confirmado que el ángulo de contacto impone una restricción geométrica a la deposición de partículas en la línea de triple fase. Debido a esto observamos cómo las suspensiones binarias sufrieron una segregación por tamaño en las gotas analizadas con CLSM . Además, constatamos que el incremento de partículas en la línea de contacto depende mucho del ángulo de contacto de retroceso. Por todo esto, concluimos que las propiedades de mojado y el propio auto-ensamblado coloidal están acoplados ya que la acumulación de partículas provoca el anclaje de la línea y esto altera su dinámica, mientras que la deposición de partículas depende, entre otros factores, del espacio disponible, de los estados meta-estables que adopte la línea y sobre todo, del flujo convectivo. Planteamos como trabajo futuro el optimizar la producción de patrones coloidales alterando las propiedades de mojado.

También hemos observado que la difusión colectiva mitiga la llegada a la línea de contacto de partículas cargadas eléctricamente, independientemente del tipo de partícula, del sustrato o de la técnica usada. La acumulación de las partículas apenas cargadas siempre ha sido menor que la acumulación de partículas cargadas. De los experimentos con meniscos guiados concluimos que el balance entre el flujo convectivo originado por la evaporación y el flujo difusivo puede controlar la deposición de partículas. Cuando el flujo evaporativo es pequeño, se puede incluso suprimir la deposición si la repulsión entre partículas es suficientemente grande y la difusión supera así el transporte de partículas por convección. Este resultado se obtuvo también con gotas evaporándose libremente. Los experimentos con mezclas binarias han ilustrado la influencia de la difusión colectiva en la deposición de partículas. Para una misma pareja de partículas, a partir de la variación del pH las partículas casi descargadas siempre llegaron a un ritmo mayor que las partículas cargadas. De igual modo, las partículas casi descargadas favorecieron el anclaje de la línea de contacto ya que la difusión de las partículas hacia el seno de la gota era menor. El flujo difusivo en las gotas cobra relevancia cuando la concentración de partículas es baja, de este modo el gradiente entre la línea de contacto y el seno de la gota es mayor, aunque la concentración en el seno aumente con el tiempo. Sin embargo, para los meniscos guiados, la concentración en el seno del fluido permanece constante durante todo el experimento favoreciendo así la difusión colectiva. En ambas configuraciones, la interacción entre el sustrato y la partícula parece no ser determinante ya que la deposición de partículas cargadas era menor incluso para el caso en que sustrato y partícula tienen cargas opuestas (deposición favorecida). Estos resultados abren una vía para conseguir segregación de partículas por su carga para auto-ensamblado convectivo.

Por último, hemos observado que hay que tener especial cuidado en la deposición de partículas fuertemente cargadas (como el poliestireno) en un medio con baja fuerza iónica. Para una suspensión de partículas con estas características, la condensación de iones puede producir algo conocido como “empujón entrópico” que mitiga su sedimentación. Las mezclas binarias de partículas con diferente relación carga-masa segregaron según el conocido efecto “nueces de Brasil”. Esta segregación produce que las partículas permanezcan suspendidas con más facilidad, si las partículas tienen una relación carga-masa mayor. Por otro lado, las partículas con una menor relación carga-masa llegaban a la línea de contacto con un ritmo menor. Este efecto no ha sido observado para partículas más pequeñas (nanopartículas) porque debido a su tamaño, no sedimentan. De esta manera, hemos encontrado que la relación carga-masa de las partículas puede controlar el ensamblaje coloidal por deposición colectiva en la línea de contacto.

APPENDIX A

High Resolution SEM of nanoparticles

In this Appendix we visualize the nanoparticles used in Part I (see Section 2.3) with High Resolution Scanning Electron Microscopy (HRSEM). We used the AURIGA microscope (Carl Zeiss SMT) of the CIC-UGR. We obtained HRSEM images of the three particles used in Part I (SiO2-s, Glass and PMMA). These particles are monodisperse and spherical (see Figure A.1).

For the SiO2-s particles at pH9 on the Glass substrate described in Chapter 3 (charged state, see Figure 2.3) a spider-web pattern was eventually observed in their deposits rather than stripe-like pattern (see Figure A.2a). When we magnified the deposit, highly ordered self-assembly with hexagonal packaging was found (see Figure A.2b). We finally confirmed how the particles deposited on highly packed configuration even when isolated island were formed (see Figure A.3).

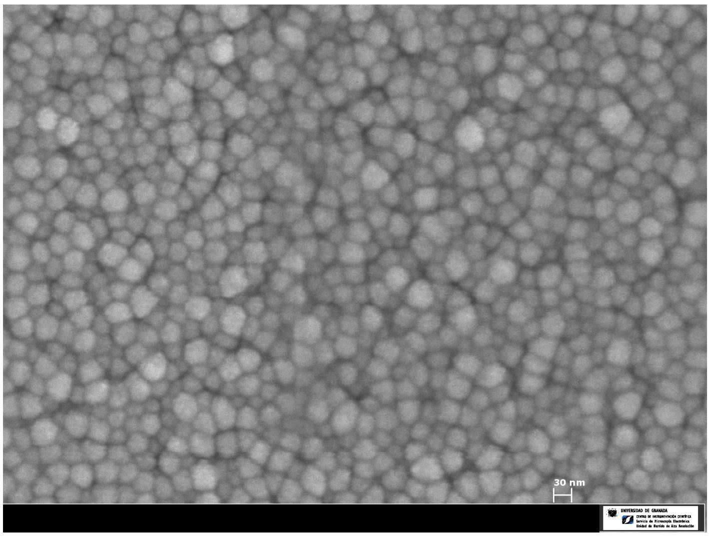

(a) Glass

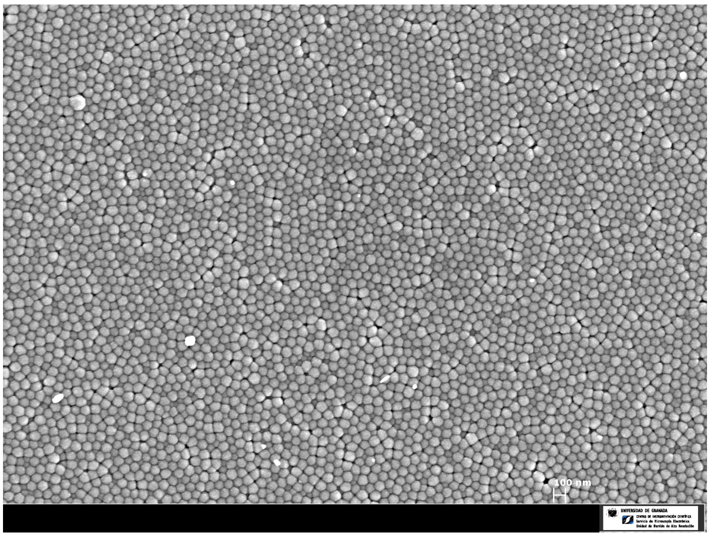

(b) SiO2-s

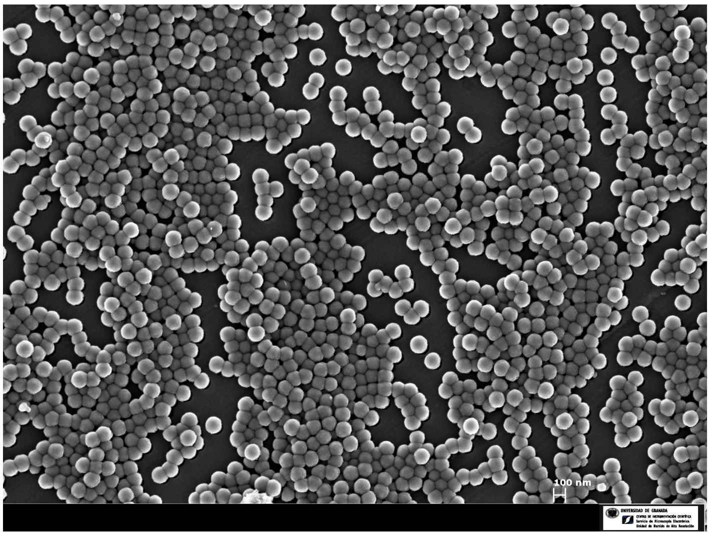

(c) PMMA

Figure A.1: HRSEM images of deposits of the particles used in Part I. Spherical shape and monodispersity are assured.

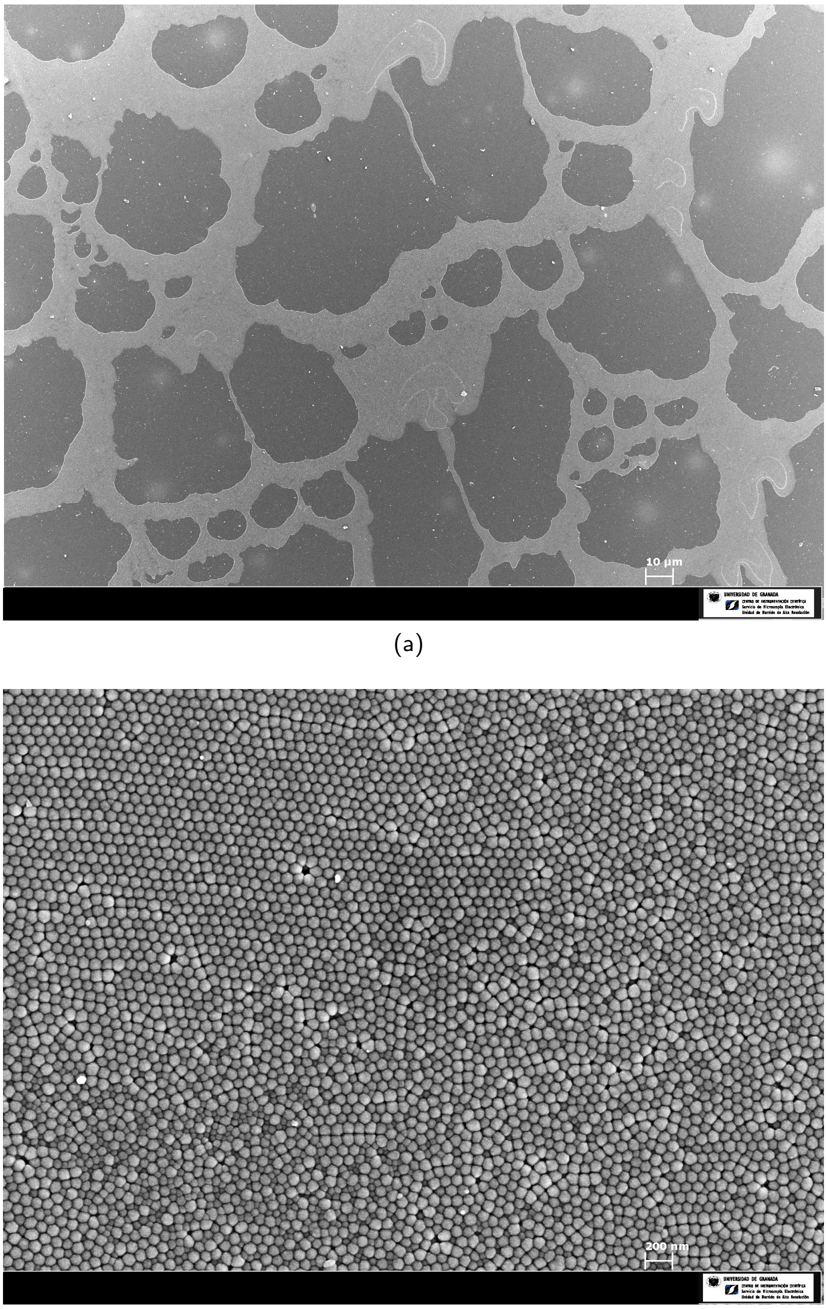

(a)

(b)

Figure A.2: HRSEM images of the deposits formed with the SiO2-s particles at pH9 (3% (w/w)) on the Glass substrate(a) A spider-web-like deposit is identified, (b) Magnification of (a), particles are locally highly-ordered.

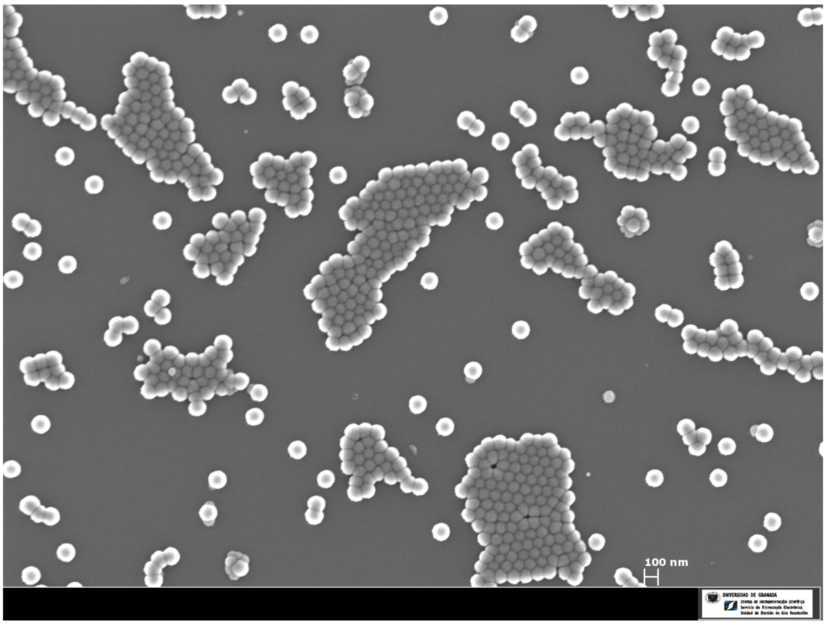

Figure A.3: HRSEM images of deposits of the SiO2-s particles at pH2 (3% (w/w)) on the PTGlas described in Chapter 3. Highly packed particles were observed to form isolated island leading to an unresolved monolayer.

APPENDIX B

Stick-Slip motion of evaporating contact lines

In convective capillary self-assembly, the use of a substrate with high Contact Angle Hysteresis (CAH) enhances the contact line self-pinning (see Section 1.2.1). This typically induce a "stick-slip" motion responsible for the periodical patterns discussed in Chapter 3. The meniscus configuration enhances the stick-slip behavior (*122*) because the contact line is driven to recede on the substrate.

In Chapter 3 we reported the displacement of the driven contact line with and it reveals a linear macroscopic behavior (see Figure 2.10). However, this behaviour was also found for experiments performed with nanoparticles suspensions at 3% (w/w). This is due to the camera resolution and the experimental conditions used. We increased the particle concentration to enhance the self-pinning as more particles deposit nearby the contact line per unit of time. This way, we performed driven-evaporating menisci experiments (see Section 2.3) at high concentration. We used the SiO2-s nanoparticles (see Section 2.2) as they were supplied at a particle concentration of 15% (w/w).

Firstly we studied the contact line dynamics on the three glass substrates described in Section 2.1. In this case, we used suspensions at pH2 to reduce possible diffusion effects (see Chapter 4).

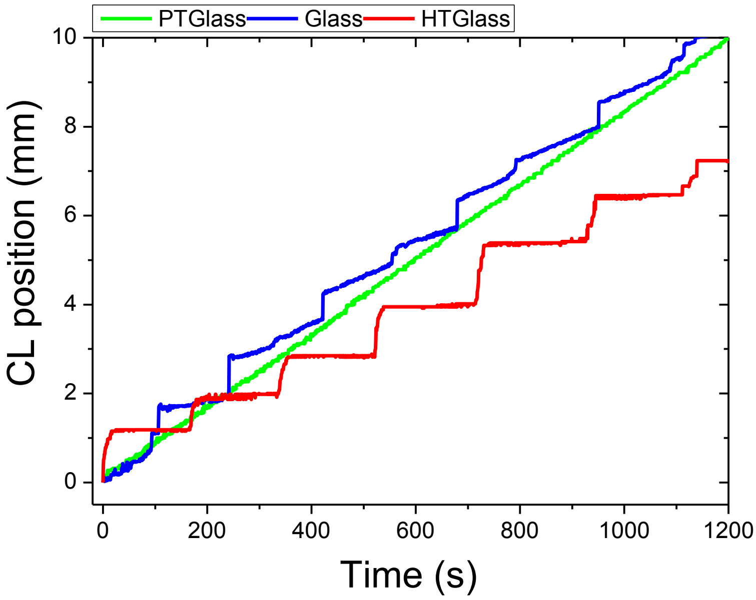

Figure B.1: Position of the contact line versus time for experiments of colloidal deposition with SiO2-s nanoparticles (pH12, 15% (w/w)) performed on the three glass substrates. Different stick-slip behavior is observed as the receding values of contact angle and CAH of each substrate.

Figure B.1 shows the position of the contact line against the time for each substrate. The plot origin was set to the position at time zero when the meniscus was at the highest position. As it begun to recede, the downward motion of the contact line was defined as a positive displacement. Different contact line dynamics was observed as the substrate used. For the PTGlass substrate we observe a linear behavior with no stick-slip. This is, the contact line receded at constant velocity as the resolution of our camera (see Figure B.1). The Glass substrate has almost the same value of receding contact angle then the PTGlass substrate, although higher CAH (see Table 2.1). This CAH enhanced the self-pinning of the contact line and produced a stick-lip motion observed by our experimental set-up. Finally on the HTGlass substrate, the triple line was further self-pinned and it exhibited a more pronounced stick-slip motion. These results sustain the discussion proposed in Section 3.1. We further conducted experiments on the Glass substrate using SiO2-s suspensions at two pH values (pH2 and pH9), namely with two charged states (see Figure 2.3). Different contact line dynamics was observed as the pH used (see Figure B.2). No stick-slip motion was observed with the charged SiO2-s particles (pH9) with the resolution of our camera. On the other hand, for the nearly uncharged particles (pH2), a well-defined stick-slip motion was obtained. This might be explained by the collective diffusion coefficient because it was higher for the charged particles (see Section 4.1) than the nearly uncharged ones. These particles were pushed towards the bulk and the self-pinning of the contact line was disfavoured. However, nearly uncharged particles faster accumulated at the triple line. The diffusive flow was not enough to allow the driven triple line to drag the particles deposited.

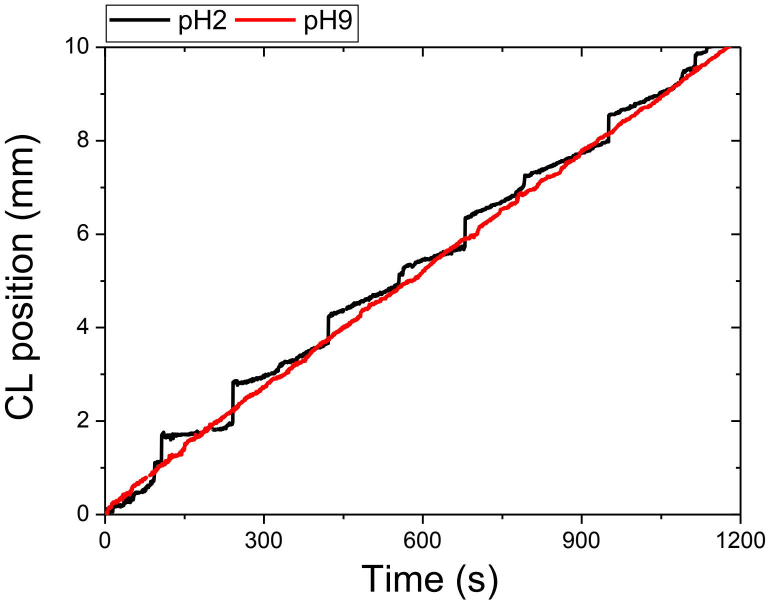

Figure B.2: Position of the contact line versus time for experiments of colloidal deposition with SiO2-s nanoparticles (15% (w/w)) performed on the Glass substrate for two pH values. Different stick-slip behavior is observed as the pH used.

With free evaporating drops, a similar behavior was observed. In this scenario, there is no driving force and self-pinning is mostly enhanced. On the three glass substrates (PTGlass, Glass and HTGlass), the contact line of water drops remains static during the entire evaporation process due to their low value of receding contact angle. However, on the PMMA substrate (see Section 2.1), the contact line does recede. We gently placed two drops containing the SiO2-s particles (0.01% (w/w)) at pH2 and pH9 accordingly, on a PMMA substrate (see Figure B.3a). The drop radius remained fixed at pH2 until the complete drop evaporation while it receded at pH9 (see Figure B.3b). This points out to an enhanced self-pinning for the barely charged particles. We also performed in-situ monitoring with the CLSM technique (see Section 5.3). We conducted the evaporation of 3μl drops containing the MF-I particles for two different charge states (pH10 and pH12, see Section 5.2). Since the nearly uncharged MF-I particles arrived to the triple line faster (see Chapter 7), their accumulation caused that the triple line remained self-pinned during the complete evaporation of the drop (not shown). The triple line could not be fixed by the charged particles because there were not sufficient number of particles deposited. Furthermore, due to their higher collective diffusion coefficient, they diffused away from the triple line more easily than the uncharged ones and they could be "dragged" by the line as it receded. No particle deposit was found except for the isolated "islands" produced by surface defects (see Figure B.4).

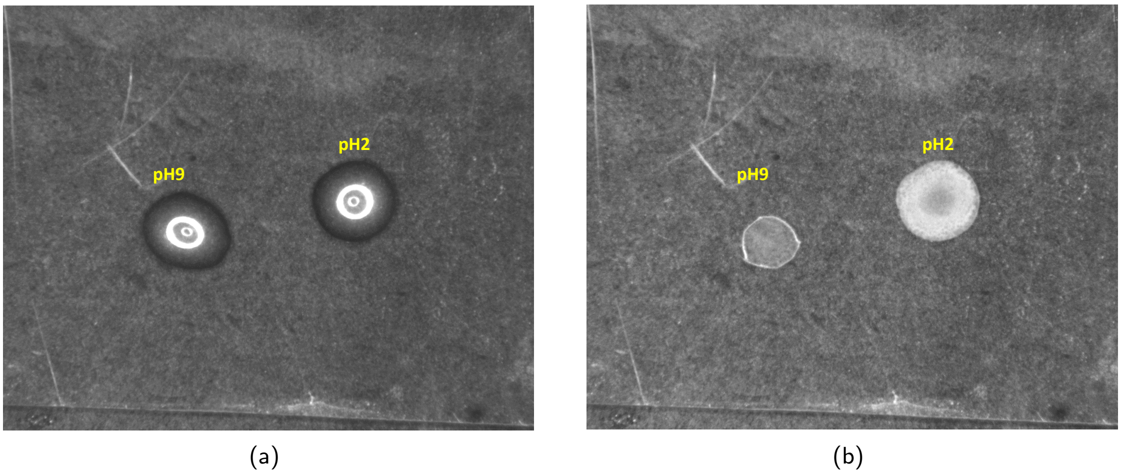

(a) (b)

Figure B.3: Cenital images of 3μl sessile drops containing the SiO2-s nanoparticles on PMMA at 0.01% (w/w) for two pH values (a) at the beginning of the experiment, (b) and after complete evaporation (b). The radius of the final deposit is smaller with the charged particles because the contact line receded.

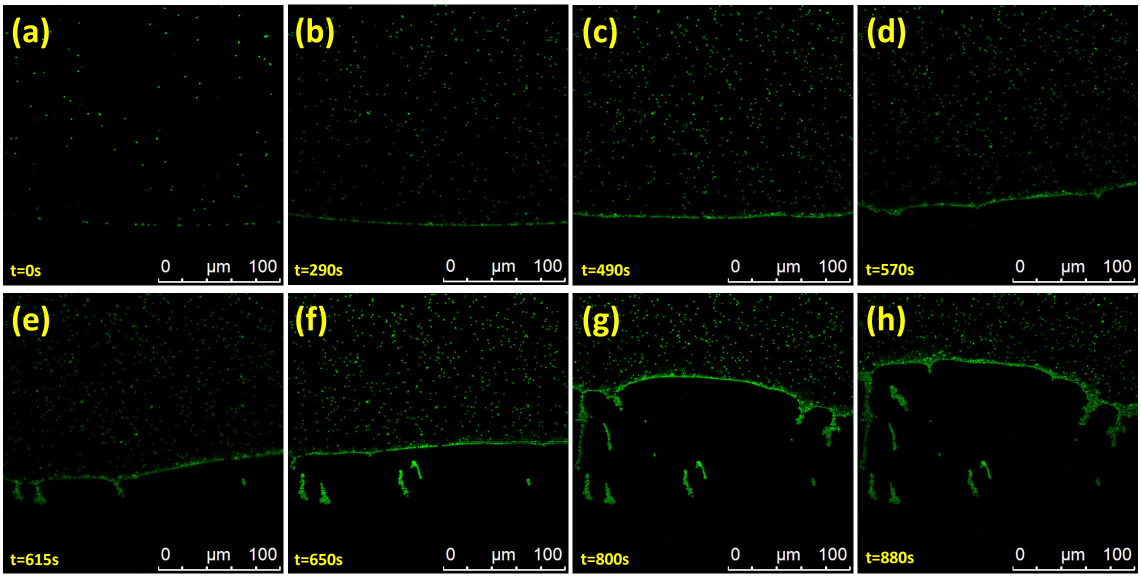

Figure B.4: Sequence of CLSM images of the contact line of a drop containing MF-I particles at pH12 and 0.01% (w/w). The charged MF-I particles slower accumulated at the triple line than the uncharged ones and this inhibited the contact line self-pinning.

APPENDIX C

Fingering and branching in particle deposits

In convective capillary self-assembly, the deposits can adopt multiple morphologies depending on the velocity of the contact line, the wettability properties of the substrate or the particle used (*75*). Branch-like structures have been observed with free evaporating drops (*74*, *131*) (see Figure C.1). These exotic structures are very interesting due to their singular geometry (*132*). Numerical models have been developed to reproduce these patterns (*133*). For the formation of these structures, it is important the particle shape (*87*). Marangonni flow and chemical-driven instabilities can also produce these deposits (*134*, *135*).

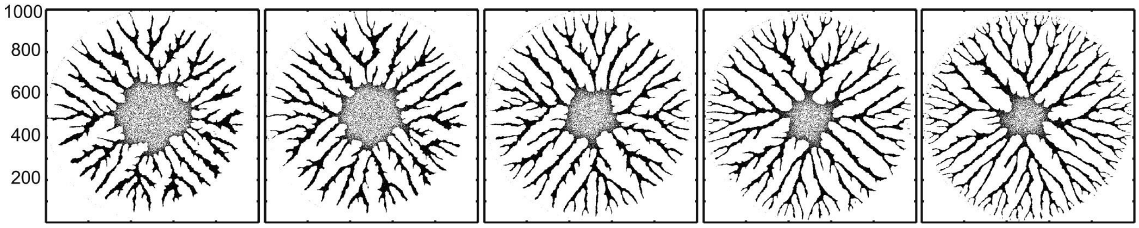

Figure C.1: Typical branch-like deposits found with evaporating colloidal drops. Simulations are able to reproduce the branched structures (*74*).

We performed driven-evaporating menisci experiments (see Section 2.3) with the glass and

PMMA particles at pH2 (see Section 2.2) and 3% (w/w) we analyzed the deposits with the white light confocal microscope (WLCM) (see Section 2.3). We selected the PTGlass substrate because of its very low receding contact angle and low contact angle hysteresis (see Table 2.1). With this system, we observed, in some cases, branched structures formed with the glass particles (see Figure C.2). We found that when the contact line is pinned at a small surface defect or inhomogeneity, a branch-like deposit is formed rather than a particulate film (see Figure C.3).

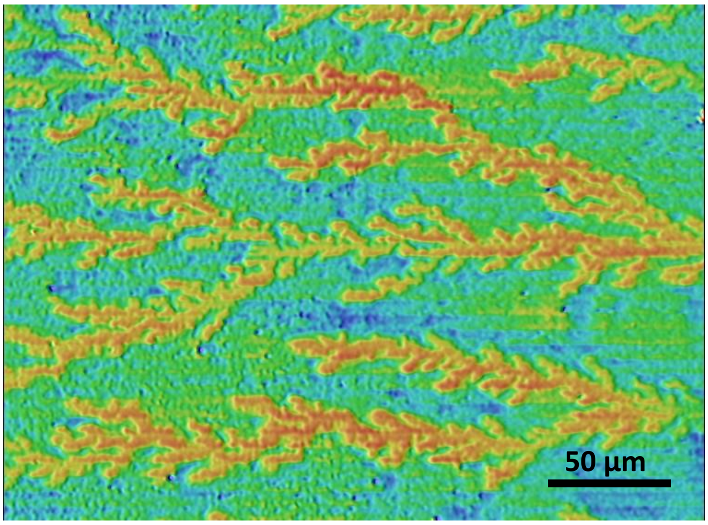

Figure C.2: WLCM topography of the deposit of glass particles formed on the PTGlass substrate at pH2 and 3% (w/w).

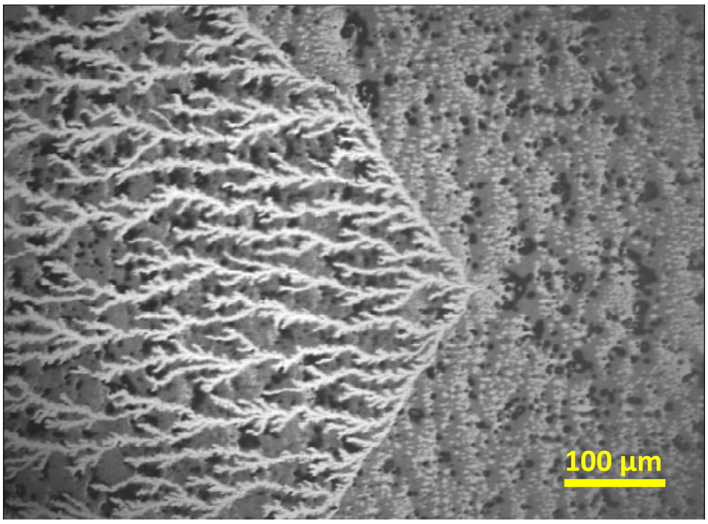

Figure C.3: Precursor event of contact line pinning for the formation of a branched structure of glass particles on the PTGlass substrate at pH2 and 3% (w/w).

Otherwise, when the PMMA particles were used, fingering was observed on the same substrate (see Figure C.4).

The mechanism for this effect in our systems are unknown because it is out of focus in this thesis. However, further work should be addressed in this respect to obtain reproducible branch-like deposits on the PTGlass substrate by driven-evaporating menisci.

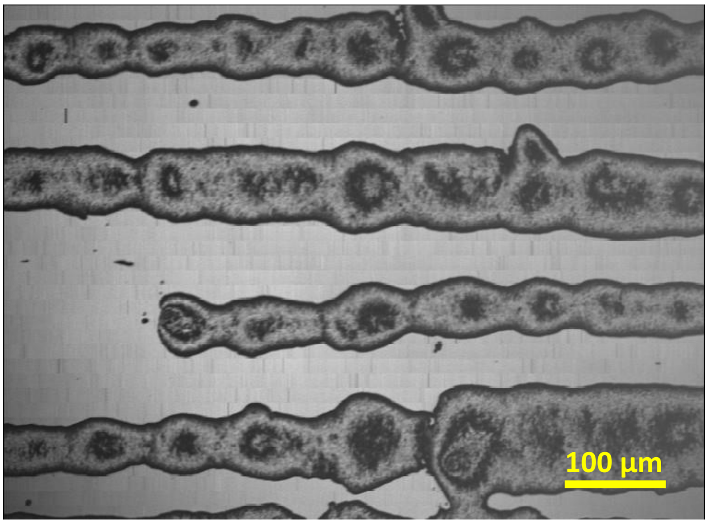

Figure C.4: Finger-like deposits formed with the PMMA particles on the PTGlass substrate at pH2 and 3% (w/w). We observe fingers along the direction of the contact line displacement.

APPENDIX D

Rush-hour effect in the colloidal deposition driven by evaporation

To illustrate the "rush-hour" effect (*76*) during the colloidal deposition in evaporation drops. We performed experiments described in Section 5.3 at the triple line, at ≈100μm from it and at ≈200μm. Far from the contact line the particle increment was much lower than at the triple line (see Figure D.1). In the three cases, we observe a sudden acceleration at the end of the drop evaporation and a final saturation due to the collapse of the drop apex. The experiment time increases as we approach to the drop center, as expected. A linear fitting was performed at the early stage of each graph. The particle increment per unit time at ≈100μm from the contact line was very similar to the particle increment per unit time at ≈200μm from the contact line (0.11 and 0.14 particles/second accordingly). On the other hand, the particle increment at the contact line was greater (2.95 p/s). We also performed a linear fit to the "rush-hour" stage of the experiments and the particle flow agrees in the three experiments (9.79, 4.64 and 9.52 p/s at the contact line, ≈100μm and ≈200μm accordingly).

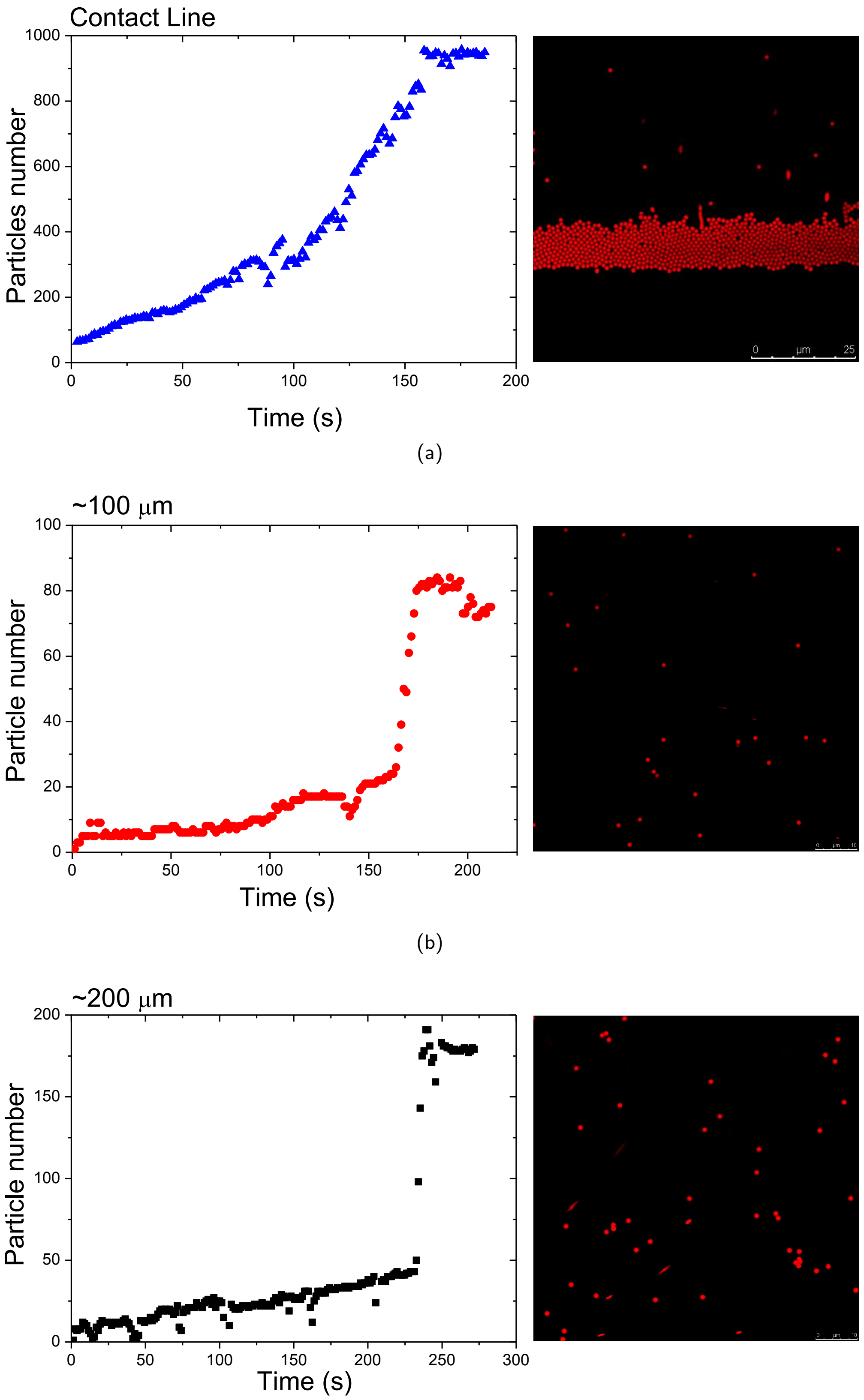

(a)

(b)

(c)

Figure D.1: In-plane motion of particles in evaporating drops for PS-I particles at pH7 and 0.01% (w/w) on glass substrate (a) at the contact line (b) at ≈100 μm from the contact line and (c) at ≈200 μm from the contact line.

APPENDIX E

Effect of the electrolyte concentration on the colloidal assembly of charged particles

Convective/capillary self-assembly of strongly charged particles at low ionic strength reveal a singular behavior. These colloidal suspensions are unexpectedly stable against sedimentation. Due to the so-called "entropic lift" related to the diffusion of counter-ions into the solvent (*129*). Counter-ions diffuse through a medium seeking to maximize their entropy and homogeneity. This way, to maintain the electroneutrality, they "push" the particles by repelling the counter-ions adsorbed into its surface (see Section 1.3.2). We studied the effect of added salt concentration within the low ionic strength regime. We measured the electrophoretic mobility of polystyrene particles (PS-I, see Section 5.2) at increasing concentrations of NaCl (see Figure E.1). We observed an increase of the surface charge of the PS-I particles as the NaCl concentration. We could not perform measurements at higher concentration (>4mM) due to device limitations. These results showed that the PS-I particles behaved atypically as the ionic strength was varied (*53*). We further performed in-plane particle counting using CLSM (see Section 5.3) with the PS-I suspensions on Glass (see Section 5.1), varying the concentration of in-excess electrolyte in the medium. We plotted the particle increment per unit of wet area against the time in Figure E.2. It can be observed that at increasing NaCl concentrations, the increment of particles nearby the triple line also increased. Figure E.3 shows the linear trend of the early flow of incoming particles (at

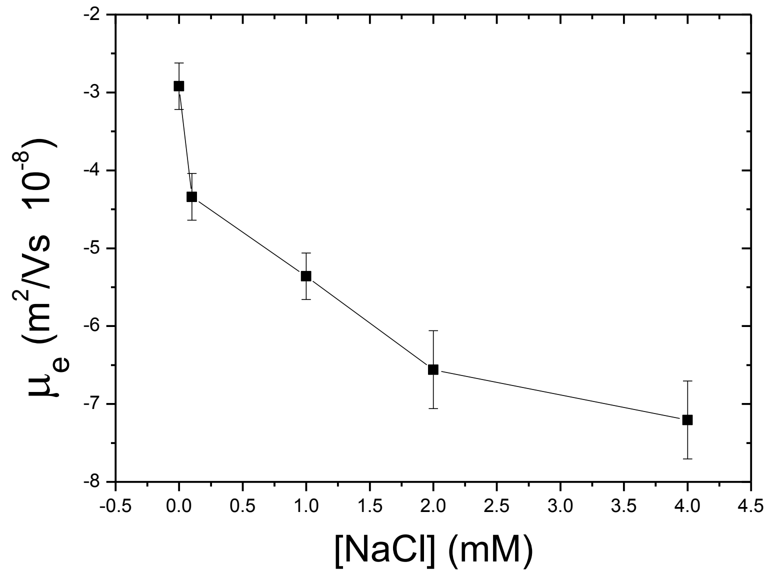

Figure E.1: Electrophoretic mobility for the PS-I particles (0.01% (w/w)) against the concentration of NaCl. an unexpected increase of the particle charge was observed as increasing electrolyte concentrations.

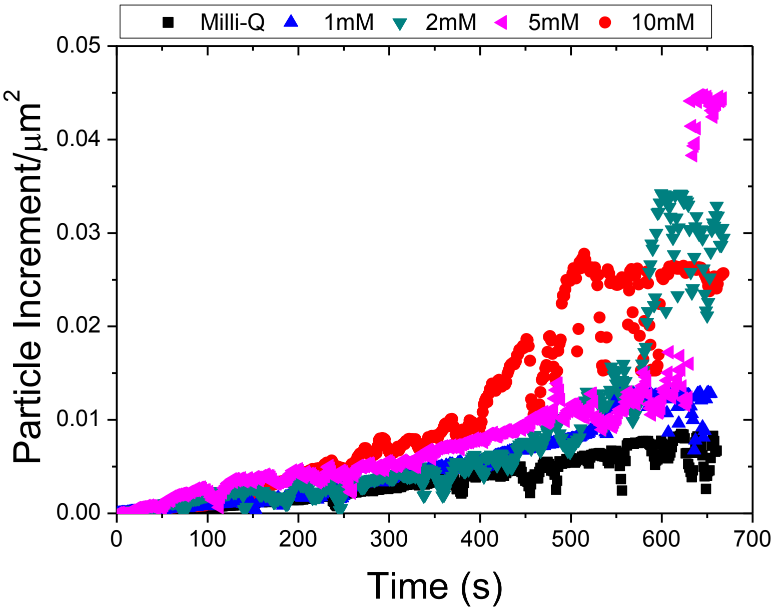

Figure E.2: Increment of PS-I particles nearby the triple line per unit of wet area against the time for the PS-I particles at 0.005% (w/w) at different NaCl concentrations.

short times) with the NaCl concentration of NaCl. As the concentration of electrolyte increases, the particles reach the contact line faster. We discarded effects due to substrate wettability because the substrate used was fixed.

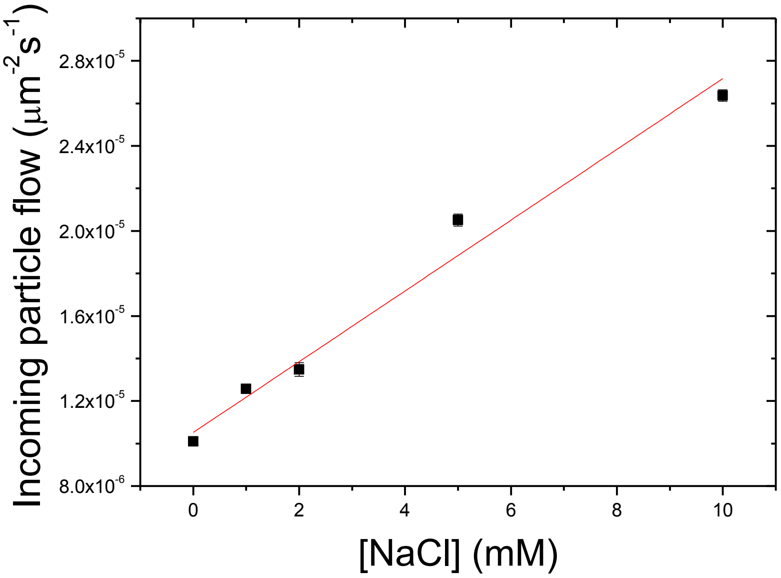

Figure E.3: Rate of PS-I particle increment at the triple line against the NaCl concentration.

From the real time CLSM images, we observe that the PS-I particles were gradually adsorbed at the water-air interface. This way, as we increased the salt concentration we observed well-ordered particles in the image background, while a few particles appear directly in the foreground, on the substrate (see Figure E.4). The water-air interface at the wedge-shaped region seems to be saturated as the electrolyte concentration. The ions from NaCl also suffer the "Coffee Stain" effect like the PS-I particles (*136*). This way, the concentration of electrolyte greater at the contact line than in the bulk. It is known that the surface tension of water increases as the concentration of NaCl (*137*). Therefore, a surface tension gradient was established along the water-air interface due to the NaCl concentration gradient. This surface tension gradient further developed a marangoni flow that intended to balance the gradient by replenishing water from the apex of the drop towards the contact line. Unlike the experiments where surfactants are used (*22*), in this scenario, the marangoni flow pushed the PS-I particles adsorbed towards the contact line. This way, as we increased the NaCl concentration, the marangoni flow was reinforced, and more particles arrived at the contact line from the water-air interface.

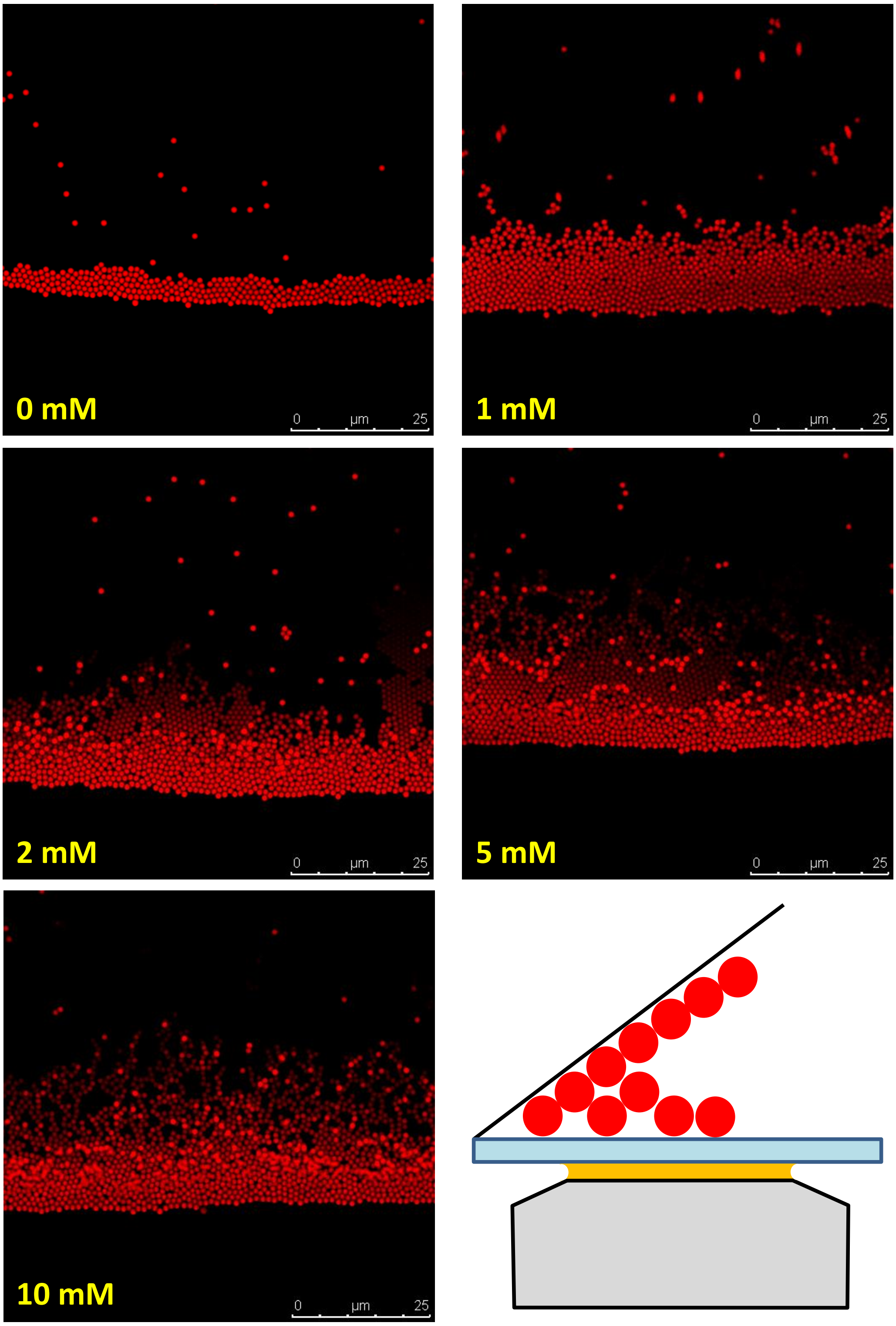

Figure E.4: CLSM images acquired at the final stage of evaporation. Images show the PS-I particle accumulation at the triple line for different NaCl concentrations. The air-liquid interface of the wedge-shaped region becomes visible from 2mM.

Bibliography

[1] Deegan, R. D.; Bakajin, O.; Dupont, T. F.; Huber, G.; Nagel, S. R.; Witten, T. A. Capillary flow as the cause of ring stains from dried liquid drops. *Nature* **1997**, *389*, 827–829.

[2] Tarasevich, Y.; Pravoslavnova, D. M. Segregation in desiccated sessile drops of biological fluids. *Eur. Phys. J. E* **2007**, *22*, 311–314.

[3] Li, Q.; Jonas, U.; Zhao, X. S.; Kappl, M. The forces at work in colloidal self-assembly : a review on fundamental interactions between colloidal particles. *Asia-Pac. J. Chem. Eng.* **2008**, *3*, 255–268.

[4] Lotito, V.; Zambelli, T. Self-assembly and nanosphere lithography for large-area plasmonic patterns on graphene. *J. Colloid Interface Sci.* **2015**, In press, http://dx.doi.org/10.1016/j.jcis.2014.11.007.

[5] Layani, M.; Berman, R.; Magdassi, S. Printing holes by a dewetting solution enables formation of a transparent conductive film. *Appl. Mater. Inerfac.* **2014**, *6*, 18668–18672.

[6] Sun, D.; Zhang, Y. Preparation of fast-drying waterborne nano-complex traffic-marking paint. *J. Coat. Technol. Res.* **2012**, *9*, 151–156.

[7] Trantum, J. R.; Wright, D. W.; Haselton, F. R. Biomarker-Mediated Disruption of Coffee-Ring Formation as a Low Resource Diagnostic Indicator. *Langmuir* **2012**, *28*, 2187–2193.

[8] Wen, J. T.; Ho, C. M.; Lillehoj, P. B. Coffee ring aptasensor for rapid protein detection. *Langmuir* **2013**, *29*, 8440–8446.

[9] Gulka, C. P.; Swartz, J. D.; Trantum, J. R.; Davis, K. M.; Peak, C. M.; Denton, A. J.; Haselton, F. R.; Wright, D. W. Coffee rings as low-resource diagnostics: detection of the malaria biomarker Plasmodium falciparum histidine-rich protein-II using a surface-coupled ring of Ni(II)NTA gold-plated polystyrene particles. *App. Mater. Int.* **2014**, *6*, 6257–6263.

[10] Ma, H.; Hao, J. Ordered patterns and structures via interfacial self-assembly: superlattices, honeycomb structures and coffee rings. *Chem. Soc. Rev.* **2011**, *40*, 5457–5471.

[11] Doganci, M. D.; Cavusoglu, S.; Oksuz, M.; Erbil, H. Y. Effect of surface free energy to control the deposit morphology during evaporation of graphite/SDS dispersion drops. *Coll. Surf. A* **2014**, *461*, 310–322.

[12] Erbil, H. Y. Control of stain geometry by drop evaporation of surfactant containing dispersions. *Adv. Colloid Interface Sci.* **2015**, In press, corrected proof, http://dx.doi:10.1016/j.cis.2014.08.004.

[13] Sobac, B.; Brutin, D. Desiccation of a sessile drop of blood: Cracks, folds formation and delamination. *Coll. Surf. A* **2014**, *448*, 34–44.

[14] Lee, I. Molecular self-assembly: smart design of surface and interface via secondary molecular interactions. *Langmuir* **2013**, *29*, 2476–2489.

[15] Abbasian, A.; Ghaffarian, S.; Mohammadi, N.; Khosroshahi, M.; Fathollahi, M. Study on different planforms of paint's solvents and the effect of surfactants (on them). *Prog. Org. Coat.* **2004**, *49*, 229 – 235.

[16] Shimoni, A.; Azoubel, S.; Magdassi, S. Inkjet printing of flexible high-performance carbon nanotube transparent conductive films by "coffee ring effect". *Nanoscale* **2014**, *6*, 11084–11089.

[17] Wray, A. W.; Papageorgiou, D. T.; Craster, R. V.; Sefiane, K.; Matar, O. K. Electrostatic Suppression of the "Coffee Stain Effect". *Langmuir* **2014**, *30*, 5849–5858.

[18] Tang, Y.; He, W.; Wang, S.; Tao, Z.; Cheng, L. The superiority of silver nanoellipsoids synthesized via a new approach in suppressing the coffee-ring effect during drying and film formation processes. *Nanotechnology* **2014**, *25*, 125602–7.

[19] Sun, P.; Ma, R.; Wang, K.; Zhong, M.; Wei, J.; Wu, D.; Sasaki, T.; Zhu, H. Suppression of the coffee-ring effect by self-assembling graphene oxide and monolayer titania. *Nanotechnology* **2013**, *24*, 075601–9.

[20] Hu, H.; Larson, R. G. Marangoni effect reverses coffee-ring depositions. *J. Phys. Chem. B* **2006**, *110*, 7090–7094.

[21] Buffone, C.; Minetti, C.; Boussemaere, L.; Roudgar, M.; De Coninck, J. Marangoni convection in evaporating meniscus with changing contact angle. *Exp. Fluids* **2014**, *55*, 1833–8.

[22] Still, T.; Yunker, P. J.; Yodh, A. G. Surfactant-Induced Marangoni Eddies Alter the Coffee-Rings of Evaporating Colloidal Drops. *Langmuir* **2012**, *28*, 4984–4988.

[23] Cecere, A.; Buffone, C.; Savino, R. Self-induced Marangoni flow in evaporating alcoholic solutions. *Int. J. Heat Mass Transfer* **2014**, *78*, 852 – 859.

[24] Larson, R. G. Transport and Deposition Patterns in Drying Sessile Droplets. *AIChE Journal* **2014**, *60*, 1538–1571.

[25] Erbil, H. Y. Evaporation of pure liquid sessile and spherical suspended drops: A review. *Adv. Colloid Interface Sci.* **2012**, *170*, 67–86.

[26] Bhardwaj, R.; Fang, X.; Attinger, D. Pattern formation during the evaporation of a colloidal nanoliter drop: a numerical and experimental study. *J. Phys.* **2009**, *11*, 075020–33.

[27] Askounis, A.; Sefiane, K.; Koutsos, V.; Shanahan, M. E. The effect of evaporation kinetics on nanoparticle structuring within contact line deposits of volatile drops. *Coll. Surf. A* **2014**, *441*, 855 – 866.

[28] Semenov, S.; Starov, V.; Rubio, R.; Agogo, H.; Velarde, M. Evaporation of sessile water droplets: Universal behaviour in presence of contact angle hysteresis. *Coll. Surf. A* **2011**, *391*, 135 – 144.

[29] Hu, H.; Larson, R. G. Analysis of the Microfluid Flow in an Evaporating Sessile Droplet. *Langmuir* **2005**, *21*, 3963–3971.

[30] Marín, A. G.; Gelderblom, H.; Lohse, D.; Snoeijer, J. H. Order-to-Disorder Transition in Ring-Shaped Colloidal Stains. *Phys. Rev. Lett.* **2011**, *107*, 085502–4.

[31] Wong, T.-S.; Chen, T.-H.; Shen, X.; Ho, C.-M. Nanochromatography Driven by the Coffee Ring Effect. *Anal. Chem.* **2011**, *83*, 1871–1873.

[32] Askounis, A.; Sefiane, K.; Koutsos, V.; Shanahan, M. E. Effect of particle geometry on triple line motion of nano-fluid drops and deposit nano-structuring. *Adv. Colloid Interface Sci.* **2014**, In press, DOI:10.1016/j.cis.2014.05.003.

[33] Han, W.; Byun, M.; Lin, Z. Assembling and positioning latex nanoparticles via controlled evaporative self-assembly. *J. Mater. Chem.* **2011**, *21*, 16968–16972.

[34] Sommer, A. P.; Ben-Moshe, M.; Magdassi, S. Size-Discriminative Self-Assembly of Nanospheres in Evaporating Drops. *J. Phys. Chem. B* **2004**, *108*, 8–10.

[35] Chen, H.; Tang, T.; Amirfazli, A. Fabrication of polymeric surfaces with similar contact angles but dissimilar contact angle hysteresis. *Coll. Surf. A* **2012**, *408*, 17–21.

[36] Zhang, L.; Nguyen, Y.; Chen, W. “Coffee ring” formation dynamics on molecularly smooth substrates with varying receding contact angles. *Coll. Surf. A* **2014**, *449*, 42 – 50.

[37] Deegan, R. D. Pattern formation in drying drops. *Phys. Rev. E* **2000**, *61*, 475–485.

[38] Eral, H. B.; Mannetje, D. J. C. M.; Oh, J. M. Contact angle hysteresis: a review of fundamentals and applications. *Coll. Pol. Sci.* **2012**, *291*, 247–260.

[39] Noguera-Marín, D.; Moraila-Martínez, C. L.; Cabrerizo-Vílchez, M. A.; Rodríguez-Valverde, M. A. Transition from Stripe-like Patterns to a Particulate Film Using Driven Evaporating Menisci. *Langmuir* **2014**, *30*, 7609–7614.

[40] Moraila-Martinez, C. L.; Cabrerizo-Vilchez, M. A.; Rodriguez-Valverde, M. A. Controlling the morphology of the ring-like deposits by varying the pinning time of driven receding contac lines. *Interf. Phen. Heat Trans.* **2013**, *1*, 195–205.

[41] Ghosh, M.; Fan, F.; Stebe, K. J. Spontaneous Pattern Formation by Dip Coating of Colloidal Suspensions on Homogeneous Surfaces. *Langmuir* **2007**, *23*, 2180–2183.

[42] Eral, H. B.; Augustine, D. M.; Duits, M.; Mugele, F. Suppressing the coffee stain effect: how to control colloidal self-assembly in evaporating drops using electrowetting. *Soft Matter* **2011**, *7*, 4954–4958.

[43] Li, Y.-F.; Sheng, Y.-J.; Tsao, H.-K. Evaporation Stains: Suppressing the Coffee-Ring Effect by Contact Angle Hysteresis. *Langmuir* **2013**, *29*, 7802–7811.

[44] Fan, F.; Stebe, K. J. Assembly of Colloidal Particles by Evaporation on Surfaces with Patterned Hydrophobicity. *Langmuir* **2004**, *20*, 3062–3067.

[45] Bao, R.-R.; Zhang, C.-Y.; Zhang, X.-J.; Ou, X.-M.; Lee, C.-S.; Jie, J.-S.; Zhang, X.-H. Self-Assembly and Hierarchical Patterning of Aligned Organic Nanowire Arrays by Solvent Evaporation on Substrates with Patterned Wettability. *App. Mater. Int.* **2013**, *5*, 5757–5762.

[46] Brutin, D.; Sobac, B.; Loquet, B.; Sampol, J. Pattern formation in drying drops of blood. *J. Fluid Mech.* **2011**, *667*, 85–95.

[47] Merlin, A.; Angly, J.; Daubersies, L.; Madeira, C.; Schöder, S.; Leng, J.; Salmon, J.-B. Time-resolved microfocused small-angle X-ray scattering investigation of the microfluidic concentration of charged nanoparticles. *Eur. Phys. J. E* **2011**, *34*, 1–7.

[48] Sempels, W.; De Dier, R.; Mizuno, H.; Hofkens, J.; Vermant, J. Auto-production of biosurfactants reverses the coffee ring effect in a bacterial system. *Nat. Commun.* **2013**, *4*, 1757–8.

[49] Paddock, S.; Eliceiri, K. In *Confocal Microscopy*; Paddock, S. W., Ed.; Methods in Molecular Biology; Springer New York, 2014; Vol. 1075; pp 9–47.

[50] Routh, A. F. Drying of thin colloidal films. *Rep. Prog. Phys.* **2013**, *76*, 046603–30.

[51] Nikiforow, I.; Adams, J.; König, A. M.; Langhoff, A.; Pohl, K.; Turshatov, A.; Johannsmann, D. Self-stratification during film formation from latex blends driven by differences in collective diffusivity. *Langmuir* **2010**, *26*, 13162–13167.

[52] Kruppa, T.; Neuhaus, T.; Messina, R.; Löwen, H. Soft repulsive mixtures under gravity: brazil-nut effect, depletion bubbles, boundary layering, nonequilibrium shaking. *J. Chem. Phys.* **2011**, *136*, 134106–10.

[53] Antonietti, M.; Vorwerg, L. Examination of the atypical electrophoretic mobility behavior of charged colloids in the low salt region using the O'Brian-White theory. *Coll. Pol. Sci.* **1997**, *275*, 883–887.

[54] Groot, R. D. Ion condensation on solid particles: Theory and simulations. *J. Chem. Phys.* **1991**, *95*, 9191–9203.

[55] Gillespie, D. A.; Hallett, J. E.; Elujoba, O.; Hamzah, A. F. C.; Richardson, R. M.; Bartlett, P. Counterion condensation on spheres in the salt-free limit. *Soft Matter* **2014**, *10*, 566–577.

[56] Wu, Y.; Zhang, X.; Zhang, X.; Munyalo, M. Modeling and experimental study of vapor phase-diffusion driven sessile drop evaporation. *Appl. Therm. Eng.* **2014**, *70*, 560–564.

[57] Noguera-Marín, D.; Moraila-Martínez, C. L.; Cabrerizo-Vílchez, M. A.; Rodríguez-Valverde, M. A. In-plane particle counting at contact lines of evaporating colloidal drops: effect of the particle electric charge. *Soft Matter* **2015**, *11*, 987–993.

[58] Fischer, B. J. Particle Convection in an Evaporating Colloidal Droplet. *Langmuir* **2002**, *18*, 60–67.

[59] Bocquet, L. Tasting edge effects. *Am. J. Phys.* **2007**, *75*, 148–150.

[60] Griffiths, D. J.; College, R. *Introduction to electrodynamics*; Prentice hall Upper Saddle River, NJ, 1999; Vol. 3.

[61] Soltman, D.; Subramanian, V. Inkjet-printed line morphologies and temperature control of the coffee ring effect. *Langmuir* **2008**, *24*, 2224–2231.

[62] Perelaer, J.; Smith, P. J.; van den Bosch, E.; van Grootel, S. S. C.; Ketelaars, P. H. J. M.; Schubert, U. S. The Spreading of Inkjet-Printed Droplets with Varying Polymer Molar Mass on a Dry Solid Substrate. *Macromol. Chem. Phys.* **2009**, *210*, 495–502.

[63] Girard, F.; Antoni, M.; Sefiane, K. On the Effect of Marangoni Flow on Evaporation Rates of Heated Water Drops. *Langmuir* **2008**, *24*, 9207–9210.

[64] Denneulin, A.; Bras, J.; Carcone, F.; Neuman, C.; Blayo, A. Impact of ink formulation on carbon nanotube network organization within inkjet printed conductive films. *Carbon* **2011**, *49*, 2603–2614.

[65] Shin, K.-Y.; Lee, S.-H.; Oh, J. H. Solvent and substrate effects on inkjet-printed dots and lines of silver nanoparticle colloids. *J. Micromech. Microeng.* **2011**, *21*, 045012–11.

[66] Wang, Z.; Zhao, Y.-P. In Situ Observation of Thermal Marangoni Convection on the Surface of a Sessile Droplet by Infrared Thermal Imaging. *J. Adhes. Sci. Technol.* **2012**, *26*, 1–12.

[67] Zhang, L.; Nguyen, Y.; Chen, W. "Coffee ring" formation dynamics on molecularly smooth substrates with varying receding contact angles. *Coll. Surf., A* **2014**, *449*, 42–50.

[68] Zhang, Z.; Zhang, X.; Xin, Z.; Deng, M.; Wen, Y.; Song, Y. Controlled inkjetting of a conductive pattern of silver nanoparticles based on the coffee-ring effect. *Adv. Mater.* **2013**, *25*, 6714–6718.

[69] Vogel, N.; Weiss, C. K.; Landfester, K. From soft to hard: the generation of functional and complex colloidal monolayers for nanolithography. *Soft Matter* **2012**, *8*, 4044–4061.

[70] Baughman, K. F.; Maier, R. M.; Norris, T. A.; Beam, B. M.; Mudalige, A.; Pemberton, J. E.; Curry, J. E. Evaporative Deposition Patterns of Bacteria from a Sessile Drop: Effect of Changes in Surface Wettability Due to Exposure to a Laboratory Atmosphere. *Langmuir* **2010**, *26*, 7293–7298.

[71] Bhardwaj, R.; Fang, X.; Somasundaran, P.; Attinger, D. Self-Assembly of Colloidal Particles from Evaporating Droplets: Role of DLVO Interactions and Proposition of a Phase Diagram. *Langmuir* **2010**, *26*, 7833–7842.

[72] Sommer, A. P. Limits of the Impact of Gravity on Self-Organizing Nanospheres. *J. Phys. Chem. B* **2004**, *108*, 8096–8098.

[73] Yakhno, T. A.; Yakhno, V. G.; Sanin, A. G.; Sanina, O. A.; Pelyushenko, A. S.; Egorova, N. A.; Terentiev, I. G.; Smetanina, S. V.; Korochkina, O. V.; Yashukova, E. V. The informative-capacity phenomenon of drying drops. *Eng. Med. Biol. Mag.* **2005**, *24*, 96–104.

[74] Crivoi, A.; Duan, F. Evaporation-Induced Branched Structures from Sessile Nanofluid Droplets. . *Phys. Chem. C* **2013**, *117*, 7835–7843.

[75] Yang, X.; Li, C. Y.; Sun, Y. From multi-ring to spider web and radial spoke: competition between the receding contact line and particle deposition in a drying colloidal drop. *Soft matter* **2014**, *10*, 4458–4463.

[76] Marin, A. G.; Gelderblom, H.; Lohse, D.; Snoeijer, J. H. Rush-hour in evaporating coffee drops. *Phys. Fluids* **2011**, *23*, 091111.

[77] Chen, L.; Evans, J. R. G. Arched structures created by colloidal droplets as they dry. *Langmuir* **2009**, *25*, 11299–11301.

[78] Morales, V. L.; Parlange, J.-Y.; Wu, M.; Pérez-Reche, F. J.; Zhang, W.; Sang, W.; Steenhuis, T. S. Surfactant-Mediated Control of Colloid Pattern Assembly and Attachment Strength in Evaporating Droplets. *Langmuir* **2013**, *29*, 1831–1840.

[79] Derjaguin, B.; Landau, L. Theory of the stability of strongly charged lyophobic sols and of the adhesion of strongly charged particles in solutions of electrolytes. *Prog. Surf. Sci* **1993**, *43*, 30 – 59.

[80] Verwey, E. J. W. Theory of the Stability of Lyophobic Colloids. *J. Phys. Coll. Chem.* **1947**, *51*, 631–636.

[81] Yan, Q.; Gao, L.; Sharma, V.; Chiang, Y.-M.; Wong, C. C. Particle and Substrate Charge Effects on Colloidal Self-Assembly in a Sessile Drop. *Langmuir* **2008**, *24*, 11518–11522.

[82] Hsueh, C.; Moraila-Martínez, C. L.; Doumenc, F.; Rodríguez-Valverde, M. A.; Guerrier, B. Self-assembly in drying complex fluid at low capillary number. *Chem. Eng. Process* **2013**, *68*, 64 – 68.

[83] Moraila-Martinez, C. L.; Cabrerizo-Vilchez, M. A.; Rodriguez-Valverde, M. A. The role of the electrostatic double layer interactions in the formation of nanoparticle ring-like deposits at driven receding contact lines. *Soft Matter* **2013**, *9*, 1664–1673.

[84] Crivoi, A.; Duan, F. Effect of Surfactant on the Drying Patterns of Graphite Nanofluid Droplets. *J. Phys. Chem. B* **2013**, *117*, 5932–5938.

[85] Majumder, M.; Rendall, C. S.; Eukel, J. A.; Wang, J. Y. L.; Behabtu, N.; Pint, C. L.; Liu, T.-Y.; Orbaek, A. W.; Mirri, F.; Nam, J.; Barron, A. R.; Hauge, R. H.; Schmidt, H. K.; Pasquali, M. Overcoming the "Coffee-Stain" Effect by Compositional Marangoni-Flow-Assisted Drop-Drying. *J. Phys. Chem. B* **2012**, *116*, 6536–6542.

[86] Yunker, P. J.; Still, T.; Lohr, M. a.; Yodh, a. G. Suppression of the coffee-ring effect by shape-dependent capillary interactions. *Nature* **2011**, *476*, 308–311.

[87] Yunker, P.; Lohr, M.; Still, T.; Borodin, A.; Durian, D.; Yodh, A. Effects of Particle Shape on Growth Dynamics at Edges of Evaporating Drops of Colloidal Suspensions. *Phys. Rev. Lett.* **2013**, *110*, 035501–5.

[88] Cassie, A. Contact angles. *Discuss. Faraday Soc.* **1948**, *3*, 11–16.

[89] Young, T. An Essay on the Cohesion of Fluids. *Phil. Trans. R. Soc.* **1805**, *95*, 65–87.

[90] Ángel Rodríguez-Valverde, M.; Tirado-Miranda, M. Derivation of Jurin's law revisited. *Eur. J. Phys.* **2011**, *32*, 49–54.

[91] Gao, L.; Mccarthy, T. J. Contact Angle Hysteresis Explained. *Langmuir* **2006**, *22*, 6234–6237.

[92] Korhonen, J. T.; Huhtamäki, T.; Ikkala, O.; Ras, R. H. A. Reliable measurement of the receding contact angle. *Langmuir* **2013**, *29*, 3858–3863.

[93] R.E. Johnson,; Dettre, R. H. Contact Angle Hysteresis III. Study of an Idealized Heterogeneous Surface. *J. Phys Chem.* **1964**, *68*, 1744–1750.

[94] Park, J. K.; Kang, K. H. Numerical analysis of moving contact line with contact angle hysteresis using feedback deceleration technique. *Phys. Fluids* **2012**, *24*, 042105–20.

[95] Weon, B.; Je, J. Self-Pinning by Colloids Confined at a Contact Line. *Phys. Rev. Lett.* **2013**, *110*, 028303.

[96] Shmuylovich, L.; Shen, A. Q.; Stone, H. A. Surface Morphology of Drying Latex Films : Multiple Ring Formation. *Langmuir* **2002**, *18*, 3441–3445.

[97] Picknett, R. G.; Bexon, R. The Evaporation of Sessile or Pendant Drops in Still Air. *J. Colloid Interface Sci.* **1977**, *61*, 336–350.

[98] Bourgès-Monnier, C.; Shanahan, M. E. Influence of Evaporation on Contact Angle. *Langmuir* **1995**, *11*, 2820–2829.

[99] Morozov, A. N.; Skripkinc, A. V. Description vaporation of a spherical liquid drop by a non-markovian random process based on integral stochastic equations. *Rus. Phys. J.* **2011**, *53*, 55–64.

[100] Deegan, R. D.; Bakajin, O.; Dupont, T. F.; Huber, G.; Nagel, S. R.; Witten, T. A. Contact line deposits in an evaporating drop. *Phys. Rev. E* **2000**, *62*, 756–765.

[101] Born, P.; Blum, S.; Munoz, A.; Kraus, T. Role of the meniscus shape in large-area convective particle assembly. *Langmuir* **2011**, *27*, 8621–8633.

[102] Leshansky, A. M.; Morris, J. F.; Brady, J. F. Collective diffusion in sheared colloidal suspensions. *J. Fluid Mech.* **2008**, *597*, 305–341.

[103] Einstein, A. A new analysis of molecule dimensions. *Ann. Phys.* **1906**, *19*, 289–306.

[104] Peppin, S. S. L.; Elliott, J. a. W.; Worster, M. G. Solidification of colloidal suspensions. *J. Fluid Mech.* **2006**, *554*, 147–166.

[105] Nägele, G. On the dynamics and structure of charge-stabilized suspensions. *Phys. Rep.* **1996**, *272*, 215 – 372.

[106] Peppin, S. S. L.; Elliott, J. A. W.; Worster, M. G. Solidification of colloidal suspensions. *J. Fluid Mech.* **2006**, *554*, 147–166.

[107] Daubersies, L.; Salmon, J.-B. Evaporation of solutions and colloidal dispersions in confined droplets. *Phys. Rev. E* **2011**, *84*, 031406.

[108] Widjaja, E.; Harris, M. T. Particle deposition study during sessile drop evaporation. *AIChE J.* **2008**, *54*, 2250–2260.

[109] Doumenc, F.; Guerrier, B. Drying of a Solution in a Meniscus: A Model Coupling the Liquid and the Gas Phases. *Langmuir* **2010**, *26*, 13959–13967.

[110] Frastia, L.; Archer, A. J.; Thiele, U. Dynamical Model for the Formation of Patterned Deposits at Receding Contact Lines. *Phys. Rev. Lett.* **2011**, *106*, 077801–4.

[111] Ras, M.; Philipse, A. P. Evidence for a macroscopic electric field in the sedimentation profiles of charged colloids. *Nature* **2004**, 2–5.

[112] Breu, A. P. J.; Ensner, H.-M.; Kruelle, C. A.; Rehberg, I. Reversing the Brazil-Nut Effect: Competition between Percolation and Condensation. *Phys. Rev. Lett.* **2003**, *90*, 014302–3.

[113] Williams, J. C. The Segregation of Particulate Materials. A Review. *Powder Technol.* **1976**, *15*, 245–251.

[114] Kudrolli, A. Size separation in vibrated granular matter. *Rep. Prog. Phys.* **2004**, *67*, 209–247.

[115] Möbius, M. E.; Lauderdale, B. E.; Nagel, S. R.; Jaeger, H. M. Size separation of granular particles. *Nature* **2001**, *414*, 270–1.

[116] Makse, H. A.; Halvin, S.; King, P. R.; Eugene, H. S. Spontaneous stratification in granular mixtures. *Nature* **1997**, *386*, 379–382.

[117] Esztermann, A.; Löwen, H. Colloidal Brazil-nut effect in sediments of binary charged suspensions. *Europhys. Lett.* **2004**, *68*, 120–126.

[118] Petasch, W.; Kegel, B.; Schmid, H.; Lendenmann, K.; Keller, H. Low-pressure plasma cleaning: a process for precision cleaning applications. *Surf. Coat. Technol.* **1997**, *97*, 176 – 181.

[119] Ruiz-Cabello, F. J. M.; Rodríguez-Valverde, M. A.; Cabrerizo-Vílchez, M. A. Contact Angle Hysteresis on Polymer Surfaces: An Experimental Study. *J. Adhes. Sci. Technol.* **2011**, *25*, 2039–2049.

[120] Moraila-Martínez, C. L.; Ruiz-Cabello, F. J. M.; Cabrerizo-Vílchez, M. A.; Rodríguez-Valverde, M. A. The effect of contact line dynamics and drop formation on measured values of receding contact angle at very low capillary numbers. *Coll. Surf., A* **2012**, *404*, 63 – 69.

[121] Berteloot, G.; Daerr, A.; Lequeux, F.; Limat, L. Dip coating with colloids and evaporation. *Chem. Eng. Process.* **2013**, *68*, 69–73.

[122] Bodiguel, H.; Doumenc, F.; Guerrier, B. Stick-Slip Patterning at Low Capillary Numbers for an Evaporating Colloidal Suspension. *Langmuir* **2010**, *26*, 10758–10763.

[123] Bou Zeid, W.; Brutin, D. Influence of relative humidity on spreading, pattern formation and adhesion of a drying drop of whole blood. *Coll. Surf. A* **2013**, *430*, 1–7.

[124] Petsev, D. N.; Denkov, N. D. Diffusion of charged colloidal particles at low volume fraction: Theoretical model and light scattering experiments. *J. Colloid Interface Sci.* **1992**, *149*, 329 – 344.

[125] Das, S.; Chakraborty, S.; Mitra, S. Ring stains in the presence of electrokinetic interactions. *Phys. Rev. E* **2012**, *85*, 046311–8.

[126] Genovese, D. B. Shear rheology of hard-sphere, dispersed, and aggregated suspensions, and filler-matrix composites. *Adv. Colloid Interface Sci.* **2012**, *171-172*, 1 – 16.

[127] Vizcarra-Rendón, A.; Medina-Noyola, M.; Klein, R. Electrolyte friction on non-spherical polyions. *Chem. Phys. Lett.* **1990**, *173*, 397 – 402.

[128] Diaz, C. a.; Xia, Y.; Rubino, M.; Auras, R.; Jayaraman, K.; Hotchkiss, J. Fluorescent labeling and tracking of nanoclay. *Nanoscale* **2013**, *5*, 164–168.

[129] Hynninen, A.-P.; Roij, R. V.; Dijkstra, M. Sedimentation profiles of charged colloids: Entropic lift and charge separation. *Europhys. Lett.* **2004**, *65*, 719–725.

[130] Moncho-Jordá, A.; Louis, A. A.; Padding, J. T. Effects of Interparticle Attractions on Colloidal Sedimentation. *Phys. Rev. Lett.* **2010**, *104*, 068301–4.

[131] Weon, B. M.; Je, J. H. Fingering inside the coffee ring. *Phys. Rev. E* **2013**, *87*, 013003–6.

[132] Crivoi, A.; Duan, F. Evaporation-induced formation of fractal-like structures from nanofluids. *Phys. Chem. Chem. Phys.* **2012**, *14*, 1449–1454.

[133] Crivoi, A.; Duan, F. Fingering structures inside the coffee-ring pattern. *Coll. Surf. A* **2013**, *432*, 119–126.

[134] Riolfo, L.; Carballido-Landeira, J.; Bounds, C.; Pojman, J.; Kalliadasis, S.; Wit, A. D. Experimental reaction-driven liquid film fingering instability. *Chem. Phys. Lett.* **2012**, *534*, 13 – 18.

[135] Yiantsios, S. G.; Higgins, B. G. Marangoni flows during drying of colloidal films. *Phys. Fluids* **2006**, *18*, 082103–11.

[136] Kaya, D.; Belyi, V. A.; Muthukumar, M. Pattern formation in drying droplets of polyelectrolyte and salt. *J. Chem. Phys.* **2010**, *133*, 114905–9.

[137] Jones, G.; Ray, W. A. The Surface Tension of Solutions of Electrolytes as a Function of the Concentration. III. Sodium Chloride. *J. Am. Chem. Soc.* **1941**, *63*, 3262–3263.